

RELATIONSHIPS BETWEEN HYDROCARBON-FILLED POROSITY AND  
KEROGEN MATURITY USING CORE DATA AND PETROPHYSICAL  
MODELING

A Thesis

by

MARGARET ZOE SMOOT

Submitted to the Office of Graduate and Professional Studies of  
Texas A&M University  
in partial fulfillment of the requirements for the degree of

MASTER OF SCIENCE

Chair of Committee,	Andreas Kronenberg
Co-Chair of Committee,	Michael Tice
Committee Member,	Zoya Heidari
Head of Department,	Rick Giardino

December 2015

Major Subject: Geophysics

Copyright 2015 Margaret Zoe Smoot

## ABSTRACT

Unconventional shale reservoir core samples analyzed by thermal and solvent extraction methods, analytical techniques, and microstructural observations exhibit strong positive linear relationships between hydrocarbon mobility and imaged pore space with maturity measured by vitrinite reflectance (%Ro). This positive relationship between thermal maturity and porosity differs from porosity-burial relationships governed by mechanical compaction and effective pressure.

Solvent extraction measurements and pyrolysis results indicate that solvent extraction removes both light (mobile) and heavy (immobile) components of bitumen, while thermal extraction fails to remove the immobile portion. Percent image area recognized as pore space in SEM BSE images show that the porosities are considerably lower than extraction predicted porosity measurements (% bulk volume). Thus, primary storage of pore-filling fluids is probably governed by adsorption and absorption.

Unconventional reservoir shale core samples subjected to Dean Stark and retort extractions combined with pyrolysis, performed both before and after extraction, permitted identification and quantification of measurable pore-filling fluids and organic matrix material. X-ray powder diffraction (XRD) provided bulk mineralogical composition information. Microscopic X-ray fluorescence (MicroXRF) revealed bedding patterns and areas of interest on which further imaging was performed. Attempts at identifying organic matter through electron microprobe wavelength-dispersive spectroscopy (WDS) proved unsuccessful due to difficulty imaging carbon

and low sulfur counts in the organics. Reflected light microscopy revealed foram shells and fractures acting as storage space for organic matter. Scanning electron microscopy (SEM) was performed on the micron scale in order to image porosity. Secondary electron (SE) images revealed very little about organic porosity, but backscattered electron (BSE) images successfully imaged pore space and provided a means for identifying organic matter based on its low density. Quantification of imaged pore space and organic matter was performed using ImageJ Software and manipulation of lookup table numbers (LUT #).

## DEDICATION

This thesis is dedicated to my mother. Thank you for your continual support throughout this process.

## ACKNOWLEDGEMENTS

I would like to thank my committee chair, Dr. Kronenberg, my co-committee chair, Dr. Tice, and my outside committee member, Dr. Heidari, for their guidance and invaluable advice throughout the course of this study.

I would also like to express my appreciation for those outside of my committee who helped me with lab work and provided expertise and support along my journey. Amber Peterson has served as a constant source of guidance and support throughout this process. Dr. John Pantano has also been a great source of information and encouragement throughout my research. Charles Choens has served as a great source of information. Without the help of Aaron Eaves, Grayson Dowlearn, and Harold Johnson, thin section preparation would have proven much more time consuming and challenging; I truly appreciate your invaluable assistance during this process. Dr. Ray Guillemette and Lindsey Hunt provided their expertise on the electron microprobe, and have been extremely generous with their time; I cannot thank them enough for their generosity. Lastly, I would like to express my gratitude to Dr. Michael Pendleton and Tom Stephens for their suggestions and expertise while using the SEM and trying out various techniques for imaging.

Without the financial support of Dr. Carlos Dengo and fellowships through the Chevron and the Berg-Hughes center, along with the ConocoPhillips SPIRIT scholarship, and additional funding from ExxonMobil, SPWLA, and Desk and Derrick

scholarships, this work would not have been possible. I truly appreciate all of the financial support.

Finally, I would like to thank my mother and Apostolos Kourakis for their never-ending support and encouragement throughout the years.

## NOMENCLATURE

Al	Aluminum
All	Ca-rich and Avg-Ca samples
AR	As-received
Avg-Ca	Samples representing mixed calcite/clay/quartz regions
Ba	Barium
BSE	Backscattered electrons
BV	Bulk volume
C	Carbon
Ca	Calcium
CaCO <sub>3</sub>	Calcium carbonate (calcite)
Ca-Rich	Samples representing highly calcitic regions
C <sub>C</sub>	Convertible carbon
C <sub>E</sub>	Expelled carbon
C <sub>HC</sub>	Retained hydrocarbons created from organic carbon
C <sub>R</sub>	Residual carbon
DS	Dean Stark
Fe	Iron
FID	Flame ionization detector
GRI	Gas research institute
HC	Hydrocarbon

H:C	Hydrogen:carbon
HI	Hydrogen index
LUT	Lookup table
LUT #	Lookup table number
MicroXRF	Microscopic X-ray fluorescence
OBM	Oil based mud
O:C	Oxygen:carbon
OI	Oxygen index
OM	Organic matter
P	Phosphorus
$P_e$	Effective pressure
$P_l$	Lithostatic pressure
$P_{pf}$	Pore fluid pressure
$P_w$	Hydrostatic pressure
PU	Porosity Units (% of bulk volume)
S	Sulfur
Si	Silicon
S1	Amount of free hydrocarbons (mg HC/g rock)
S2	Amount of hydrocarbons created by thermal cracking of nonvolatile organic matter (mg HC/g rock)
S3	Amount of generated CO <sub>2</sub> (mg CO <sub>2</sub> /g rock)
SE	Secondary electrons



SEM	Scanning electron microscopy
Ti	Titanium
T <sub>max</sub>	Peak temperature of S2
TOC	Total organic content
TOC <sub>ADJ</sub>	Adjusted total organic content
TOC <sub>O</sub>	Original total organic content
T1	Phase 1 of retort extraction (121°C)
T2	Phase 2 of retort extraction (315 °C)
T3	Phase 3 of retort extraction (704 °C)
USGS	United States Geological Survey
WDS	Wavelength-dispersive spectroscopy
XRD	X-ray powder diffraction
Φ <sub>hc</sub>	Hydrocarbon porosity
φ <sub>t</sub>	Total porosity
φ <sub>w</sub>	Water porosity
%Mob	Mobile percentage of hydrocarbon porosity

## TABLE OF CONTENTS

	Page
ABSTRACT .....	ii
DEDICATION .....	iv
ACKNOWLEDGEMENTS .....	v
NOMENCLATURE.....	vii
TABLE OF CONTENTS .....	x
LIST OF FIGURES.....	xii
LIST OF TABLES .....	xv
1. INTRODUCTION.....	1
1.1 Organic matter .....	2
1.2 Porosity .....	6
1.3 Kerogen type and maturity .....	8
2. BACKGROUND.....	12
2.1 Bulk extraction measurements .....	13
2.2 Microstructural observations and imaging.....	18
3. METHODS.....	22
3.1 Porosity estimates.....	22
3.1.1 Dean Stark: solvent extraction .....	22
3.1.2 Retort: thermal extraction.....	23
3.2 Pyrolysis and LECO total organic content methods .....	24
3.3 Compositional analysis of the rock matrix .....	27
3.3.1 X-ray powder diffraction.....	27
3.3.2 Microscopic X-ray fluorescence .....	28
3.3.3 Electron microprobe: wavelength-dispersive spectroscopy .....	29
3.4 Microscopic imaging.....	30
3.4.1 Reflected light microscopy.....	31

	Page
3.4.2 Scanning electron microscopy: secondary electron imaging .....	31
3.4.3 Scanning electron microscopy: backscattered electron imaging.....	32
3.5 Upscaling: petrophysical applications.....	33
4. RESULTS.....	35
4.1 Porosity observations .....	35
4.2 Organic matter composition and potential .....	39
4.3 Composition and imaging .....	40
4.3.1 X-ray powder diffraction.....	45
4.3.2 Microscopic X-ray fluorescence .....	47
4.3.3 Reflected light microscopy.....	51
4.3.4 Wavelength-dispersive spectroscopy .....	53
4.3.5 Scanning electron microscopy .....	55
5. DISCUSSION .....	62
5.1 Porosity analysis.....	62
5.2 Organic matrix and hydrocarbon mobility .....	78
5.2.1 Matrix-contributing organic matter.....	78
5.2.2 Mobility .....	82
5.3 Compositional analysis and imaging.....	86
5.3.1 General composition .....	86
5.3.2 Density-based quantification.....	87
5.3.3 Pore conservation: effective pressure.....	97
5.3.4 Backscattered electron porosity relationships .....	105
5.4 Upscaling.....	110
6. CONCLUSIONS .....	114
REFERENCES .....	116
APPENDIX A .....	123
APPENDIX B .....	124

## LIST OF FIGURES

	Page
Figure 1 Organic matter maturation and generated products .....	3
Figure 2 Total organic content evolution and expulsion .....	5
Figure 3 Van Krevelen plot .....	9
Figure 4 Shale matrix and pore components .....	13
Figure 5 Pyrogram comparison .....	15
Figure 6 Pyrolysis measurements and suggested breakdown.....	17
Figure 7 USGS Petrographic Atlas examples of reflected light microscopy .....	20
Figure 8 Pyrogram display of pyrolysis measurements.....	26
Figure 9 Tilt angle vs. secondary electron yield.....	32
Figure 10 Comparison of total porosities .....	38
Figure 11 Pseudo-van Krevelen plot .....	44
Figure 12 Microscopic x-ray fluorescence core sample.....	47
Figure 13 Microscopic x-ray fluorescence elemental maps .....	48
Figure 14 False-color microscopic x-ray fluorescence overlay maps .....	50
Figure 15 Reflected light microscopy images .....	52
Figure 16 Backscattered electron and wavelength-dispersive spectroscopy images from the electron microprobe.....	54
Figure 17 Secondary electron images.....	56
Figure 18 Backscattered electron images for samples of varying maturities .....	57
Figure 19 Lookup table histograms of 8-bit backscattered electron images .....	59

	Page
Figure 20 Grayscale 8-bit lookup table .....	61
Figure 21 Total porosity vs. bulk density .....	64
Figure 22 Comparison of as-received bulk densities .....	65
Figure 23 Comparison of water porosities .....	66
Figure 24 Comparison of total porosities with fluid substitution for retort .....	69
Figure 25 Comparison of hydrocarbon porosities .....	70
Figure 26 Comparison of S1 for Dean Stark and as-received extractions .....	71
Figure 27 Comparison of S1 for retort and as-received extractions .....	72
Figure 28 Comparison of S1 for Dean Stark and retort extractions .....	73
Figure 29 Comparison of S2 for Dean Stark and as-received extractions .....	75
Figure 30 Comparison of S2 for retort and as-received extractions .....	76
Figure 31 Comparison of S2 for Dean Stark and retort extractions .....	77
Figure 32 Shale matrix and pore components and corresponding pyrolysis measurements .....	79
Figure 33 Comparison of S2 for as-received, Dean Stark and retort extractions .....	80
Figure 34 As-received bulk densities vs. TOC (as-received and adjusted) .....	81
Figure 35 Mobility vs. measured maturity .....	84
Figure 36 Mobility vs. calculated maturity .....	85
Figure 37 8-bit grayscale backscattered electron images and corresponding histograms .....	88
Figure 38 Lookup table histogram of 8-bit backscattered electron images with compositional ranges .....	90

	Page
Figure 39 X-ray diffraction volume vs. backscattered electron area comparison: clay and quartz, calcite, pyrite, and TOC.....	93
Figure 40 Modified fire lookup table.....	95
Figure 41 8-bit backscattered electron images with modified fire lookup table .....	96
Figure 42 Backscattered electron images of foraminifera .....	98
Figure 43 False-colored backscattered electron images of foraminifera .....	99
Figure 44 Hydrostatic and lithostatic pressure curves and core pore fluid pressures.....	102
Figure 45 False-colored backscattered electron images of foram pyrite inclusions, cementation, and shell fracturing.....	103
Figure 46 Pore diagrams .....	104
Figure 47 Backscattered electron porosity vs. backscattered electron calcite content .....	106
Figure 48 Backscattered electron images of average calcium: fractured regions .....	107
Figure 49 Measured maturity vs. SEM pore space.....	108
Figure 50 Measured maturity vs. burial depth.....	111
Figure 51 Modified shale compaction curve and porosity vs. burial depth .....	112
Figure 52 Difference between total porosity estimated by compaction and Dean Stark estimation vs. maturity .....	113

## LIST OF TABLES

	Page
Table 1 Hydrocarbon generation stages and corresponding maturities .....	11
Table 2 Retort phases, temperatures, and corresponding extraction fluids.....	24
Table 3 Pyrolysis phases, rates, and corresponding measurements .....	25
Table 4 Grinding and polishing grit size, type, and time .....	29
Table 5 Densities of minerals and organics.....	34
Table 6 Porosity results .....	36
Table 7 As-received pyrolysis and LECO TOC results .....	41
Table 8 Post-Dean Stark pyrolysis and LECO TOC results .....	42
Table 9 Post-retort pyrolysis and LECO TOC results.....	43
Table 10 X-ray powder diffraction results .....	46
Table 11 Lookup table ranges and corresponding densities.....	92

## 1. INTRODUCTION

Organic pore space formation in hydrocarbon-rich shales, created as organic matter matures, has been investigated to determine relationships between organic porosity, organic character, and level of maturity. Calculating organic porosity in unconventional shales is complicated by a number of factors. First, several pore types exist within the shales: intergranular or intragranular pores within organic and inorganic phases contribute to effective porosity in distinctly different ways as hosts to fluids and transport properties. Second, different methods of determining porosity within tight, or low-porosity shales yield different results.

Organic porosity is thought to exist primarily within the organic matter (Jarvie, 2007; Bernard et al., 2012; Modica and Lapierre, 2012), suggesting that as the organic matter matures, pore space is created which contains the reacted hydrocarbon products within these organic pores. In this study, scanning electron microscopy (SEM) was utilized to characterize structural, petrophysical pore space within the organic matter. The SEM images and extracted pore space data have been compared with the hydrocarbon-filled porosity measurements to test/confirm organic porosity hypotheses. Micro-X-ray fluorescence (MicroXRF) was also performed to better understand the inorganic composition of the shale samples.

In this study, Dean Stark (toluene solvent extraction) and retort (thermal extraction) methods have been used to determine porosity and the results are compared. Previous observations have shown that total porosity in Dean Stark measurements is



consistently higher than total porosity estimated from retort (Burger et al., 2014).

Differences in each of these measurements have been evaluated to better understand what is defined as porosity in each extraction method.

Relationships between measured vitrinite reflectance (%R<sub>o</sub>) and porosity observations and measurements resulting from both the SEM imaging and extraction studies will be evaluated. Data from pyrolysis, specifically T<sub>max</sub>, which is the maximum amount of source potential (S<sub>2</sub>) measured during pyrolysis (Charest, 2013), has been used to estimate vitrinite reflectance (%R<sub>o</sub>) when %R<sub>o</sub> estimates are unavailable (Senftle and Landis, 1991). A relationship between R<sub>o</sub> and “mobile” hydrocarbons has been modeled and compared with effective porosity estimates.

### *1.1 Organic matter*

The term “organic matter” has various definitions amongst researchers. Curtis and coworkers include pyrobitumen, bitumen, and kerogen as components of organic matter (Curtis et al., 2012), while Modica and Lapierre do not include pyrobitumen as a component of the TOC (Modica and Lapierre, 2012). In many studies organic matter has not been characterized (Loucks et al., 2012; Passey et al., 2010; Slatt and O’Brien, 2011; Wang and Reed, 2009), while others categorize organic matter based on maturity rather than chemical components (Bernard et al., 2012). For this study, organic matter will be defined as pyrobitumen, bitumen, and kerogen.

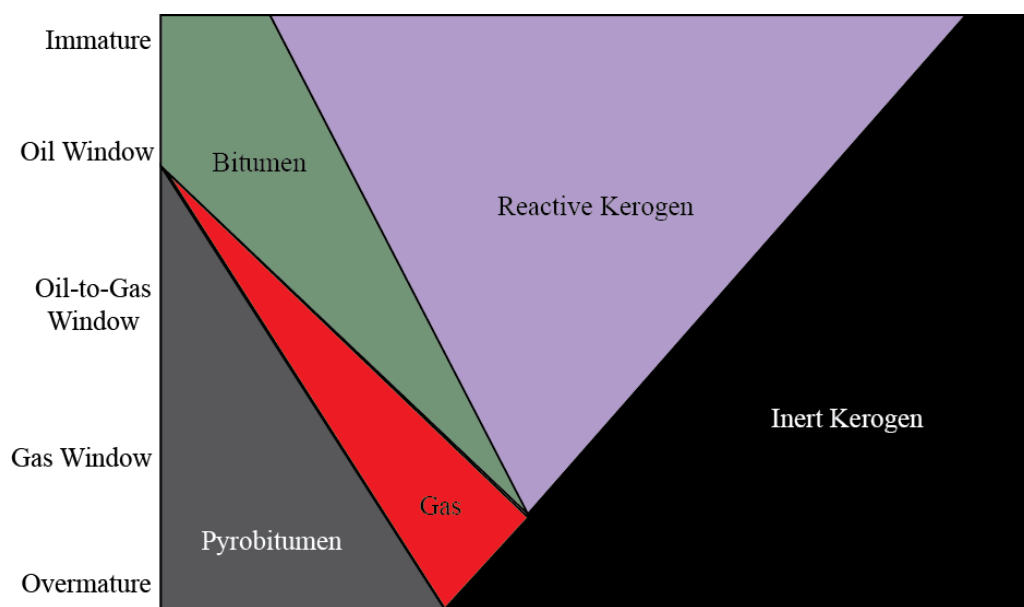


Figure 1. Organic matter maturation and generated products. Diagram of organic material constituents within unconventional shales represented as rough relative abundance throughout maturation. Based on Dembicki (2013)

Figure 1 illustrates some of the variation in definitions used in organic matter descriptions and changes in composition with thermal maturity. Organic matter is composed of soluble bituminous components and insoluble kerogen components, which range in density from 1.0 – 2.2 g/cc (Smith, 1969; Smith et al., 1994). Organic matter matures as a function of time and temperature, which depend, to first order, on burial depth (Al-mashramah, 2011). As the organic matter matures, the amount of pyrobitumen increases, bitumen increases and then decreases, reactive kerogen decreases, and inert kerogen increases. The insoluble pyrobitumen results from reacted bitumen; when overmaturation occurs, only pyrobitumen and inert kerogen remain (Dembicki, 2013).

Total Organic Content (TOC) is a measurable component of the organic matter. Three components of TOC exist: (1) organic carbon that has been retained within the system ( $C_{HC}$ ), (2) organic carbon that is able to be converted into hydrocarbons ( $C_C$ ), (3) and inert or residual carbon ( $C_R$ ). Carbon that has been expelled ( $C_E$ ) from the system as oil or gas is created within this system as seen in Figure 2 (Jarvie et al., 2007). TOC can be studied in order to understand the hydrocarbon generating history of the organic matter and calculate the original TOC ( $TOC_o$ ).

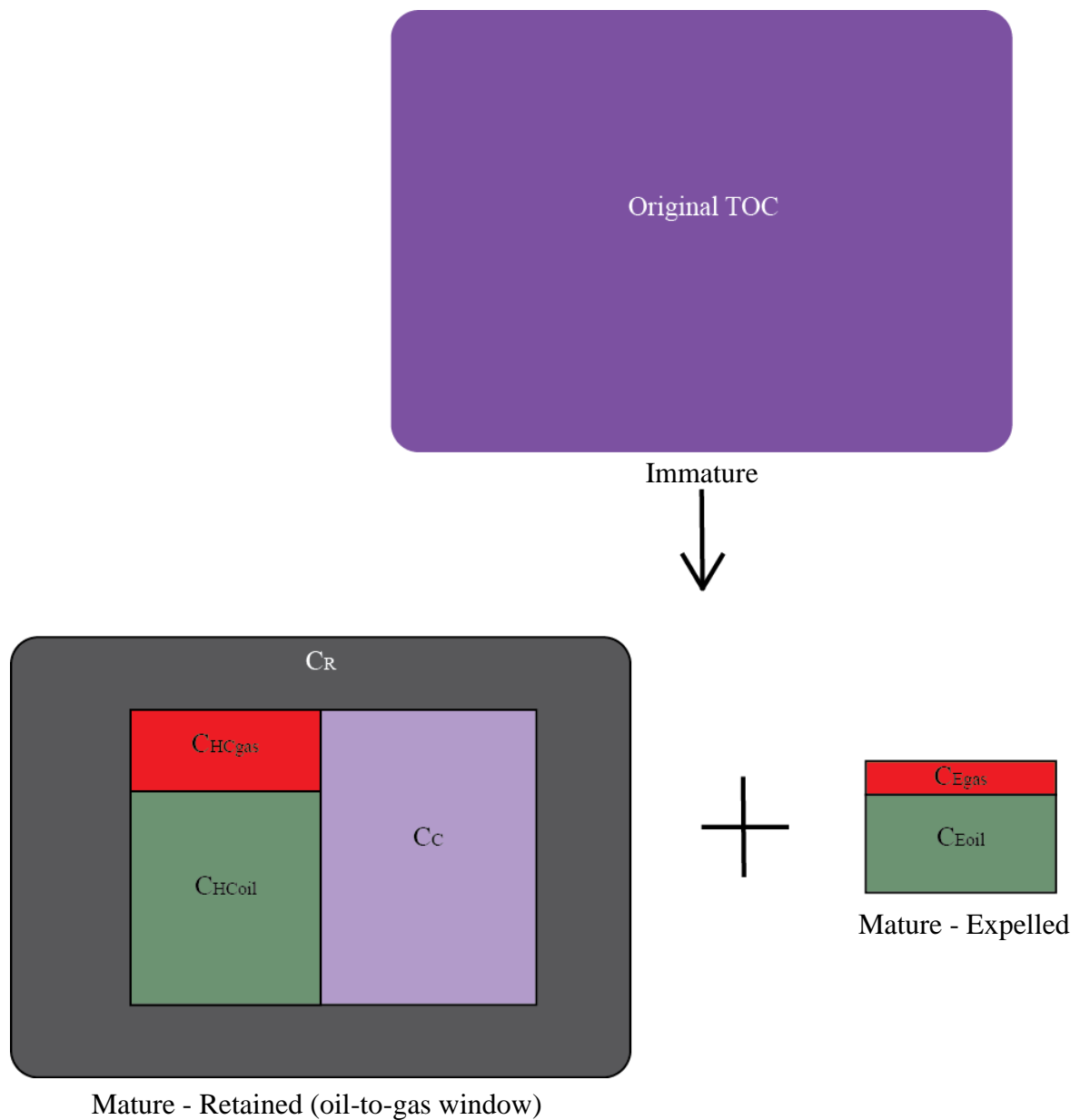


Figure 2. Total organic content evolution and expulsion. Diagram representing original total organic content (TOCo) and retained, or stored, organics along with expelled hydrocarbon liquid and gas components produced during maturation.  $C_R$  represents residual, inert carbon,  $C_C$  is remaining convertible carbon,  $C_{HCgas}$  and  $C_{HCoil}$  are gas and liquid components of retained hydrocarbons, and  $C_{Egas}$  and  $C_{Eoil}$  are gas and liquid hydrocarbons that have been lost through expulsion due to inadequate storage space within the organic pore system.

## 1.2 Porosity

Porosity is the measurement of void space within a rock. The void space can be a result of physical or chemical processes, which result in various types of pore spaces. Pore spaces are classified as intergranular, meaning between grains or linking grains, or intragranular, meaning contained within a grain. Pore spaces can take the shapes of spaces between grains, more equant spaces within grains, or fractures between and through grains. Porosity is also classified as organic or inorganic, referring to the material surrounding and forming the void space. This void space is typically filled with gas, liquid hydrocarbons, and/or water.

The presence of fluid within the pore spaces prevents the collapse of the pores as rock layers undergo burial and compaction. During burial, compaction is experienced by the rock and is dependent on effective pressure ( $P_e$ ) (Young et al., 1964; Neglia, 1979; Brace, 1980; Morrow et al., 1984; Dewhurst et al., 1998; Kwon et al., 2001). Effective pressure is calculated by:

$$P_e = P_l - \chi P_{pf} \quad (1)$$

Where  $P_l$  is the lithostatic pressure,  $P_{pf}$  is the pore fluid pressure, and  $\chi$  is approximately 1 for low strength rocks such as shales (Kwon et al., 2001; Terzaghi, 1923). The fluid within the pores reduces  $P_e$  enough to effectively maintain pore structures and prevent loss of storage space due to pore structure collapse (Fjaer et al., 2008).

The formation of hydrocarbon porosity is currently the subject of debate. Some workers believe that free hydrocarbons exist within pore spaces that develop as a result of organic matter decomposition (Jarvie et al., 2007). Modica and Lapierre (2012), on

the other hand, assert that these organically derived pore spaces are too small and water wet, making it difficult for the hydrocarbons to enter the pore spaces due to high capillary forces. Bernard et al. (2012) assert that the organic pore spaces are filled because the low porosity of the shales leaves no other pore spaces available for hydrocarbon storage. These studies indicate that a better understanding of the relationship between organic pore space and organic matter is required in order to evaluate the evolution of organics and pores in shales subject to burial and thermal geologic histories.

Hydrocarbon storage within shales is complicated due to gas storage. Gas is stored in shales by two different mechanisms, by which sorbed is stored in pores and fractures. Sorption occurs by (1) adsorption, in which gas molecules adhere to surfaces, and (2) absorption, by which gas molecules are dissolved into the organic material. Both processes are affected by the type of kerogen present, the level of thermal maturity, and the richness of the organic matter (Jarvie et al., 2007). In order to expel gases, the sorptive sites must be saturated with gas in the system (Pepper, 1992). Hydrocarbon estimation is also complicated by the unknown amount of expelled hydrocarbons in a system. It is not possible to quantify the expelled hydrocarbon in situ. Analyses must take into account (or at least acknowledge) the formation of hydrocarbons that have exited the system. While not readily measured, expelled hydrocarbons are vital to understanding the relationship between organic porosity and hydrocarbon formation. Given this, measurements of remaining hydrocarbons and porosity may offer a means to inferring hydrocarbons, expelled geologically and during reservoir management.

### *1.3 Kerogen type and maturity*

Both kerogen type and maturity influence the potential petroleum generation of organic matter. Four types of kerogen have been classified: I, II(S), III, and IV. These types are classified based on environment of deposition and they can be determined using a van Krevelen diagram (Fig. 3). A van Krevelen diagram plots the atomic ratios of Hydrogen:Carbon (H:C) and Oxygen:Carbon (O:C) against one another to determine kerogen type (Charest, 2013; Crain, 2014; Tissot et al., 1974). Alternate forms of these diagrams can also be used to determine kerogen type. The hydrogen index (HI) and oxygen index (OI) can act as proxies for H:C and O:C respectively and can be used to plot a pseudo-van Krevelen diagram (Dembicki, 2009; Espitalie et al., 1977; Peters, 1986; Baskin, 1997).

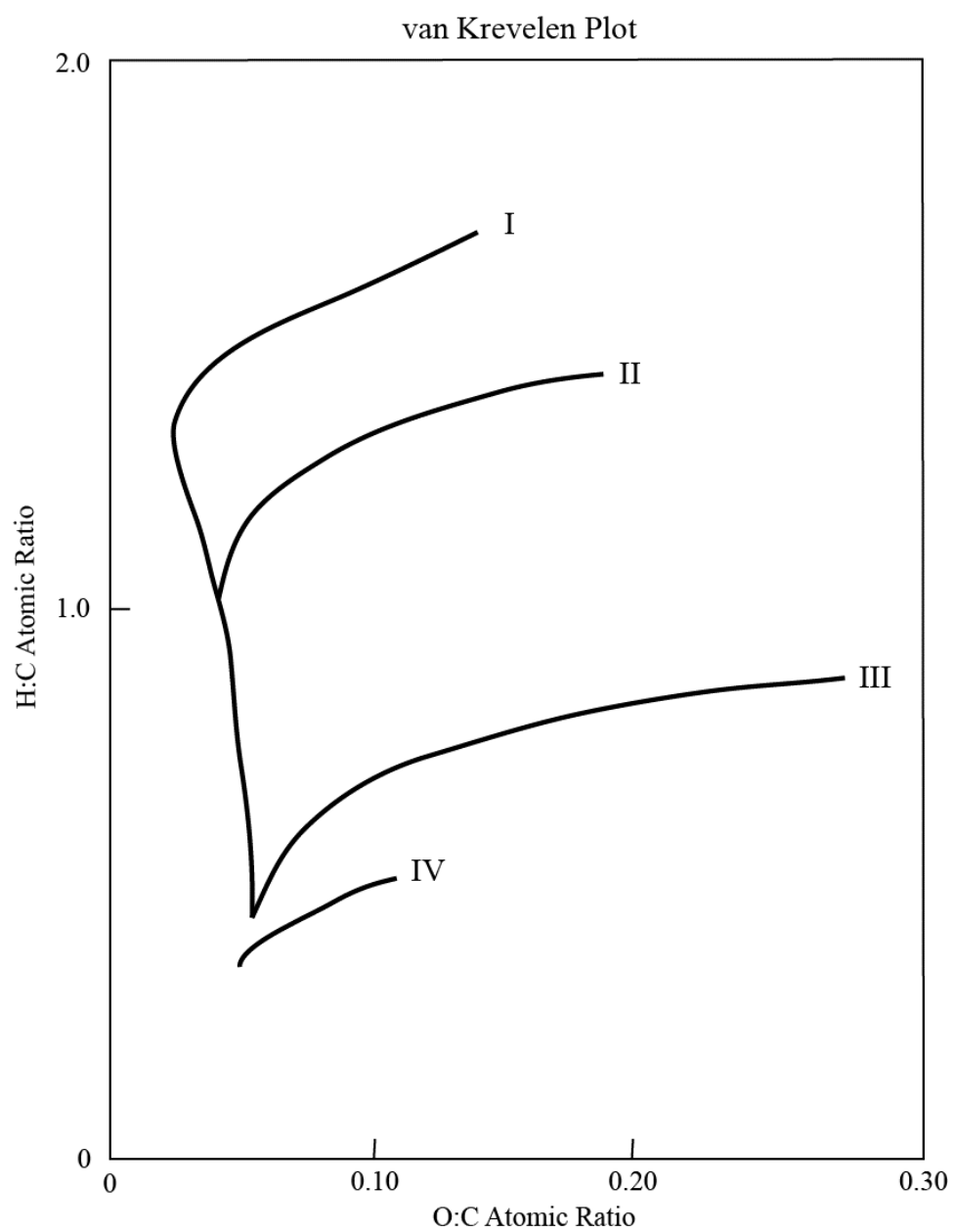


Figure 3. Van Krevelen plot. Oxygen:carbon atomic ratios are plotted against hydrogen:carbon atomic ratios to estimate kerogen type based on where the points plot between the I, II, III, and IV lines. Modified from Rice (1993).



Type I kerogen is deposited in lacustrine environments. Type I kerogen has the highest H:C ( $>1.5$ ) and lowest O:C ( $<0.1$ ) and tends to produce oil (Charest, 2013; Crain, 2014, Dembicki, 2009).

Type II kerogen is deposited in marine environments. Type II kerogen has the second highest H:C (1.1-1.3) and second lowest O:C and tends to produce primarily oil with some gas (Charest, 2013; Crain, 2014).

Type III kerogen is deposited in terrestrial environments. Type III kerogen has low H:C ( $<1.0$ ) and high O:C (0.2 – 0.3) and tends to produce primarily gas with some oil (Charest, 2013; Crain, 2014).

Lastly, type IV kerogen is also deposited in terrestrial environments but has very low H:C and high O:C. This form of kerogen does not tend to produce hydrocarbons due to its inert nature (Charest, 2013; Crain, 2014).

Kerogen type influences the type of hydrocarbon, gas or oil that may be generated once the organic matter reaches maturity. Maturity is normally measured by vitrinite reflectance (%Ro). Maturity for oil-prone and gas-prone generation is summarized in Table 1 (Dembicki, 2009).

Hydrocarbon Generation Stages and Corresponding Maturities			
Oil-Prone		Gas-Prone	
Generation Stage	% R <sub>o</sub>	Generation Stage	% R <sub>o</sub>
Immature	<0.6	Immature	<0.8
Early Oil	0.6-0.8	Early Gas	0.8-1.2
Peak Oil	0.8-1.0	Peak Gas	1.2-2.0
Late Oil	1.0-1.35	Late Gas	>2.0
Wet Gas	1.35-2.0		
Dry Gas	>2.0		

Table 1. Hydrocarbon generation stages and corresponding maturities. Table of oil-prone and gas-prone generation stages and corresponding maturities based on vitrinite reflectance values (%R<sub>o</sub>). Modified from Dembicki (2009), Dow (1977), and Senftle and Landis (1991).

It is important to understand the kerogen type and maturity level, because the kerogen type determines the proportion of organic carbon with potential of hydrocarbon generation. Type I kerogen has greater potential (as high as 80%) for converting organic carbon into hydrocarbons, while type III has a much lower potential (10-30%). These potentials are directly related to the H:C ratio; the greater the H:C ratio, the greater the potential for organic carbon to convert to hydrocarbons. This relationship gives insight into the history of the organic carbon maturation and potentially the porosity associated with it (Charest, 2013).

## 2. BACKGROUND

Shales, defined in this paper as clay to silt-sized grained ( $< 63 \mu\text{m}$  based on Wentworth (1922) grain-size classification) rocks that may or may not contain clays, and may act as both source and unconventional reservoir rocks. If they are high in organic carbon content, significant amounts of organic matter are typically trapped in these fine-grained rocks, and they mature during burial. As they mature, liquid and gas hydrocarbons are stored in pore space created within residual organic matter. Significant observations have been made which are relevant to organic porosity and its relationship to thermal maturity of kerogen (Jarvie, 2007; Bernard et al., 2012; Modica and Lapierre, 2012), but understanding the porosity and the fluids filling the pore space remains a challenge. As organic matter matures, oil, gas, bitumen, and other residual products are created (Fig. 2). Some hydrocarbons are expelled from the system, some are adsorbed by the system, and some are retained within the pore space of the system. Shales also contain water, which can fill the pore space, bind to clays, or support the clay network structurally in the form of  $(\text{OH}^-)$ . These complicating factors make direct correlations of porosity and hydrocarbon evolution within source-reservoir shales difficult. Categories of pore systems of unconventional shale reservoirs and fluids of these shales can be organized (Fig. 4) in relation to the formation of organic porosity and evolution of organic matter as hydrocarbons mature. My goal with this study is to advance our

understanding of porosity during the burial of shales and quantify the characteristics of porosity as they relate to thermal maturity. With this work, I aim to derive an equation relating maturity to “mobility,” the flowable/producing portion of hydrocarbons.

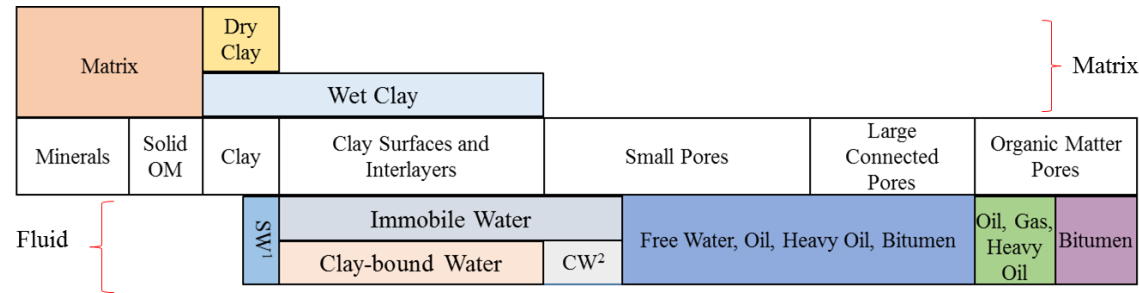


Figure 4. Shale matrix and pore components. Chart categorizing the matrix contributing components within unconventional shales and fluid types contributing to both the matrix structure and pore storage reservoirs. 1. SW – structural water, 2. CW – capillary water.

## 2.1 Bulk extraction measurements

Dean Stark and retort methods are the two methods most commonly implemented for measuring porosity in unconventional shales. Dean Stark is a solvent extraction (toluene for this study) of pore fluids, while retort uses thermal extraction. These methods, however, consistently fail to produce identical results, differing by an average of 1–2 porosity units (sometimes more), where units is defined as the percentage of space within a rock (Burger et al., 2014; Handwerger et al., 2012). This difference can be of great significance when determining economic viability of unconventional shales, which by definition have low porosities (typically less than 15%).

Petrophysical interpretations, which use these porosity, along with other well properties including density values are also commonly forced to use inflated matrix-contributing kerogen density values. Inflated kerogen densities may be linked to inaccurate quantification of pore fluids, and a better understanding of extraction components is necessary for improved estimation of well characteristics.

Recent studies disagree on whether solvent extraction by the Dean Stark method is a clear approach for determining porosity (Collins and Lapierre, 2014; Burger et al., 2014). Burger et al. (2014) suggest that Dean Stark may overestimate porosity due to extraction of solid organic matter. Collins and Lapierre (2014) use Dean Stark results combined with pyrolysis data in order to isolate heavier soluble components of the organic matter and determine the total quantity of bitumen within a sample based on the amount of free hydrocarbons (S1) and the amount of hydrocarbons created by thermal cracking of nonvolatile organic matter (S2) measurements. Quantifying the bitumen component requires first finding the difference between the original, or “as-received,” S2 value and the post Dean Stark S2, which is defined as S1’ and then adding S1’ to S1 for a total bitumen, in weight percent, quantity. The formula is:

$$Total\ Bitumen = S1_{DS} + (S2_{AR} - S2_{DS}) \quad (2)$$

where:

$$S2_{AR} - S2_{DS} = S1' \quad (3)$$

Plotted pyrograms can be plotted together to visualize the differences in S1 and S2 peaks (Fig. 5).

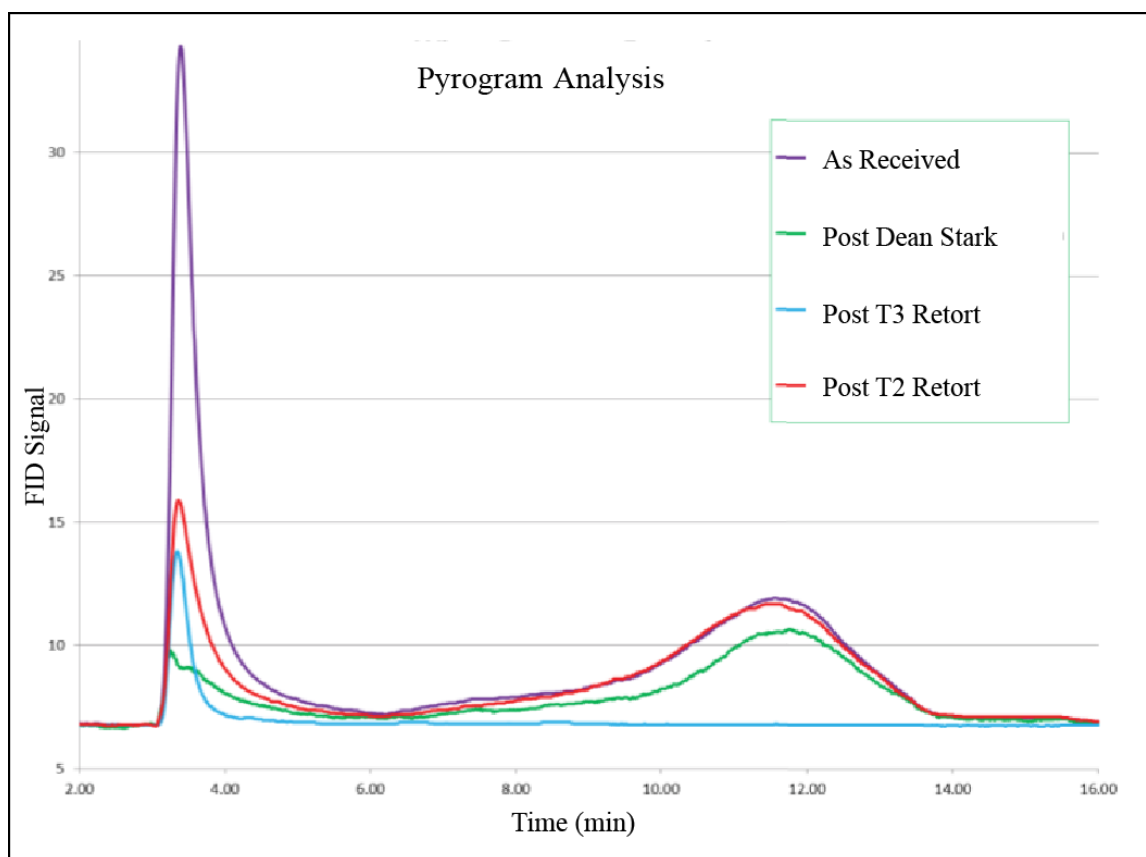


Figure 5. Pyrogram comparison. Resulting pyrograms from as-received, post Dean Stark, Post T3 (704°C) retort, and Post T2 (315°C) pyrolysis. Pyrograms are plotted as flame ionization detector (FID) signal, in millivolts as a function of time in minutes. Two distinct peaks appear, the first represents S1, free hydrocarbons measured within the system, and the second represents S2, or the organic potential of the system.

S1 is represented by the first observed peak and S2 is represented by the second peak. With processing of the sample, from the as-received sample to the post-Dean Stark sample considerable decreases are detected. In the S1 peak and the S2 peak post-retort analyses are complicated by the reappearance of an S1 peak following extraction, which will be addressed later.

Jarvie (2012) presented a similar calculation in order to quantify total oil by thermal extraction:

$$Total\ Oil = (S1_{AR} - S1_{extracted\ rock}) + (S2_{AR} - S2_{extracted\ rock}) + EL \quad (4)$$

where EL represents evaporative loss of oil. However, this calculation does not address the question of what is measured by the change in S1 of the rock, or  $S1_{extracted\ rock}$ . If  $S1_{extracted\ rock}$  is greater than zero, then either the extraction process is not complete and free hydrocarbons remain within the pore system or unexpected cracking of new hydrocarbons is occurring during the thermal extraction (retort) process which creates additional free hydrocarbons within the system. Jarvie (2012) presented a diagram, based on Equation 4, which can be applied to both his results and those of Collins and Lapierre (2014) for S1 and S2 measurements (Fig. 6).

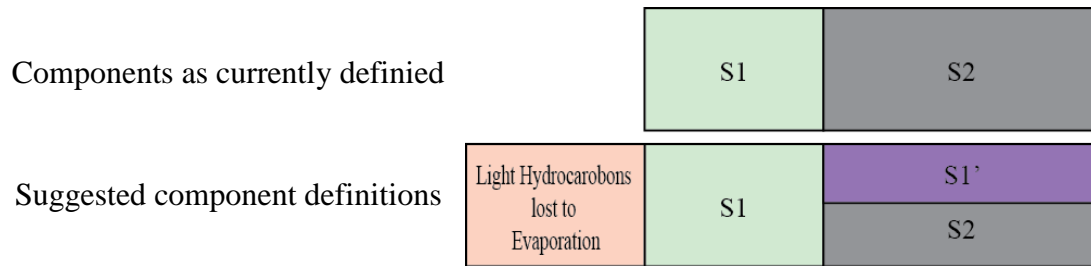


Figure 6. Pyrolysis measurements and suggested breakdown. Diagram representing the differences between pyrolysis measurements, S1 and S2, and interpretations of organic constituents of unconventional shales. S1' is representative of the immobile bitumen that is soluble but not mobile. S2 is interpreted as the insoluble component only. Current definitions also fail to account for evaporative loss of light-end hydrocarbons. Modified from Jarvie (2012).

Both the Dean Stark and Retort methods must be investigated further in order to understand the implications of these calculations and apply them to predict the effective porosity of unconventional shales accurately.

Technological advances in studying unconventional reservoir shales are quickly evolving. It has only been within the last 20 years that the Gas Research Institute introduced the crushed shale technique, called GRI, for analyzing low-porosity unconventional rocks (ResTech, 1996). GRI facilitates Dean Stark measurements by creating access for the solvent to extract the pore fluids, which would otherwise be impractical because of the low permeabilities of fine-grained rocks. Retort measurements also requires crushed sample preparation for practical measurements. Theoretically, Dean Stark and retort measurements should produce similar results (Handwerger et al., 2011), though close analyses have indicated results differ (Collins



and Lapierre, 2014; Burger et al., 2014; Jarvie, 2012).

## *2.2 Microstructural observations and imaging*

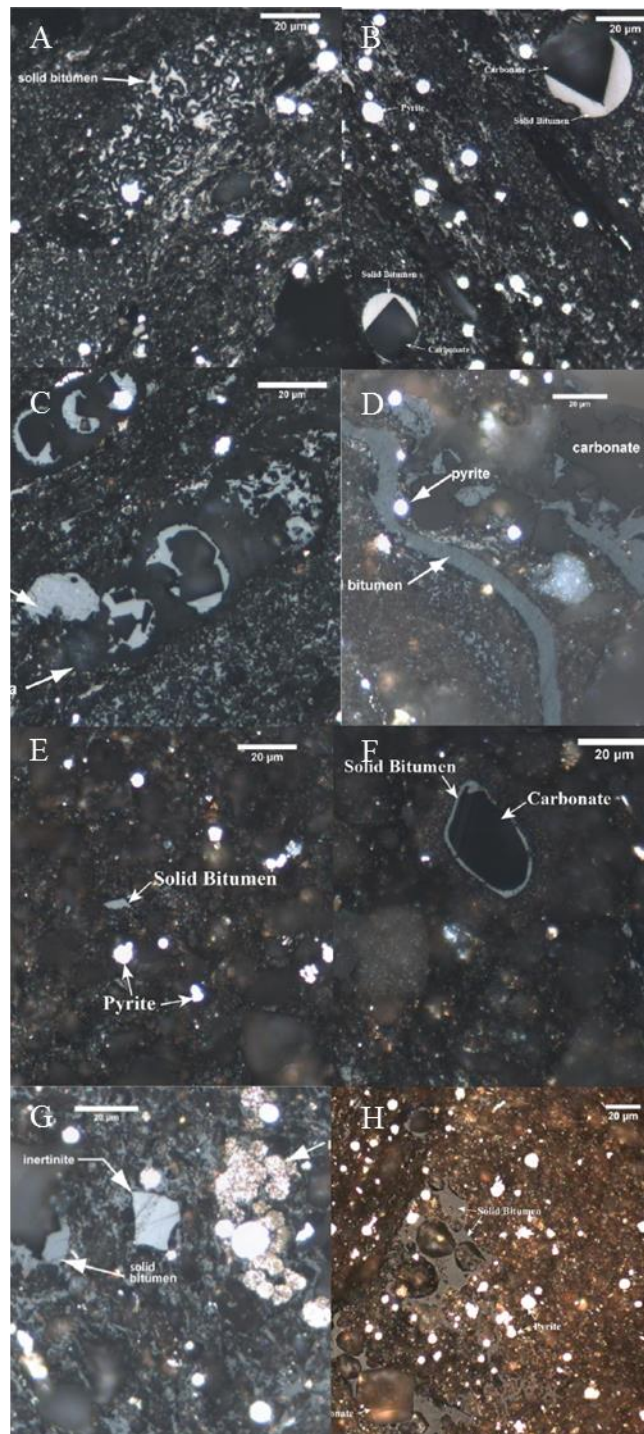
One obstacle that must be overcome to resolve differences between these measurements is to image the organic matter that releases organic constituents. Studies have been carried out imaging organic matter in shales (Loucks et al., 2012; Camp and Wawak, 2013; Lemmens and Richards, 2013; Spain and McLin, 2013; Jennings and Antia, 2013) in which organic matter is identified by morphology and density. Analyses of chemical or other physical properties have not been carried out to identify organic matter unambiguously, and processes that are capable of accurately applying these techniques are expensive, time-consuming, and not easily accessible.

Organic matter is identified in reflected light by its color, which may or may not be reliable, and primarily by its morphology, with amorphous forms. Organic matter tends to fill available pore spaces and act as both matrix and pore fluid as it matures. The U.S. Geological Survey (2011) has compiled a petromicrograph atlas of reflected light images (Fig. 7) of porosity, based on incident white light and fluorescent light methods, which can be used for reference when attempting to image organic matter in core samples.

Loucks (2012) presented scanning electron microscope (SEM) images using backscattered electrons (BSE) of organic matter, which illustrate differences in BSE intensity as a function of density. Given a constant set of SEM conditions, grayscale values in BSE images can be compared with lookup table numbers (LUT #), to estimate

density differences of solid phases, with the brightest colors (highest LUT # - near white) representing the highest densities and the darkest colors (lowest LUT # - near black) representing the lowest densities (Camp and Wawak, 2013). Organic matter has a relatively low density ( $0.8 - 2.2 \text{ g/cm}^3$ ), compared to other common matrix minerals in shales: quartz ( $2.65 \text{ g/cm}^3$ ), clays ( $2.6 - 3.4 \text{ g/cm}^3$ ), and calcite ( $2.71 \text{ g/cm}^3$ ) (Kane, 2007; Smith et al., 1994; Roberts, Campbell, and Rapp, 1990). The low density of organic matter and pore space are imaged at the darkest end of the grayscale, which allows us to isolate and identify the organic matter using BSE for imaging. Confirming these qualitative identification techniques with more accurate quantification techniques, which rely on chemical identification, could provide a more accurate means of imaging and quantifying organic matter in unconventional reservoirs.

Figure 7. USGS Petrographic Atlas examples of reflected light microscopy. A guide for identification of organic and mineral components of unconventional reservoir shales. (A) Bossier shale: 2.09 %Ro and 4.36 %wt TOC, (B) Bossier shale: 2.09 %Ro and 6.89 %wt TOC, (C) Eagle Ford shale: 1.36 %Ro, (D) Eagle Ford shale: 1.096 %Ro and 4.36 %wt TOC, (E) Haynesville shale: 1.85 %Ro, (F) Haynesville shale: 1.93 %Ro and 2.96 %wt TOC, (G) Marcellus shale: 0.96 %Ro, (H) Haynesville shale: 0.93 %Ro (Reprinted with permission from U. S. Geological Survey, 2011).



### 3. METHODS

#### 3.1 Porosity estimates

Two different methods of obtaining porosity were compared: Dean Stark analysis which depends on solvent extraction and retort analysis which depends on thermal extraction. In neither is porosity directly measured, but porosity ( $\phi$ ) can be calculated from volumetrics:

$$\phi = \frac{V_{pore}}{V_{bulk}} = \frac{V_{bulk} - V_{grain}}{V_{bulk}} \quad (5)$$

where  $V_{pore}$  is the volume of the pore space,  $V_{bulk}$  is the bulk volume of the sample, and  $V_{grain}$  is the dry, or extracted, matrix volume (Luffel, Guidry, and Curtis, 1992; Collins and Lapierre, 2014). In this study, the Dean Stark (solvent extraction) method will be compared to the retort (temperature extraction) method. Because of the low permeability of these shale cores ( $\kappa \sim 3.0 \times 10^{18} - 8.0 \times 10^{13} \mu\text{m}^2$ ) within the unconventional shales, both extraction processes require crushing samples to powders (particle size  $\sim 0.5 - 0.85 \text{ mm}$ ) before carrying out the extraction process.

##### 3.1.1 Dean Stark: solvent extraction

Dean and Stark (1920) introduced this solvent extraction method typically using toluene, to extract water and hydrocarbons from the rock sample. When applying the Dean Stark technique to unconventional shales, samples must be crushed using the GRI procedure before extraction (Luffel and Guidry, 1992). The resulting crushed sample is then treated with the organic solvent until the water volume no longer increases (about

one week). Once the fluids, water and hydrocarbons, are extracted they undergo distillation during which time hydrocarbons are lost and water is collected. Water volume is measured directly, by mass measurement, while the oil volume is inferred based on the sample mass difference pre and post-extraction. Only total water saturation and total oil saturation are reported, and total porosity includes all of the extracted hydrocarbons.

### *3.1.2 Retort: thermal extraction*

The retort extraction method liberates volatiles by heating, which evolves through three temperature steps, 121 °C, 315 °C, and 704 °C (250 °F, 600 °F, and 1300 °F). This extraction method, like Dean Stark extraction, also requires the samples to be crushed when applied to unconventional reservoir shales. At 121 °C (T1), free and capillary water are extracted and collected. At 315 °C (T2), clay bound water and free oil are extracted and collected. At 704 °C (T3), structural water and “bound” oil are extracted and collected. Table 2 summarizes the extraction phases for T1, T2, and T3. Effective and total porosities are reported; the total porosity does not include the hydrocarbons released from 315 to 704 °C, and therefore the data from T3 will not be included in this study. Water and oil saturations are measured directly during retort extraction.

Retort Phases, Temperatures, and Corresponding Extraction Fluids				
Phase	Temperature (°C)	Temperature (°F)	Extracted Water Type	Extracted Hydrocarbon Type
T1	121.1	250.0	Free and Capillary Bound	-
T2	315.6	600.0	Clay Bound Water	Free
T3	704.4	1300.0	Structural Water	Bound

Table 2. Retort phases, temperatures, and corresponding extraction fluids. Table of retort extraction phases (T1, T2, and T3) with their corresponding temperatures, types of water extracted, and types of hydrocarbons extracted for each phase of the process.

The reported values for total porosity of each method are observably different. The porosity data from these two methods will be compared and contrasted in order to determine distinct differences in measurements. I will analyze the saturation data along with pyrolysis and LECO TOC, with the goal of understanding the nature of porosity in fine-grained unconventional reservoir rocks.

### *3.2 Pyrolysis and LECO total organic content methods*

Pyrolysis analyses on shale samples was performed in order to understand the properties of the organic matter contained in the samples. Pyrolysis measures S1, S2, S3, and the peak temperature of hydrocarbon release  $T_{\max}$  through heating in an inert helium atmosphere (Table 3) (Ocean Drilling Program, 2014). S1 is the amount of free hydrocarbons in the system, S2 is the amount of hydrocarbons generated through thermal cracking (the potential), S3 is the amount of  $\text{CO}_2$  which is related to the type and potential reactivity of the organic matter, and  $T_{\max}$  measures the peak temperature of S2, or maximum amount of hydrocarbon released from kerogen cracking during pyrolysis.

Pyrolysis Phases, Rates, and Corresponding Measurements				
Phase	Temperature (°C)	Time/Rate	Measurement	Measured Substance
1	300.0	3 min	S1	Free Hydrocarbons (mg HC/g Rock)
2	300.0-550.0	25 °C/min	S2, T <sub>max</sub> **	HC Generated through Thermal Cracking (mg HC/g Rock)
3	390.0-300.0*	Variable	S3	CO <sub>2</sub> Generated from Pyrolysis (mg CO <sub>2</sub> /g Rock)

Table 3. Pyrolysis phases, rates, and corresponding measurements. Table of pyrolysis phases (1, 2, and 3) with their corresponding temperatures, types of water extracted.

\*During Phase 3, samples are cooled from 390–300°C. \*\*T<sub>max</sub> represents the peak temperature of S2.

T<sub>max</sub> can be used to determine the maturity of hydrocarbons initially in the shale, in terms of vitrinite reflectance (Ro) using the formula from Zdanavičiūtė and Lazauskienė, (2009):

$$R_{o_{Calculated}} = 0.180T_{max} - 7.16 \quad (6)$$

Pyrolysis requires 100 mg of crushed sample in helium atmosphere to be heated, while a flame ionization detector (FID) identifies hydrocarbons generated. An Omega type K (calibration) thermocouple fitted with a resistance temperature detector used for the splitter monitors the temperature within the system. As the system temperature rises, the FID records 3 primary peaks throughout time (temperature). These peaks represent (in order) S1, S2, and S3. T<sub>max</sub> is determined by the temperature of maximum hydrocarbon generation. The measured parameters obtained during pyrolysis (i.e. S1, S2, S3, and T<sub>max</sub>) can be plotted as FID versus time (or temperature) (Fig. 8) (Clementz, 1979; Espitalie et al., 1977; Espitalie, Marquis, and Barsony, 1984; Espitalie, Deroo, and Marquis, 1985; Peters, 1986)



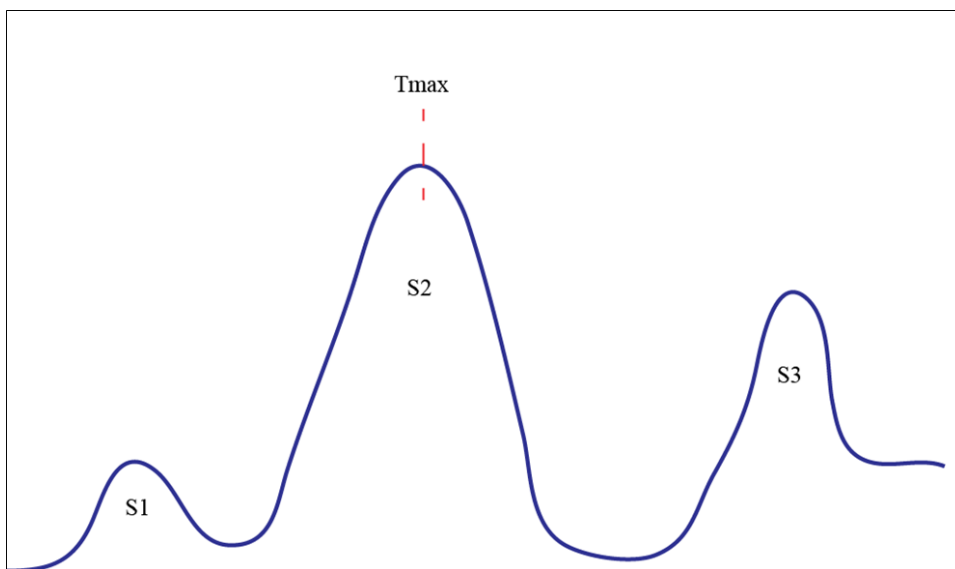


Figure 8. Pyrogram display of pyrolysis measurements. This diagram illustrates pyrolysis measurements including S1, S2, S3, and  $T_{\max}$  from Peters (1986).

TOC is measured separately, using a LECO C230 instrument. Sample material undergoes combustion within the LECO C230, during which time  $\text{CO}_2$  is created and detected by a non-dispersive infrared detector (NDIR). The quantity of the  $\text{CO}_2$  generated is compared with the original sample weight to determine the percent carbon within the sample and is reported as TOC (Ellington and Associates, 2015; Tissot, Espitalie, and Combaz, 2015).

Pyrolysis and LECO TOC were performed on the Dean Stark samples and retort samples, both as-received and post extraction.

### *3.3 Compositional analysis of the rock matrix*

Compositional analyses were performed at multiple scales in order to quantify the matrix and pore-filling materials of the shale core samples. At the core scale, X-ray powder diffraction (XRD) was performed in order to quantify various organic and crystalline inorganic phases. Samples from the core also underwent microscopic X-ray fluorescence (MicroXRF), which allows for compositional analysis of intact (not powdered) samples. Polished plates were made from the samples following MicroXRF analyses and mapped by electron microprobe wavelength-dispersive spectroscopy (WDS) with the goal of identifying organic matter at the micron scale.

#### *3.3.1 X-ray powder diffraction*

X-ray powder diffraction was performed to identify and quantify the crystalline phases of shale core by analyzing their diffraction patterns (Klug and Alexander, 1954). The XRD analysis underwent Reitveld refinement with the goal of improved XRD results.

Reitveld refinement is a minimization process which aims to increase the resolution of overlapping peaks in order to more clearly identify XRD signatures and quantify the quantities of different minerals that make up the shale. The need to apply the Reitveld method stems from limitations of XRD, which include: diffraction peak overlap, inaccuracy, and preferred orientation (non-random crystal distribution) (Will, 2006).

The Reitveld refined XRD data will allow base estimates of calcite, clay, kerogen, quartz, and pyrite. These values, quantified by volume percent, serve as a guide for understanding the solid phases imaged at various scales.

### *3.3.2 Microscopic X-ray fluorescence*

While useful to identify crystalline phases, bedding, phase distributions and microstructures cannot be detected using powder XRD. In order to identify and isolate areas of interest for imaging, microscopic X-ray fluorescence (MicroXRF), was used to map phase distributions of samples taken from the shale core using a Horiba XGT-7000 instrument.

MicroXRF is a technique in which a cross-section of a sample is analyzed by exposing the sample to X-rays in the form of a beam. The X-rays excite electrons and lead to fluorescence, which is collected and interpreted for elemental composition (Janssens, Adams, and Rindby, 2000).

The samples were approximately 10 – 20 mm thick. The processed area for each sample was 2.56 x 2.56 cm<sup>2</sup>. The 100 µm resolution of the MicroXRF allows for identification of highly calcitic regions and significant differences in composition throughout the sampled area. This non-destructive analysis, along with processing techniques using ImageJ Software, was used to identify areas that were then imaged using reflected light, secondary electrons (SE), and backscattered electrons (BSE) (Rasband, 2014).

### 3.3.3 Electron microprobe: wavelength-dispersive spectroscopy

After samples underwent MicroXRF representative regions of samples were prepared as polished plates for electron microprobe analyses. These samples were ground and polished to a final thickness of  $\sim 100\ \mu\text{m}$  using a sequence of grit sizes and powder types indicated in Table 4:

Grinding and Polishing Grit Size, Type, and Time		
Grit Size ( $\mu\text{m}$ )	Powder Type	Time (min)
34.3	SiC	5.0
14.5	$\text{Al}_2\text{O}_3$	5.0
9.5	$\text{Al}_2\text{O}_3$	5.0
3.0	$\text{Al}_2\text{O}_3$	8.0
0.3	$\text{Al}_2\text{O}_3$	10.0

Table 4. Grinding and polishing grit size, type, and time. Grinding and polishing grit sizes listed in microns. Composition of grit powders, and polishing time for each grit size listed in minutes.

After polishing, the samples were imaged using reflected light microscopy and then carbon-coated in preparation for secondary electron microscopy (SEM) and microprobe analyses.

A Cameca SX50 electron microprobe was utilized to obtain elemental analyses through wavelength-dispersive spectroscopy (WDS) analyzing for  $\text{Al}_2\text{O}_3$ ,  $\text{CaCO}_3$ ,  $\text{FeS}_2$ ,  $\text{PO}_4$  and  $\text{SiO}_2$  with the goal of identifying organic (and inorganic) phases at the microscale (near  $\mu\text{m}$  resolution).

WDS is a form of x-ray spectrometry in which x-rays of isolated wavelengths are measured by diffraction from single-crystals of the instrument detectors tuned to a given Bragg's angle for each element. The relationship between this angle and the wavelength can be explained by Bragg's law:

$$n\lambda = 2d\sin\theta \quad (7)$$

where  $n$  represents the reflection order,  $\lambda$  is the wavelength of the x-ray,  $d$  is the interplanar spacing, and  $\theta$  is the Bragg angle (Reed, 2005).

Digital element maps were created using WDS by representing photon counts through pixel brightness levels, with the brightest pixels representing highest photon counts. Aluminum, calcium, carbon, iron, silicon, and sulfur maps were obtained and processed using ImageJ software.

### *3.4 Microscopic imaging*

Samples were imaged at multiple scales using reflected light, secondary electron (SE), and backscattered electron (BSE) microscopy. In preparation for scanning electron microscopy (SEM) through both SE and BSE, the polished plates were carbon-coated to prevent electron charging during imaging. This carbon-coat was applied after the sections were observed by reflected light microscopy (using a Zeiss Axioplan 2 Imaging microscope with a Zeiss AxioCam HRc camera). All SEM work was done using a FEI Quanta 600 FE-SEM, at a working distance of 10 mm and a field-emission electron beam grounded at 10 kV.

#### *3.4.1 Reflected light microscopy*

Reflected light microscopy was chosen over transmitted light microscopy because of the nature of the unconventional reservoir shale samples. These shales, whose primary components are calcite, clays, and organic solids (Moh's hardness 1 – 4), are very soft and difficult to prepare as thin ( $\sim 30\text{ }\mu\text{m}$ ), polished sections for transmitted light microscopy. The dark color of the organic matter also makes reflected light a better choice for imaging these samples at 10x, 20x, and 50x magnification.

#### *3.4.2 Scanning electron microscopy: secondary electron imaging*

Secondary electron (SE) was selected for imaging initial observations of shale samples. To obtain SE images, secondary electron yield is measured and related to the tilt angle (Fig. 9), which is representative of the topography of the sampling area (Reed, 2005). Image resolution for SE images using the FEI Quanta 600 FE-SEM can be accomplished on the nanometer scale.

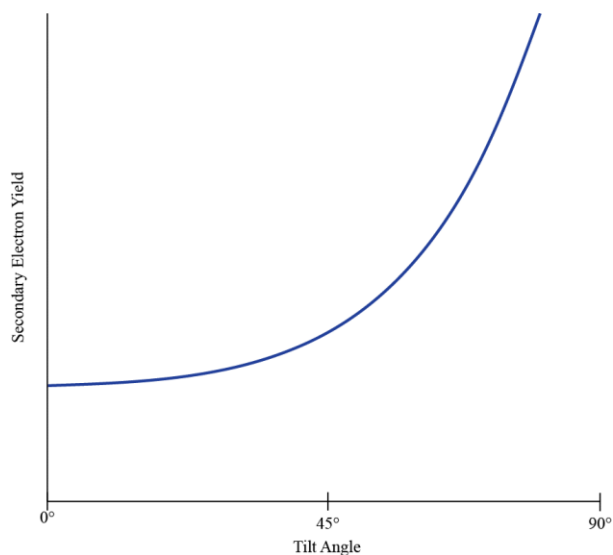


Figure 9. Tilt angle versus secondary electron yield. Used for interpreting topography of secondary electron images based on Reed (2005).

### 3.4.3 Scanning electron microscopy: backscattered electron imaging

Backscattered electrons (BSE) were used to image samples for variations in phase density. Pixel brightness in BSE images can be related to atomic number,  $Z$ , of the phase's components. BSE detectors collect and analyze the fraction of backscattered electrons from the sample surface. Elements with highest  $Z$  values are the heaviest elements and contribute to the highest phase densities of the sample.

Processing of the BSE images was done using ImageJ Software. Lookup tables (LUT) were prepared with LUT numbers that can be related to density values of known elements (Table 5). Identifying locations of phases by this method was tested by comparing with volume fractions of phases based on bulk, powder XRD analyses.

Image resolution for BSE images using the FEI Quanta 600 FE-SEM can be accomplished on the micron scale.

### *3.5 Upscaling: petrophysical applications*

The porosity measurements, SEM, and MicroXRF data are measured and analyzed on the micrometer to centimeter scale but would be useful to interpret at a larger, reservoir-wide meters to kilometers scale. In order to accurately upscale this information, more information would be necessary. For example, at reservoir scales, porosity may depend on fractures that are not included in core samples, with significant implications for storage of fluids and permeability. Measurements within the fractured sections were taken in order to include fracture influence within the model, but without more information it remains unclear how to upscale the microscopic measurements.



Densities of Minerals and Organics	
Mineral(oid)	Density (g/cm <sup>3</sup> )
Coal Gas	0.58
Crude Oil	0.80-0.94
Kerogen	0.80-1.50
Vitrinite	1.28-1.70
Bitumen	1.30-2.03
Montmorillonite (Smectite)	2.00-3.00
Pyrobitumen (Graphite)	2.09-2.23
Mixed-Layer Clay (Illite/Smectite)	2.60-2.90
Plagioclase (Albite)	2.60-2.63
Kaolinite	2.60-2.63
Illite	2.60-2.90
Quartz	2.65
Calcite	2.71
Dolomite	2.85
Mica (Biotite and Muscovite)	2.77-3.40
Apatite	3.15-3.20
Marcasite	4.875
Pyrite	5.013

Table 5. Densities of minerals and organics. Table of densities for common organic and mineralogical phases of unconventional reservoir shales (Roberts, Campbell, and Rapp, 1990; Smith, 1969; Smith et al., 1999).

## 4. RESULTS

30 sampling locations, 5 each from 6 cores of varying maximum burial depths (from 1470 to 2650 m), effective pressures (from 12.51 to 18.25 MPa), and maturities (from 0.935 to 1.45 %Ro), were measured using both Dean Stark and retort extraction techniques. Each sampling location provided 2 individual samples (approximately 100 g each) for testing in order to conserve comparable sampling material properties. Pyrolysis and LECO TOC were performed on the 30 sampling locations before extraction, and all 60 of these samples underwent pyrolysis and LECO TOC analysis following extraction.

### *4.1 Porosity observations*

Dean Stark and retort extraction methods provide several measurements including as-received (AR) bulk density, dry grain density, water saturation, oil saturation, gas saturation, and dry helium porosity. These measured values are used to calculate the porosities (total, water, and hydrocarbon) using well-established relationships (See Appendix A). The 30 sampling locations with their corresponding measured densities and calculated porosities, along with available corresponding measured vitrinite reflectance (%Ro) are listed in Table 6.

Differences can be observed when comparing calculated Dean Stark and retort porosities. Total porosities are 0.1-6.0 porosity units (PU) different, with Dean Stark porosities tending to be greater than those from retort determinations. Plotting the

Porosity Results												
Dean Stark								Retort				
Core	Sample	Measured %R <sub>a</sub>	AR ρ <sub>bulk</sub> (g/cc)	Dry ρ <sub>grain</sub> (g/cc)	Φ <sub>t</sub> (% of BV)	Φ <sub>HC</sub> (% of BV)	Φ <sub>w</sub> (% of BV)	AR ρ <sub>bulk</sub> (g/cc)	Dry ρ <sub>grain</sub> (g/cc)	Φ <sub>t</sub> (% of BV)	Φ <sub>HC</sub> (% of BV)	Φ <sub>w</sub> (% of BV)
C1	1B	1.25	2.283	2.581	13.4	9.6	3.7	2.263	2.556	12.4	10.2	2.2
C1	2B	1.27	2.260	2.571	14.1	10.9	3.1	2.250	2.553	12.8	10.8	2.0
C1	3B	1.23	2.349	2.599	11.3	8.5	2.8	2.351	2.589	9.8	8.5	1.3
C1	4B	1.19	2.326	2.662	13.3	12.3	1.0	2.283	2.570	11.9	10.2	1.7
C1	5B	1.17	2.377	2.623	11.0	7.4	3.6	2.356	2.608	10.5	8.5	2.0
C2	21B	-	2.486	2.608	6.8	3.8	2.4	2.314	2.563	10.8	8.7	2.1
C2	22B	-	2.402	2.628	10.4	4.6	1.4	2.437	2.613	7.4	6.2	1.2
C2	23B	-	2.422	2.621	9.8	4.9	2.0	2.343	2.584	10.2	8.5	1.7
C2	24B	-	2.405	2.624	10.8	4.7	3.0	2.328	2.564	10.4	8.2	2.2
C2	25B	-	2.422	2.627	9.6	3.8	1.8	2.378	2.571	8.2	7.0	1.2
C3	11B	-	2.353	2.573	10.0	7.9	2.1	2.308	2.562	10.9	9.0	1.9
C3	12B	-	2.350	2.596	10.7	8.9	1.8	2.353	2.585	9.5	8.4	1.1
C3	13B	-	2.409	2.651	10.0	8.5	1.5	2.341	2.597	10.6	9.0	1.7
C3	14B	-	2.417	2.611	8.6	6.5	2.1	2.327	2.574	10.3	8.7	1.6
C3	15B	-	2.270	2.551	12.5	9.7	2.9	2.287	2.555	11.6	9.5	2.1
C4	26B	-	2.334	2.607	13.2	10.1	3.1	2.312	2.546	10.4	8.4	2.0
C4	27B	-	2.394	2.605	10.4	7.9	2.4	2.266	2.514	11.1	9.4	1.7
C4	28B	0.935	2.331	2.597	12.8	10.1	2.7	2.393	2.573	8.0	6.4	1.7
C4	29B	-	2.342	2.616	13.0	9.8	3.3	2.302	2.538	10.5	8.8	1.8
C4	30B	0.98	2.323	2.603	13.2	10.5	2.6	2.312	2.548	10.6	8.5	2.0
C5	16B	-	2.444	2.606	7.7	5.5	2.2	2.460	2.620	6.8	5.5	1.3
C5	17B	-	2.456	2.625	7.8	5.0	2.8	2.533	2.666	5.5	4.7	0.8
C5	18B	1.05	2.517	2.659	6.7	4.7	2.0	2.451	2.602	6.6	4.9	1.7
C5	19B	-	2.423	2.608	8.7	5.4	3.4	2.471	2.624	6.8	4.9	1.8
C5	20B	-	2.430	2.598	8.1	5.7	2.4	2.433	2.589	7.0	4.8	2.2
C6	6B	1.41	2.248	2.578	14.7	11.3	3.4	2.256	2.556	12.7	10.9	1.9
C6	7B	-	2.273	2.608	14.6	10.5	4.1	2.330	2.601	11.4	9.7	1.7
C6	8B	-	2.371	2.589	10.2	6.6	3.6	2.275	2.573	12.8	10.5	2.3
C6	9B	1.39	2.265	2.581	13.7	11.0	2.7	2.420	2.614	7.7	7.0	0.7
C6	10B	1.45	2.335	2.610	12.1	8.6	3.5	2.318	2.605	12.0	9.8	2.2

Table 6. Porosity results. Dean Stark and retort as-received bulk density (AR  $\rho_{\text{bulk}}$ ), dry grain density (Dry  $\rho_{\text{bulk}}$ ) and calculated porosities ( $\phi_t$ ,  $\phi_{\text{HC}}$ , and  $\phi_w$ ) listed with corresponding measured maturities (%Ro), when available, from the 30 samples representing 6 unconventional shale reservoir cores (C1-C6).

results for retort versus Dean Stark extractions (Fig. 10), significant scatter in results is apparent on average, though, retort extractions yield somewhat lower values than Dean Stark porosities, with most of the data appearing to the right of a 1:1 reference line. This trend suggests a missing component of total porosity from thermal extraction, an additional variable included in the total porosity measurement from solvent extraction, or a combination of both of these factors.

Total porosity is the sum of the hydrocarbon porosity and the water porosity. It is observed that hydrocarbon porosities differ by 0-4.9 PU and water porosities by 0.1-2.4 PU. These differences are economically significant, given that the highest estimated water porosity in all 60 samples is only 4.1 PU. Understanding the differences in these measurements will be addressed in the Results portion of this paper.

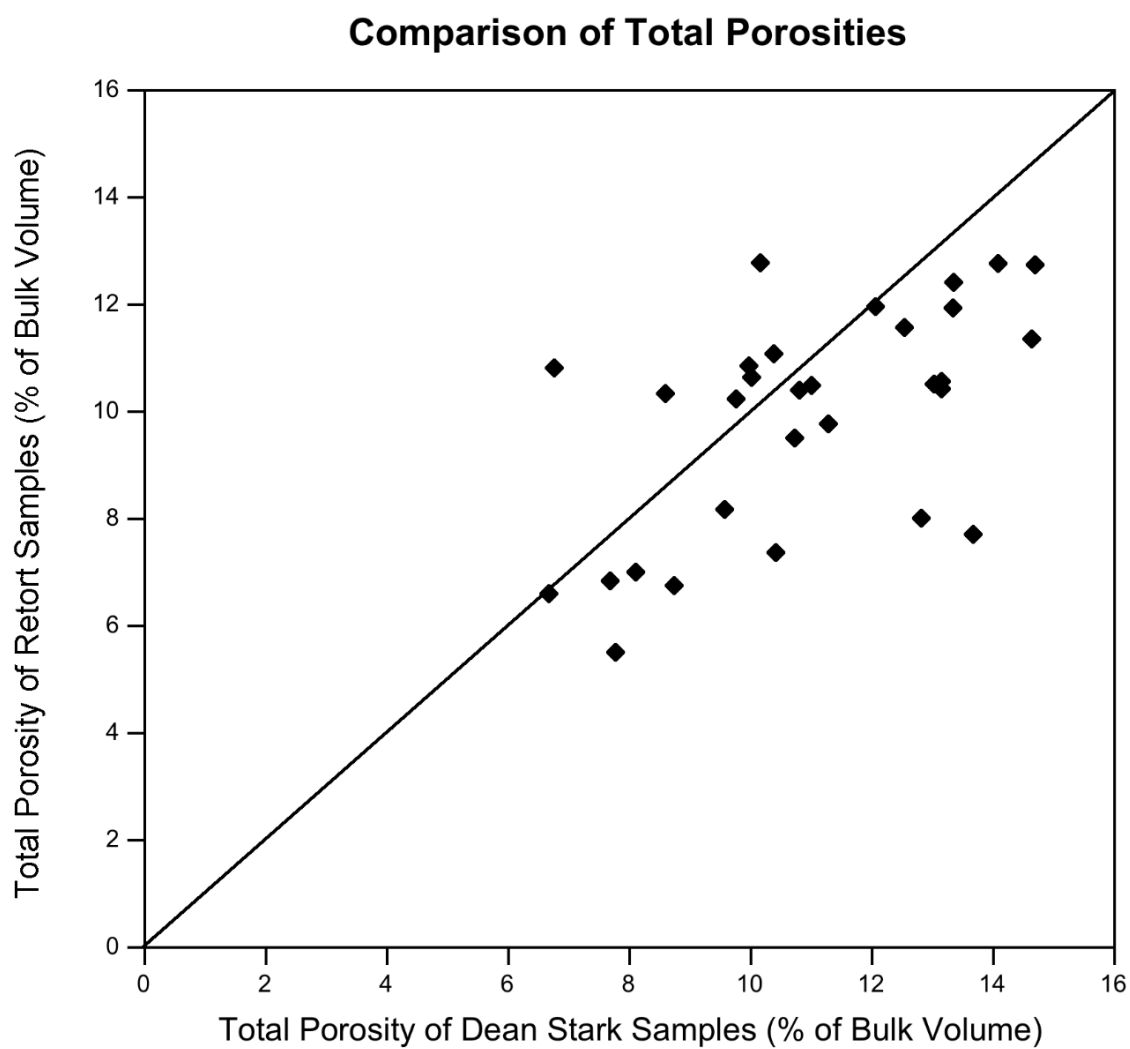


Figure 10. Comparison of total porosities. Chart comparing total porosity (% of bulk volume) from retort and Dean Stark extraction data for samples collected at comparable core depths. A reference one-to-one relationship is shown representing agreement between the two extraction methods.

#### *4.2 Organic matter composition and potential*

Pyrolysis and LECO TOC measurements were performed both before and after extraction. The data resulting from pyrolysis include measurements for S1, S2, S3,  $T_{\max}$ , HI, and OI. A calculated maturity (%Ro) using formula (6) and the measured  $T_{\max}$  have been included for comparison with measured %Ro.

The results are displayed in Tables 7 - 9. Table 7 present the as-received (pre-extraction) results, Table 8 presents the post-Dean Stark measurements, and Table 9 presents the post-retort measurements.

In all 3 datasets, measured %Ro differ considerably from the calculated %Ro. Both the measured and calculated maturities will be compared with mobility in order to explore possible relationships with hydrocarbon mobility.

An ideal extraction technique and pyrolysis evaluation would expect a value of 0 mg HC/g rock for S1, the free hydrocarbons in the evaluated sample. However, actual measurements show a significant decrease in S1 compared with the as-received group, but not a true 0 mg HC/g reading. Dean Stark S1 values are less than retort S1 values, implying either that solvent extraction is more efficient at extracting free hydrocarbons than thermal extraction or that thermal extraction creates new free hydrocarbons during the extraction process.

By definition, S2 values, or the hydrocarbon potential in mg HC/g rock, were expected to maintain the as-received value for all 3 sampling groups (as-received, post Dean Stark, and post-retort). However, a relatively significant drop was recorded by the

post-Dean Stark S2 from original values. This observation is consistent with the observations made by Collins and Lapierre (2014) and Burger et al. (2014).

The HI and OI values from the as-received data have been plotted on a pseudo-van Krevelen plot (Fig. 11) in order to determine kerogen type. From the plot, kerogen type for these samples has been determined to be Type II – Type III. Thus, the kerogen found in the samples tested is expected to be both oil and gas prone.

#### *4.3 Composition and imaging*

28 samples from comparable depths underwent XRD measurements, and 11 samples from the sampling depths were subjected to vitrinite reflectance measurements. These samples from the 11 core depths with complete data were selected for imaging and mobility analyses. Core samples were obtained from these depths and imaging was done at multiple (20X – 30,000X magnification) scales of observation.

As Received Pyrolysis and LECO TOC Results

Core	Sample	Measured %R <sub>m</sub>	LECO TOC (wt %)	S1 (mg HC/g rock)	S2 (mg HC/g rock)	S3 (mg CO <sub>2</sub> /g rock)	T <sub>max</sub> (°C)	HI (mg HC/g TOC)	OI (mg CO <sub>2</sub> /g TOC)	Calculated %R <sub>m</sub>
C1	1B	1.25	5.71	5.11	3.85	0.41	480	67.0	7.0	1.48
C1	2B	1.27	6.43	5.64	4.15	0.51	480	65.0	8.0	1.48
C1	3B	1.23	5.11	5.68	4.51	0.28	482	88.0	5.0	1.52
C1	4B	1.19	5.75	4.80	3.67	0.56	481	64.0	10.0	1.50
C1	5B	1.17	4.69	4.02	2.66	0.29	472	57.0	6.0	1.34
C2	21B	-	1.96	7.85	1.53	0.49	475	78.1	25.0	1.39
C2	22B	-	5.67	23.89	3.96	0.68	478	69.8	12.0	1.44
C2	23B	-	5.06	21.98	3.57	0.56	477	70.6	11.1	1.43
C2	24B	-	7.43	25.65	6.19	0.66	475	83.3	8.9	1.39
C2	25B	-	3.22	13.27	2.89	0.48	474	89.8	14.9	1.37
C3	11B	-	5.89	5.09	2.89	0.41	482	49.1	7.0	1.52
C3	12B	-	3.22	2.97	0.92	0.39	470	28.6	12.1	1.30
C3	13B	-	4.65	4.23	2.10	0.35	475	45.2	7.5	1.39
C3	14B	-	3.73	2.79	1.55	0.26	474	41.6	7.0	1.37
C3	15B	-	7.51	10.40	3.73	0.47	482	49.7	6.3	1.52
C4	26B	-	5.56	9.35	8.95	0.63	447	161.0	11.3	0.89
C4	27B	-	4.71	6.79	6.10	0.78	450	129.5	16.6	0.94
C4	28B	0.935	4.95	8.64	7.45	0.58	446	150.5	11.7	0.87
C4	29B	-	5.19	9.11	7.38	0.53	449	142.2	10.2	0.92
C4	30B	0.98	5.33	7.22	7.07	0.63	456	132.6	11.8	1.05
C5	16B	-	6.06	7.27	4.19	0.47	471	69.0	8.0	1.32
C5	17B	-	3.61	5.99	2.12	0.44	467	59.0	12.0	1.25
C5	18B	1.05	3.85	5.43	2.32	0.38	470	60.0	10.0	1.30
C5	19B	-	4.02	3.79	2.56	0.29	470	64.0	7.0	1.30
C5	20B	-	4.50	5.89	3.66	0.42	471	81.0	9.0	1.32
C6	6B	1.41	6.10	0.97	1.81	0.47	473	30.0	8.0	1.35
C6	7B	-	5.35	0.84	1.36	0.05	477	25.0	1.0	1.43
C6	8B	-	4.55	0.82	1.38	0.24	466	30.0	5.0	1.23
C6	9B	1.39	6.01	0.83	1.80	0.63	470	30.0	10.0	1.30
C6	10B	1.45	4.15	0.93	1.17	0.85	463	28.0	20.0	1.17

Table 7. As-received pyrolysis and LECO TOC results. Table includes S1, S2, S3, T<sub>max</sub>, HI, and OI, with measured and calculated maturity (%Ro) from the 30 samples representing 6 unconventional shale reservoir cores (C1-C6).



Dean Stark Pyrolysis and LECO TOC Results

Core Sample		Measured LECO TOC		S1	S2	S3	T <sub>max</sub>	HI	OI	Calculated
		%R <sub>o</sub>	(wt %)	(mg HC/g rock)	(mg HC/g rock)	(mg CO <sub>2</sub> /g rock)	(°C)	(mg HC/g TOC)	(mg CO <sub>2</sub> /g TOC)	%R <sub>o</sub>
C1	1B	1.25	5.51	0.82	2.78	0.23	471	50.5	4.2	1.32
C1	2B	1.27	6.21	1.41	2.93	0.29	471	47.2	4.7	1.32
C1	3B	1.23	4.65	1.35	2.23	0.30	469	48.0	6.5	1.28
C1	4B	1.19	2.66	0.80	1.17	0.23	464	44.0	8.6	1.19
C1	5B	1.17	3.69	0.51	1.34	0.24	462	36.3	6.5	1.16
C2	21B	-	4.30	0.49	1.82	0.27	464	42.3	6.3	1.19
C2	22B	-	3.58	0.60	1.41	0.36	461	39.4	10.1	1.14
C2	23B	-	3.80	0.53	1.56	0.34	461	41.1	8.9	1.14
C2	24B	-	5.14	0.45	1.85	0.30	460	36.0	5.8	1.12
C2	25B	-	3.35	0.39	1.43	0.26	461	42.7	7.8	1.14
C3	11B	-	5.54	1.12	1.74	0.26	463	31.4	4.7	1.17
C3	12B	-	4.78	1.05	1.40	0.24	465	29.3	5.0	1.21
C3	13B	-	2.69	1.17	0.70	0.20	455	26.0	7.4	1.03
C3	14B	-	4.81	3.24	1.72	0.27	464	35.8	5.6	1.19
C3	15B	-	7.19	1.51	2.31	0.27	465	32.1	3.8	1.21
C4	26B	-	4.67	0.83	3.52	0.32	453	75.4	6.9	0.99
C4	27B	-	4.52	0.39	3.21	0.35	455	71.0	7.7	1.03
C4	28B	0.935	4.70	0.47	3.31	0.33	457	70.4	7.0	1.07
C4	29B	-	3.93	0.43	2.43	0.29	454	61.8	7.4	1.01
C4	30B	0.98	4.43	0.27	2.93	0.32	458	66.1	7.2	1.08
C5	16B	-	3.64	2.95	2.66	0.31	466	73.1	8.5	1.23
C5	17B	-	3.33	0.76	2.13	0.26	465	64.0	7.8	1.21
C5	18B	1.05	2.13	0.40	0.87	0.23	459	40.8	10.8	1.10
C5	19B	-	4.10	0.80	2.07	0.27	463	50.5	6.6	1.17
C5	20B	-	4.26	1.58	2.65	0.30	463	62.2	7.0	1.17
C6	6B	1.41	5.88	1.58	1.83	0.32	469	31.1	5.4	1.28
C6	7B	-	5.08	1.99	1.71	0.33	468	33.7	6.5	1.26
C6	8B	-	5.47	2.13	1.79	0.31	469	32.7	5.7	1.28
C6	9B	1.39	5.55	2.23	2.05	0.35	462	36.9	6.3	1.16
C6	10B	1.45	4.55	1.72	1.44	0.30	466	31.6	6.6	1.23

Table 8. Post-Dean Stark pyrolysis and LECO TOC results. Table includes S1, S2, S3, T<sub>max</sub>, HI, and OI, with measured and calculated maturity (%Ro) from the 30 samples representing 6 unconventional shale reservoir cores (C1-C6).

## Retort Pyrolysis and LECO TOC Results

Core	Sample	Measured LECO TOC		S1 (mg HC/g rock)	S2 (mg HC/g rock)	S3 (mg CO <sub>2</sub> /g rock)	T <sub>max</sub> (°C)	HI (mg HC/g TOC)	OI (mg CO <sub>2</sub> /g TOC)	Calculated %R <sub>o</sub>
		%R <sub>o</sub>	(wt %)							
C1	1B	1.25	6.45	1.33	4.50	0.19	480	69.7	2.9	1.48
C1	2B	1.27	6.54	1.55	4.77	0.18	478	72.9	2.8	1.44
C1	3B	1.23	4.34	1.10	3.29	0.22	481	75.9	5.1	1.50
C1	4B	1.19	5.72	1.35	4.00	0.30	478	69.9	5.2	1.44
C1	5B	1.17	3.87	0.57	2.09	0.21	478	54.0	5.4	1.44
C2	21B	-	5.57	1.40	3.85	0.15	480	69.2	2.7	1.48
C2	22B	-	3.34	0.94	2.24	0.15	482	67.0	4.5	1.52
C2	23B	-	4.89	1.42	3.27	0.16	482	66.8	3.3	1.52
C2	24B	-	6.72	1.32	3.69	0.21	479	54.9	3.1	1.46
C2	25B	-	4.89	1.60	3.77	0.23	477	77.1	4.7	1.43
C3	11B	-	5.83	1.49	2.78	0.21	477	47.7	3.6	1.43
C3	12B	-	4.87	1.20	2.43	0.19	481	49.9	3.9	1.50
C3	13B	-	5.14	1.18	2.15	0.22	474	41.8	4.3	1.37
C3	14B	-	5.84	1.13	2.39	0.18	476	40.9	3.1	1.41
C3	15B	-	7.72	1.90	3.19	0.22	480	41.3	2.8	1.48
C4	26B	-	5.57	3.49	10.22	0.19	444	183.4	3.4	0.83
C4	27B	-	7.05	3.92	12.07	0.21	444	171.3	3.0	0.83
C4	28B	0.935	4.23	3.22	7.13	0.14	444	168.5	3.3	0.83
C4	29B	-	5.55	3.37	9.62	0.29	445	173.3	5.2	0.85
C4	30B	0.98	5.46	2.83	9.33	0.30	444	171.0	5.5	0.83
C5	16B	-	3.24	1.36	3.88	0.22	458	119.6	6.8	1.08
C5	17B	-	2.77	1.14	2.70	0.29	429	97.6	10.5	0.56
C5	18B	1.05	4.05	1.19	3.69	0.17	465	91.0	4.2	1.21
C5	19B	-	3.68	1.16	3.04	0.22	467	82.5	6.0	1.25
C5	20B	-	4.63	1.23	3.87	0.24	467	83.6	5.2	1.25
C6	6B	1.41	6.53	1.42	3.06	0.23	483	46.9	3.5	1.53
C6	7B	-	4.41	1.32	2.29	0.18	475	52.0	4.1	1.39
C6	8B	-	5.84	1.54	2.83	0.15	479	48.5	2.6	1.46
C6	9B	1.39	3.30	0.86	1.52	0.23	477	46.1	7.0	1.43
C6	10B	1.45	4.52	0.89	1.73	0.17	476	38.2	3.8	1.41

Table 9. Post-retort pyrolysis and LECO TOC results. Table includes S1, S2, S3, T<sub>max</sub>, HI, and OI, with measured and calculated maturity (%R<sub>o</sub>) from the 30 samples representing 6 unconventional shale reservoir cores (C1-C6).

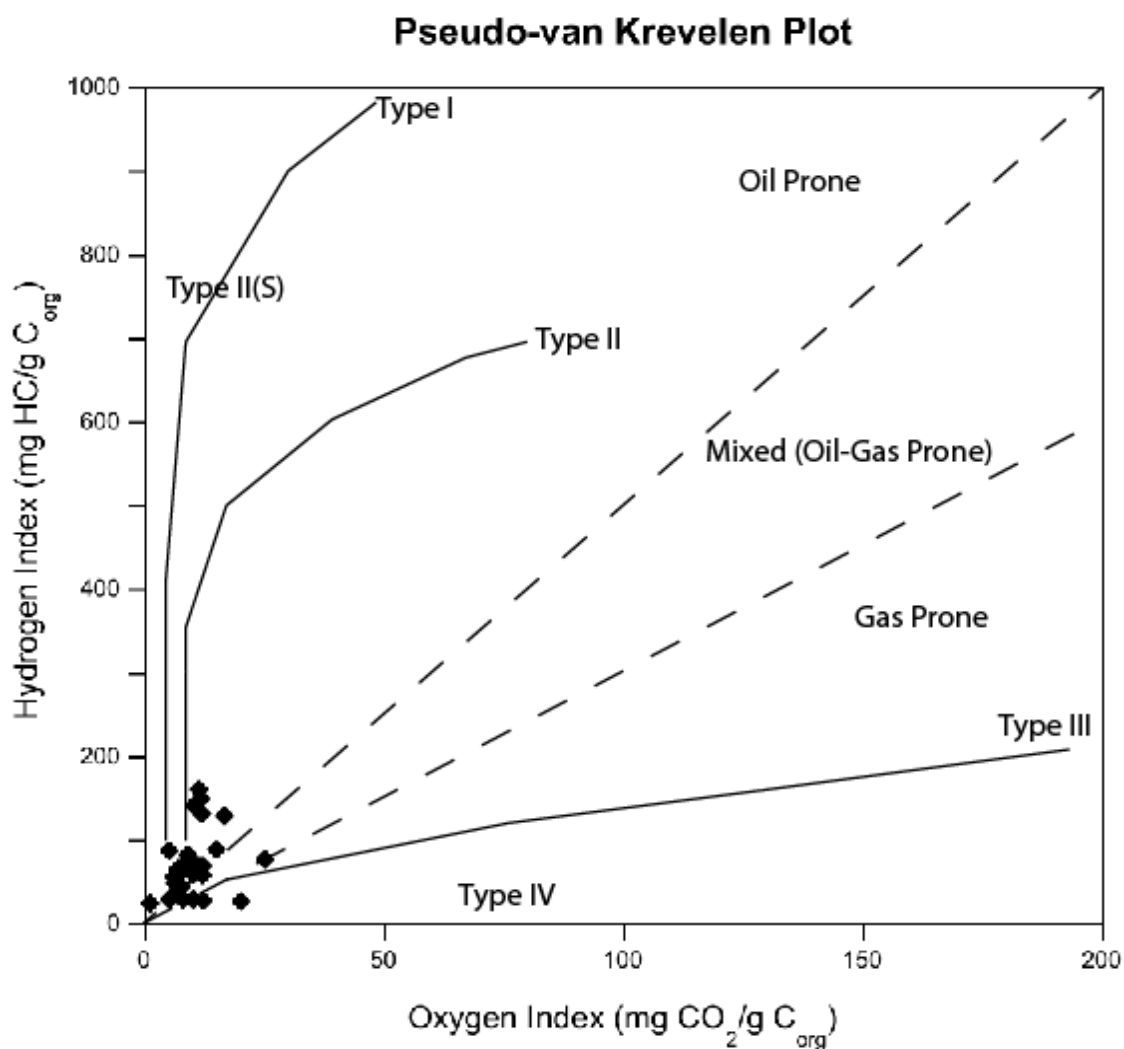


Figure 11. Pseudo-van Krevelen plot. Plot of oxygen index (mg CO<sub>2</sub> / g C<sub>org</sub>) against hydrogen index (mg HC / g C<sub>org</sub>) used to estimate the type of kerogen. The data plot primarily between Type II and Type III indicating oil prone, oil-gas prone, and gas prone kerogen.

#### *4.3.1 X-ray powder diffraction*

The XRD data was provided in both weight percent and volume percent equivalences. Table 10 displays quantities of calcite, clay, quartz, and pyrite, by weight and volume. TOC is given only as volume percent. Accessory phases in addition to the above represent less than 10% of the sample, by volume.

Calcite is the primary component of all but 1 of the 30 samples. Clay and quartz are significant matrix contributing components. The TOC measured by XRD ranges from 4.4–16.1 volume percent, making these organically rich rocks.

XRD measurements have undergone a Reitveld refinement, and are therefore considered to be reliable measurements of the rock composition within. The XRD data was used to interpret BSE images and check that phases identified by density have volume fractions of the order of XRD determinations.

## X-Ray Powder Diffraction Results

Core	Sample	Weight Percent					Volume Percent				
		Calcite	Clay	TOC	Pyrite	Quartz	Calcite	Clay	TOC	Pyrite	Quartz
C1	1B	54.6	19.1	-	3.8	18.9	48.3	17.2	12.4	1.8	17.1
C1	2B	46.1	24.1	-	4.6	20.3	40.3	21.3	13.9	2.2	18.2
C1	3B	53.7	18.1	-	4.1	20.0	48.3	16.6	11.2	2.0	18.4
C1	4B	50.3	22.9	-	4.5	18.4	44.6	20.5	12.5	2.1	16.7
C1	5B	52.4	19.9	-	3.5	21.9	47.3	18.2	10.2	1.7	20.3
C2	21B	80.8	6.3	-	0.7	10.8	77.2	6.2	4.4	0.4	10.5
C2	22B	58.1	14.2	-	3.0	22.7	51.2	12.8	12.2	1.4	20.4
C2	23B	58.7	17.9	-	2.7	19.0	52.5	16.3	11.0	1.3	17.3
C2	24B	47.5	24.6	-	5.4	20.0	40.7	21.5	15.9	2.5	17.5
C2	25B	69.3	12.7	-	1.6	14.4	64.3	12.2	7.1	0.8	13.7
C3	11B	48.9	21.9	-	4.9	20.6	43.3	19.7	12.8	2.3	18.7
C3	12B	55.6	18.1	-	4.4	18.8	52.2	17.3	7.2	2.2	18.1
C3	13B	11.1	37.4	-	9.1	36.1	10.2	34.9	10.3	4.5	34.0
C3	14B	63.7	15.9	-	5.6	11.8	59.6	15.0	8.3	2.8	11.3
C3	15B	57.3	20.8	-	5.9	13.9	49.0	18.1	16.1	2.7	12.2
C4	26B	53.1	21.0	-	3.2	19.8	47.0	19.0	12.0	1.5	17.9
C4	27B	57.0	18.9	-	3.5	15.9	51.6	17.5	10.3	1.7	14.7
C4	28B	53.5	19.0	-	3.0	20.4	47.9	17.3	10.8	1.4	18.7
C4	29B	47.4	18.7	-	2.9	27.4	42.2	17.0	11.2	1.4	24.9
C4	30B	50.5	18.7	-	3.3	24.5	44.9	17.0	11.5	1.6	22.3
C5	16B	54.0	15.0	-	2.0	24.0	45.5	13.6	-	1.0	21.8
C5	17B	53.0	12.0	-	2.0	27.0	48.6	10.9	-	1.0	24.6
C5	18B	65.0	14.0	-	3.0	14.0	47.7	12.7	-	1.4	12.7
C5	19B	-	-	-	-	-	-	-	-	-	-
C5	20B	-	-	-	-	-	-	-	-	-	-
C6	6B	55.6	16.4	-	4.2	15.1	49.3	14.8	13.3	2.0	13.7
C6	7B	60.2	12.9	-	5.6	11.7	54.4	11.9	11.8	2.7	10.9
C6	8B	66.2	11.5	-	2.9	14.2	60.2	10.5	10.0	1.4	13.2
C6	9B	59.2	9.4	-	5.1	20.0	52.6	8.3	13.1	2.4	18.1
C6	10B	50.0	17.2	-	7.7	15.5	47.0	16.1	9.4	3.9	14.9

Table 10. X-ray powder diffraction results. Table displays results from the 30 samples representing 6 unconventional shale reservoir cores. Both weight and volume percentages are provided for calcite, all clay, pyrite, and quartz. Only volume percent of total organic content is provided.

#### 4.3.2 Microscopic X-ray fluorescence

In order to determine the locations desired for 1 – 10  $\mu\text{m}$  resolution imaging, a better understanding of the bedding patterns in the samples was required. To obtain this information, MicroXRF was performed on whole samples taken from cores (Fig. 12).

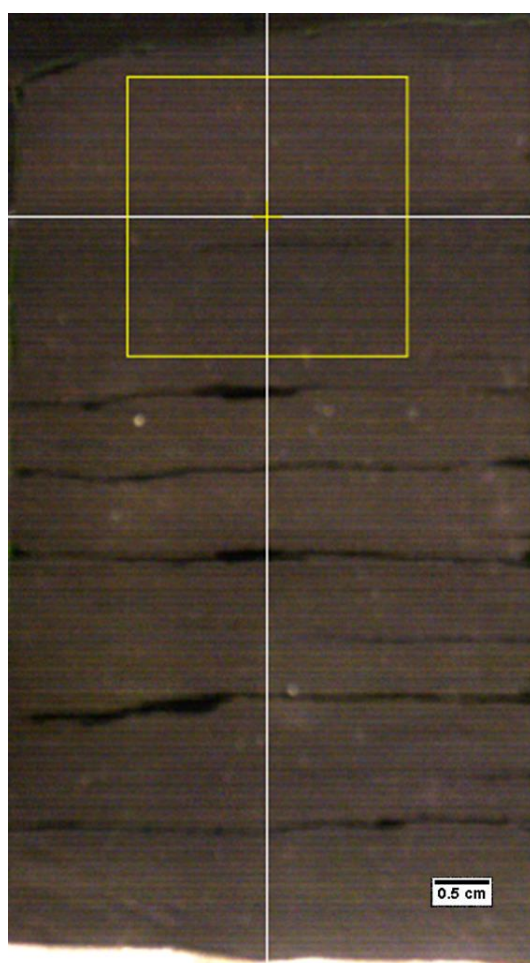


Figure 12. Microscopic X-ray fluorescence core sample. Sample 6B with location of MicroXRF outlined in yellow. The analyzed region measures 2.56 cm x 2.56 cm.

Aluminum (Al), barium (Ba), calcium (Ca), iron (Fe), phosphorus (P), sulfur (S), silicon (Si), and titanium (Ti) were individually detected (Fig. 13) by the MicroXRF and processed using ImageJ Software.

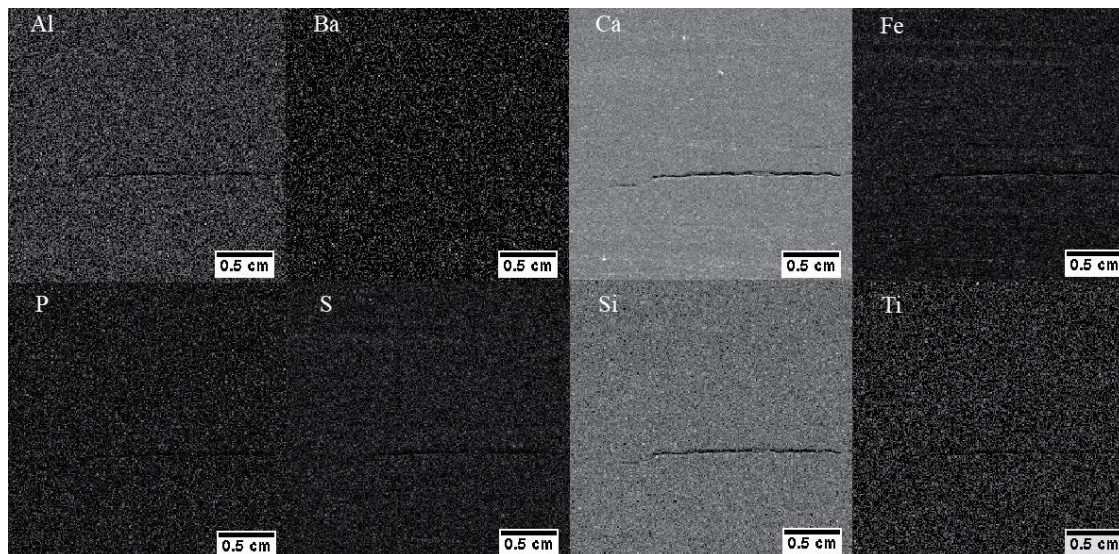


Figure 13. Microscopic x-ray fluorescence elemental maps. Elemental maps of sample 6B acquired from the sampling region identified in Figure 12. Aluminum (Al), barium (Ba), calcium (Ca), iron (Fe), phosphorous (P), sulfur (S), silicon (Si), and titanium (Ti) are displayed and were detecting at 100  $\mu$ m resolution.

Al readings are typically high for clays, while Si is strong in quartz. High levels of Ca are expected from comparison with XRD data calcite readings. Fe and S are both indicative of pyrite. P could be indicative of apatite, which is suggestive of a biologic origin. Ti is present and is suggestive of rutile, which is typically found in igneous and

metamorphic rocks and is questionable for unconventional reservoir shales. However, rutile can exist in sedimentary rocks due to its resistance to weathering and more significant concentrations are probably found in coarser-grained rocks. Ba could be symbolic of detrital materials, since its presence is commonly indicative of reworked rocks in serving as the void-filling material. Organic matter is not imaged using MicroXRF due to the low atomic numbers of the minerals found in organic matter (carbon, hydrogen, oxygen, nitrogen) and only trace amounts of sulfur.

Through ImageJ, background noise was subtracted and images were combined in order to provide a visualization of the lamination patterns within the analyzed samples. Samples 18B (1.05 %Ro), 2B (1.27 %Ro) and 6B (1.41 %Ro) are displayed in Figure 14.

Ca, P, Fe, and S have been displayed together in order to identify regions of increased biological deposition (P) and pyrite (Fe,S). Si, Al, and Ca were also displayed together in order to display patterns in bedding associated with calcite (Ca), clays (Al), and quartz (Si). The primary pattern discovered in the samples analyzed is layers of mixed calcite/clay/quartz and randomly distributed calcite-rich layers. Further imaging was done by identifying these 2 distinct layers in polished plates and acquiring images from both regions for all samples.



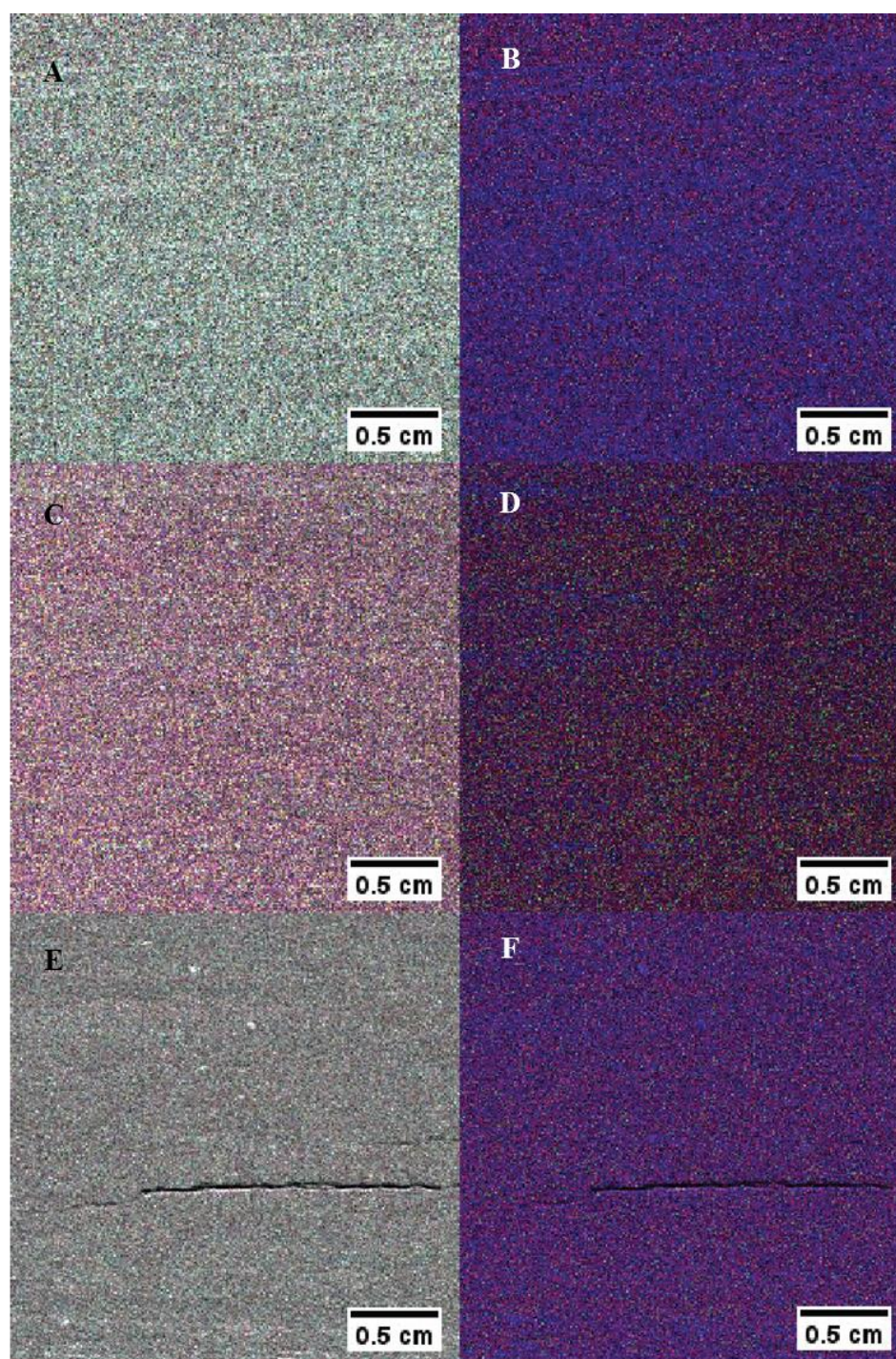


Figure 14. False-color microscopic x-ray fluorescence overlay maps. Maps of sample 18B (A and B), 2B (C and D), 6B (E and F) created from MicroXRF results. A, C, and E show Ca mapped as gray, P as cyan, Fe as magenta, and S in yellow. B, D, and F display Si as red, Al as green, and Ca as blue.

#### *4.3.3 Reflected light microscopy*

Polished plates were made for each sample that had corresponding maturity measurements. The polished plates were made from the regions of the sample material that was analyzed using the MicroXRF. Reflected light microscopy was done using the Zeiss Axioplan 2 Imaging microscope with a Zeiss AxioCam HRc camera on both the mixed calcite/clay/quartz layers and calcite-rich layers of each polished plate. Images of fractures were also collected for further analyses.

Figure 15 shows the resulting images collected at 20X magnification and 50x magnification. Figure 15 displays images from 18B from a calcite-rich layer, while 2B and 6B show mixed calcite/clay/quartz layers. 6B also contains a fracture which appears to have been filled with a light colored material. The shale material is brittle and fractures easily during specimen preparations. Similarly, microstructural analyses reveal natural fractures which are filled and some which are not filled.

Both the mixed layers and calcite-rich layers contain foraminifera (Scholle and Ulmer-Scholle, 2003), with greater numbers of forams in calcite-rich regions. These foram shells consist of calcite with cavities that can be filled by other solids of varying composition and character, partially filled, or appear to be empty, and vary in filling. Throughout the depositional history of these rocks, the foraminifera shells have maintained their original shape, even when they contain no solid phases.

The foraminifera are surrounded by very fine-grained material which was imaged using the SEM in order to better identify its density and character.



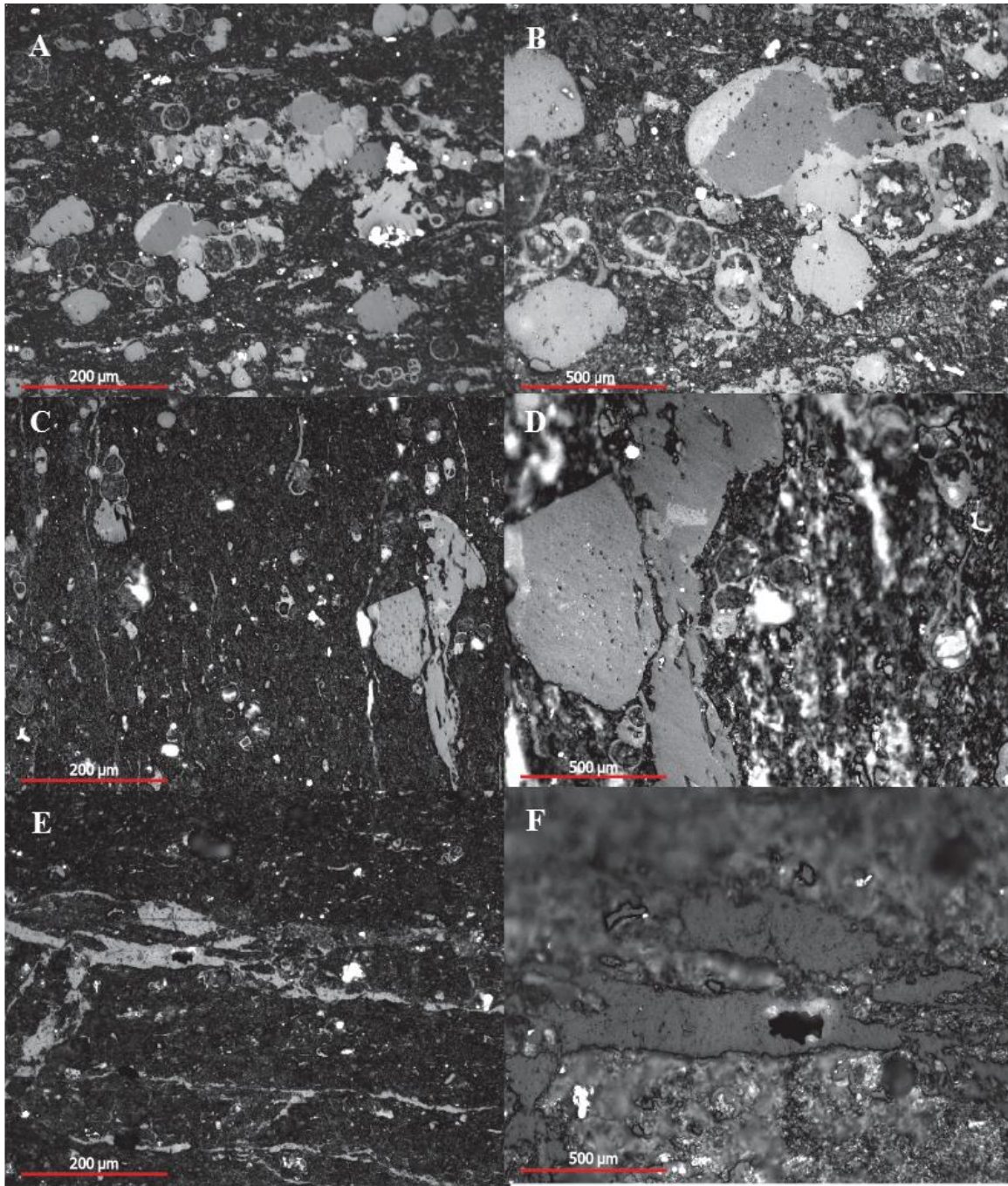


Figure 15. Reflected light microscopy images. Images collected using a Zeiss Axioplan 2 Imaging microscope with a Zeiss AxioCam HRC camera of samples 18B (A and B), 2B (C and D), 6B (E and F). A, C, and E show images captured at 20X magnification. B, D, and F display images acquired using a 50X lens.

#### *4.3.4 Wavelength – dispersive spectroscopy*

WDS was tested as a means of identifying and locating organic solids within the polished plates. Figure 16 displays a BSE image along with corresponding element maps acquired through WDS using a Cameca SX50 electron microprobe for Ca, Si, Al, C, S, and Fe). Ca was most clearly detected by WDS, while S and Fe were primarily detected in the presence of pyrite. C is difficult to detect using WDS, and it is present in both the organic matter and calcite ( $\text{CaCO}_3$ ). Ideally, organic solids could be identified by the coexistence of S and C. However, the counts for C and S were low. C counts are not expected to be large owing to its low Z, and S, which is more readily measure by WDS can be variable in organic solids. Given that S is apparently low in organics of these shales, WDS analysis mapping failed to produce practical results for the distribution of organics.

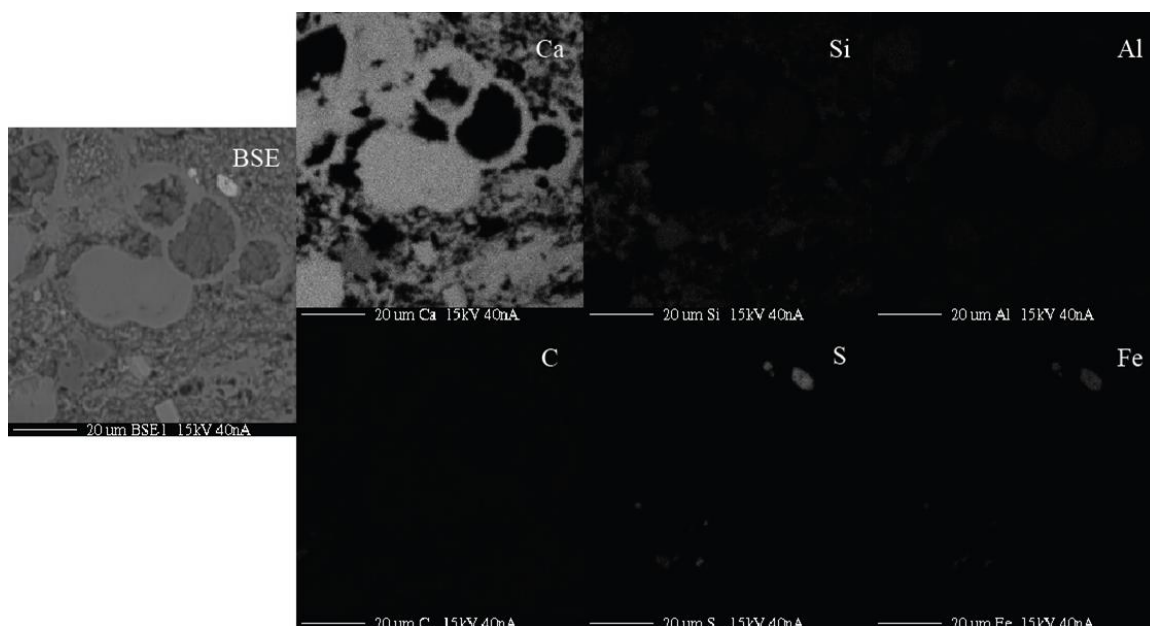


Figure 16. Backscattered electron and wavelength-dispersive spectroscopy spectroscopy images from the electron microprobe. Images collected for sample 28B using a 15 kilovolt, 40 nanoamp beam of a 100  $\mu\text{m}$  X 100  $\mu\text{m}$  area. BSE and WDS images of Al, C, Ca, Fe, S, and Si were collected from the same location and results are displayed above.

#### *4.3.5 Scanning electron microscopy*

Secondary electron (SE) SEM images (at magnifications of 750X – 30,000X) reveal smooth, polished surfaces, but offer very little insight into organic or inorganic pore space (Fig. 17). Backscattered electron (BSE) SEM images provide far better information about microstructures and phase distributions of shale samples (Fig. 18)

BSE images (at 250X, Fig. 18C; 500X, Fig. 18A, 18E; and 7500X, Fig. 18B, 18D, 18F) were taken from approximately the same locations as the reflected light images in Figure 15. All of the images exhibit the presence of matrix materials (primarily calcite, clay, quartz, pyrite, and organic matter) with varying densities. The darkest areas correspond to the lowest sample densities, primarily to fracture and foram filling phases as well as low-density phases distributed within the very fine-grained regions. The brightest areas, such as the framboidal pyrite located in the upper left-hand corner of the 7500X image of 18B, are indicative of the highest density minerals.

The distribution of LUT # is readily available using ImageJ, and can be expressed as a histogram (Fig. 19). These histograms, along with a well-calibrated lookup table (Fig. 20) facilitate the quantification of materials in BSE and will be discussed in more detail in the next section.

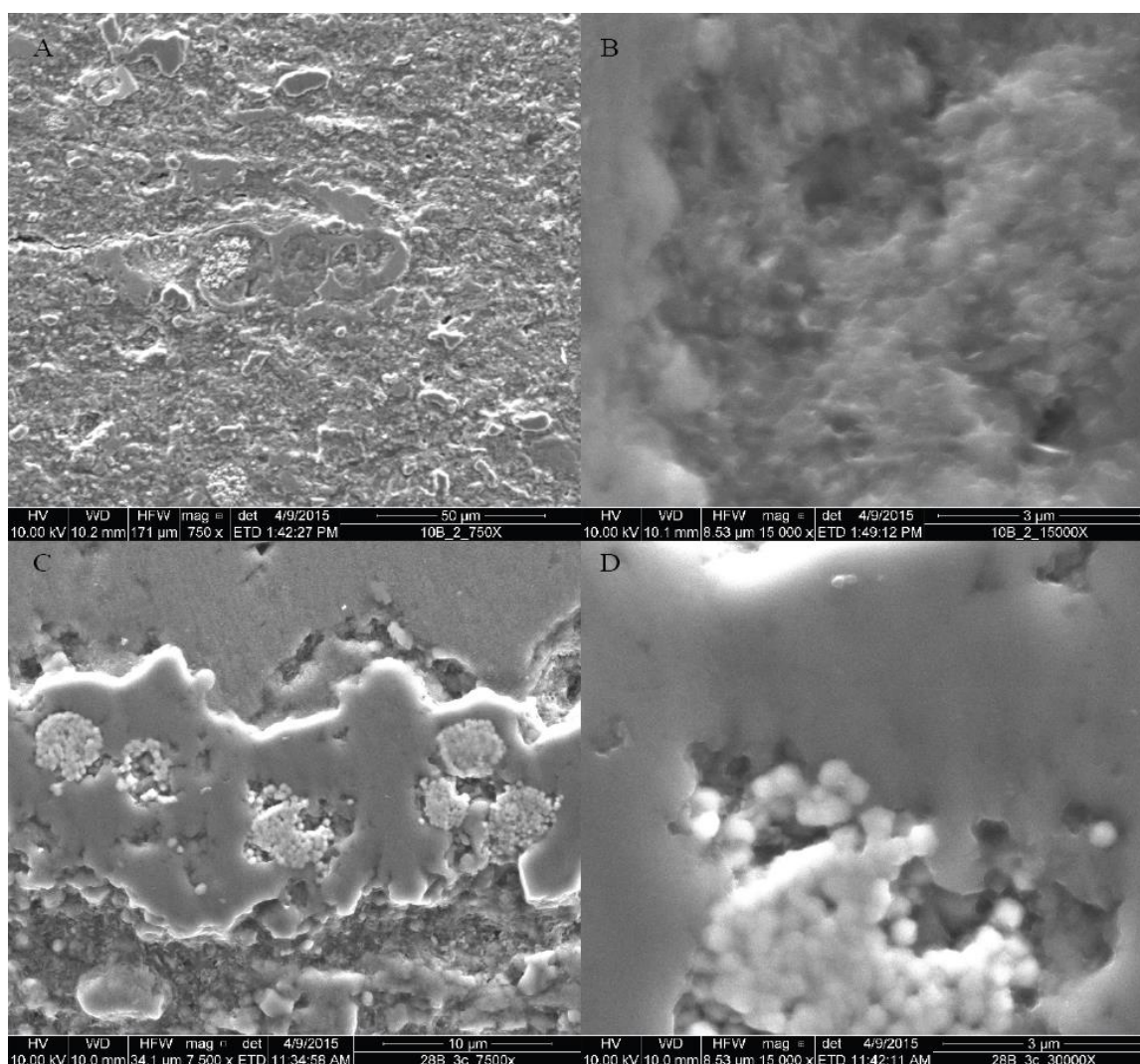


Figure 17. Secondary electron images. Images collected for samples 10B (A and B) and 28B (C and D) using a 10 kV beam and a working distance of 10 mm. A is displayed at 750X with a horizontal field width (HFW) of 171  $\mu\text{m}$ , B is 15,000X with a HFW of 8.53  $\mu\text{m}$ , C is 7,500X with a HFW of 34.1  $\mu\text{m}$  and D is 30,000X magnification with a HFW of 8.53  $\mu\text{m}$ . SE images illustrate the nature of surface roughness, resulting from polishing procedures to produces a relatively smooth surface despite the low Mohs hardness of shale minerals. SE images are ineffective in showing porosity or the shapes of individual mineral grains or solid phases.



Figure 18. Backscattered electron images for samples of varying maturities. Images collected for samples 18B (A and B), 2B (C and D), and 6B (E and F) using a 10 kV beam and a working distance of 10 mm. These samples were chosen for their range in maturity (18B: 1.05 %Ro, 2B: 1.27 %Ro, 6B: 1.41 %Ro). A is displayed at 500X with a HFW of 512  $\mu\text{m}$ , B is 7,500X with a HFW of 34.1  $\mu\text{m}$ , C is 250X with a HFW of 1020  $\mu\text{m}$ , D is 7,500X with a HFW of 34.1  $\mu\text{m}$ , E is 500X with a HFW of 512  $\mu\text{m}$ , and F is 7,500X with a HFW of 34.1  $\mu\text{m}$ . Variance in grayscale indicates variance in solid phase density.



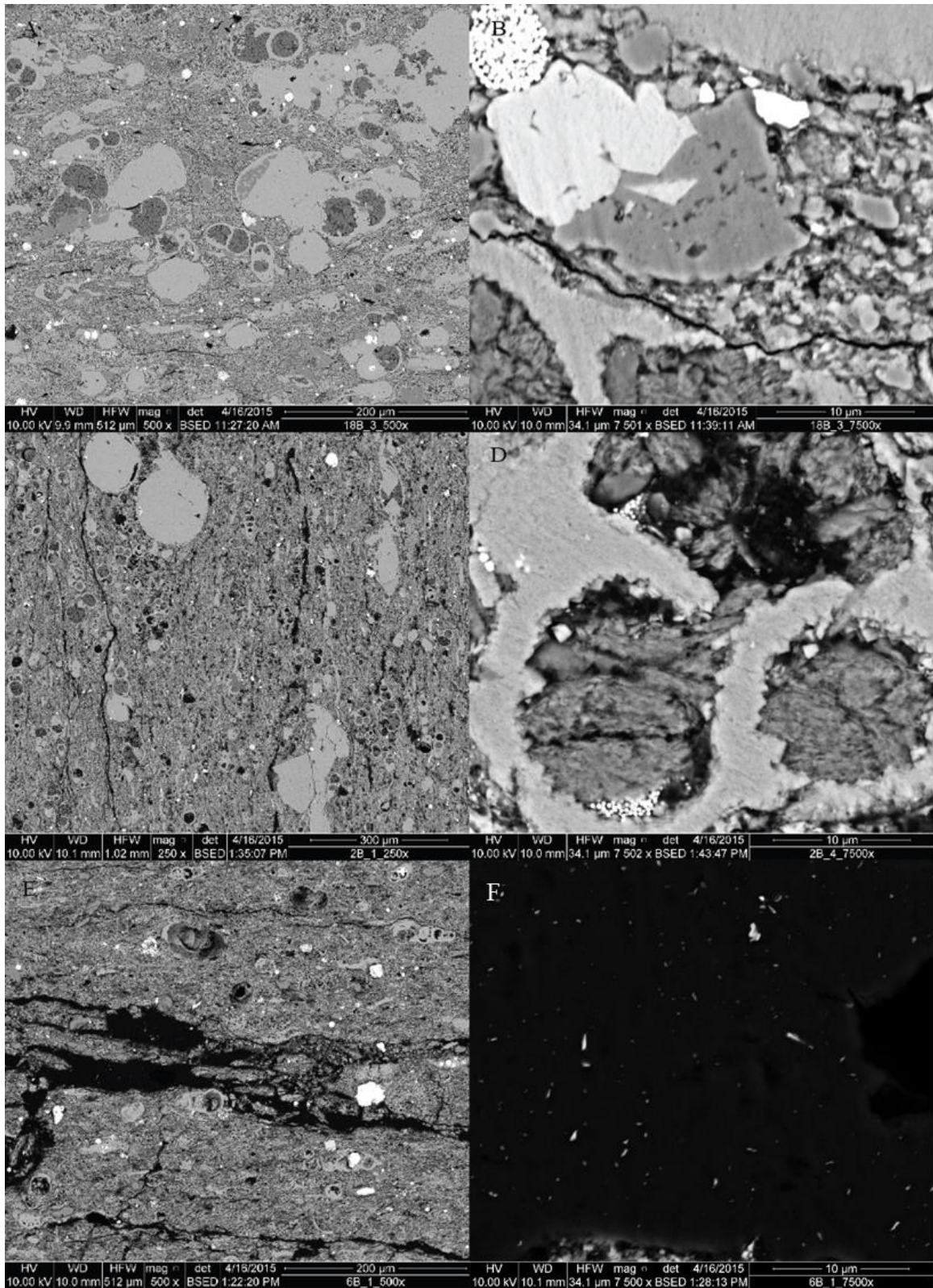
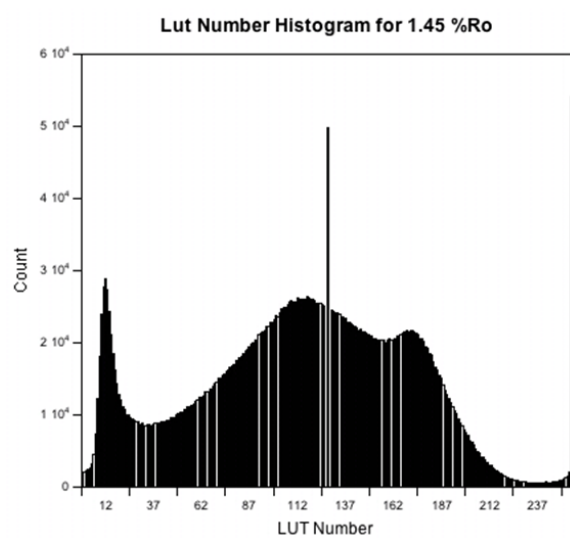
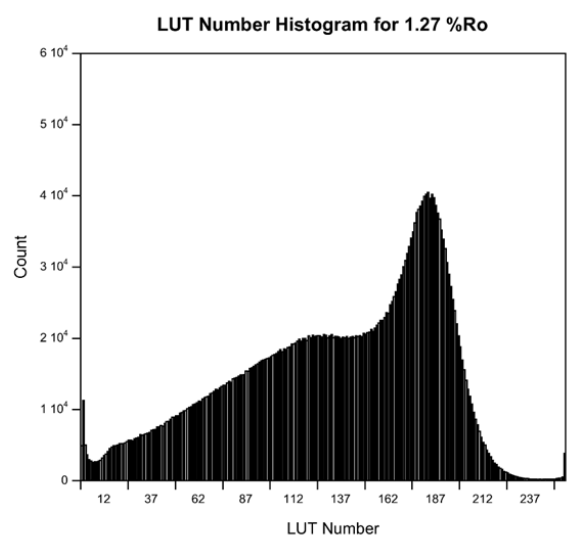
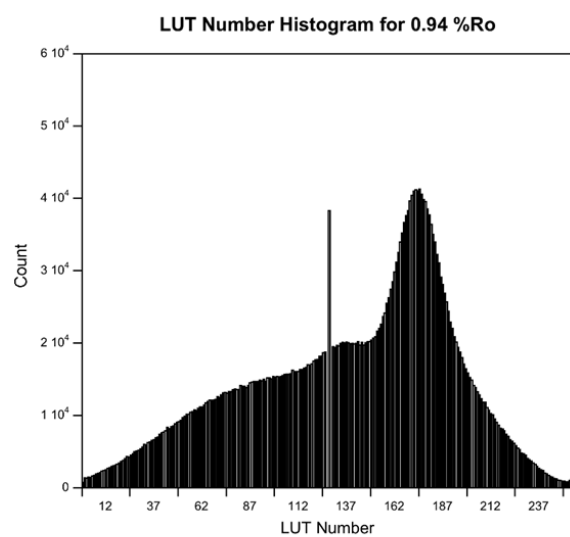


Figure 19. Lookup table histograms of 8-bit backscattered electron images. Histograms of lookup table numbers (0-255) extracted from 8-bit grayscale images produced during BSE imaging. Histograms for 3 different maturities are exhibited (0.94 %Ro, 1.27 %Ro, and 1.45 %Ro).



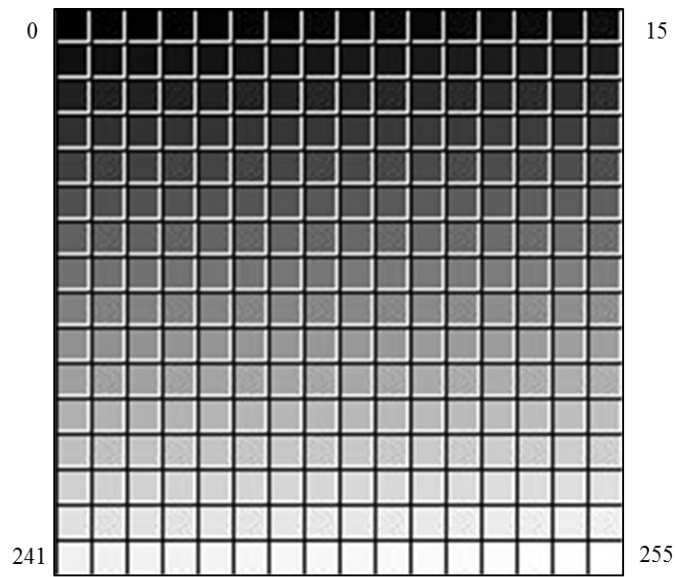


Figure 20. Grayscale 8-bit lookup table. Lookup table applied to 8-bit images using assigned numbers 0 through 255. The darkest solid black is associated with the 0 value, and the brightest white represents 255.

## 5. DISCUSSION

Very recent work has been presented at conferences discussing a solvently-extracted immobile component included in Dean Stark porosity measurements, which supports the findings of this study (Burger et al., 2014; Collins and Lapierre, 2014). In addition to confirming this work, an improved method of quantifying both matrix-contributing kerogen and mobile pore fluids follows.

### 5.1 Porosity analysis

A distinct difference in Dean Stark and retort porosities is observed when plotted separately against as-received bulk density (Fig. 21). Inequality between Dean Stark and retort porosities was determined by two separate statistical analyses. First, each data set was best-fit by a line by least squares, to compare slopes and intercepts independently. Least-squares fitting of Dean Stark data yielded a slope  $m = -31.76 \left( \frac{\% \text{ bulk volume}}{\frac{g}{cm^3}} \right)$  with a standard error of  $0.91 \left( \frac{\% \text{ bulk volume}}{\frac{g}{cm^3}} \right)$  and an intercept  $b = 86.15 (\% \text{ bulk volume})$  with a standard error of  $2.15 (\% \text{ bulk volume})$ . Least-squares fitting of the retort data yielded a slope  $m = -35.89 \left( \frac{\% \text{ bulk volume}}{\frac{g}{cm^3}} \right)$  with a standard error of  $1.47 \left( \frac{\% \text{ bulk volume}}{\frac{g}{cm^3}} \right)$  and an intercept  $b = 94.32 (\% \text{ bulk volume})$  with a standard error of  $3.47 (\% \text{ bulk volume})$ . Dean Stark and retort  $m$  and  $b$  line-fit parameters exhibit no overlap within one standard deviation of the respective best-fit lines, and are thereby considered statistically different. The second statistical evaluation considered the centroids of the Dean Stark

and retort datasets. Variances of individual data from the line fits were determined and applied to dataset centroids for both the Dean Stark and retort measurements and centroid x and y values were subjected to the t-test. Based on this analysis, total porosities estimated from Dean Stark and retort extractions are unequal ( $p=1.64\text{E-}07$ ). Before investigating any differences in hydrocarbon measurements, the water content must be compared in order to best estimate the true water saturation before storage. Dean Stark extraction was completed on samples before retort was performed; some of the cores were stored for several years between extractions. The extended storage time may result in water loss, by evaporation. Although the as-received bulk densities of retorted samples appear to be comparable to samples that underwent Dean Stark (Fig. 22), when water porosities are compared (Fig. 23), an obvious discrepancy appears.

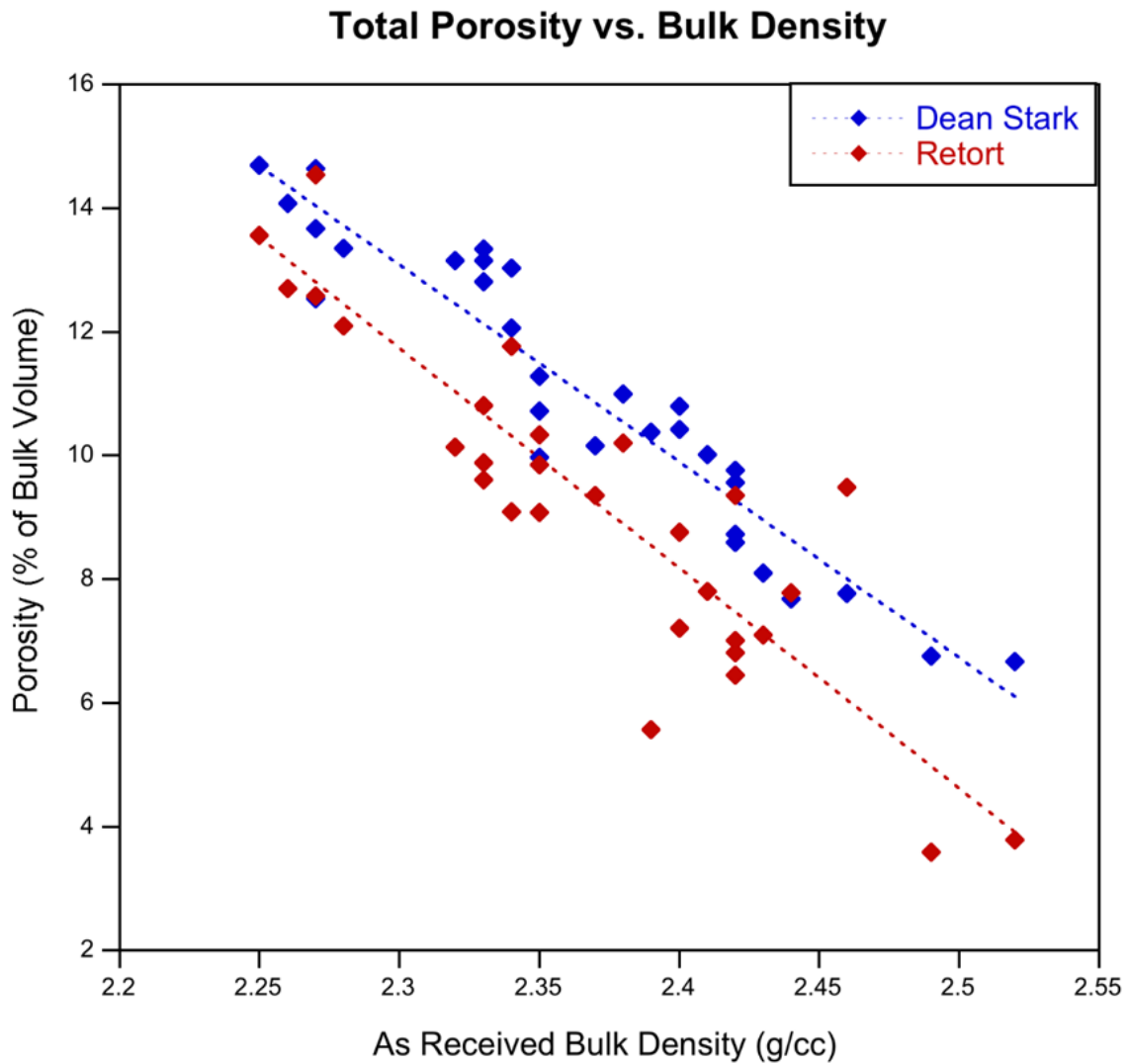


Figure 21. Total porosity vs. bulk density. Chart comparing Dean Stark calculated total porosity, as % of bulk volume, with retort porosity for samples collected at comparable core depths. Both porosities are plotted against as-received bulk densities for comparison. Best-fit lines have been applied in order to facilitate trend observation. Dean Stark measurements exhibit overall higher total porosities than retort determined porosities.

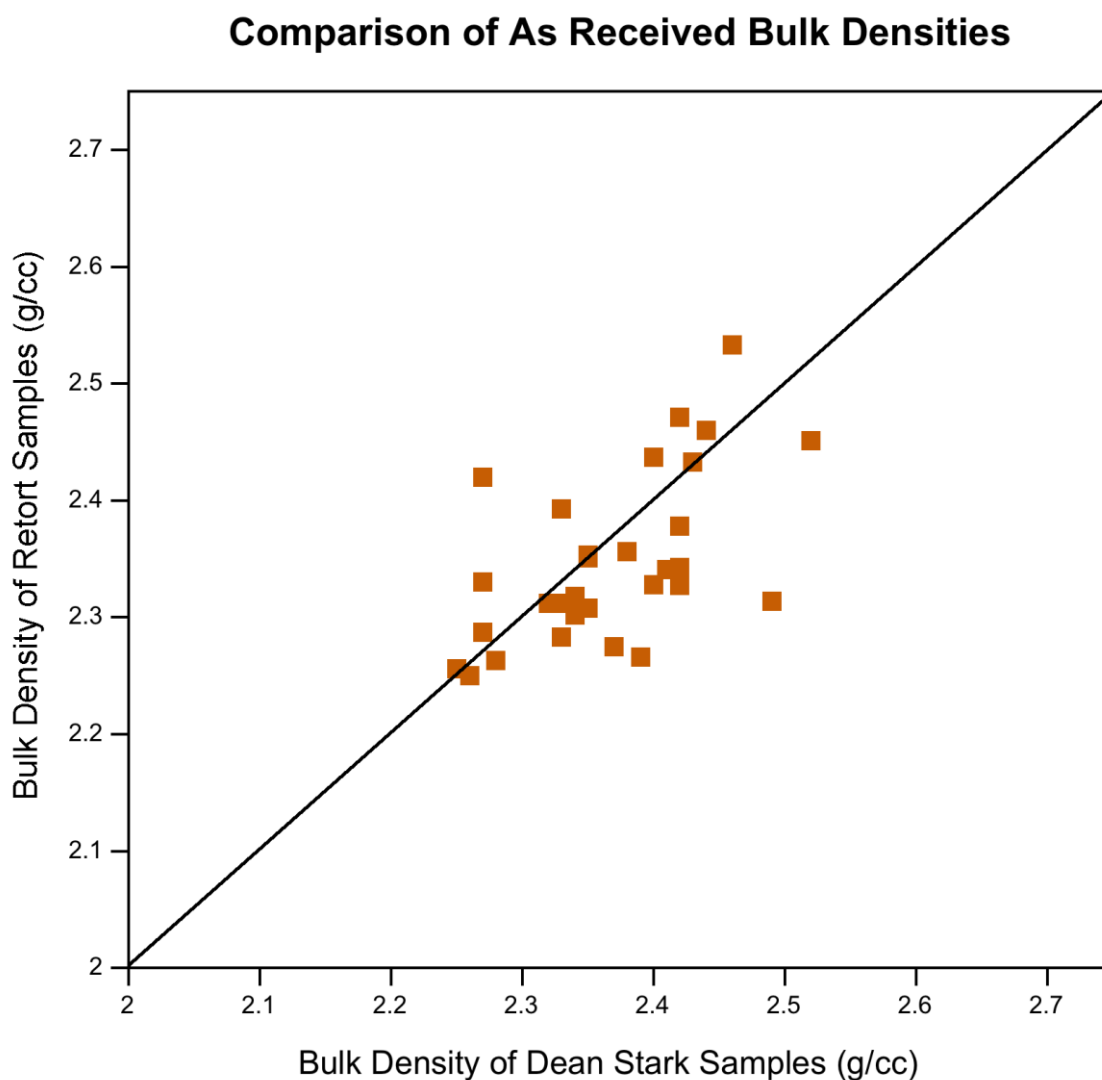


Figure 22. Comparison of as-received bulk densities. Chart comparing as-received (pre-extraction) bulk densities, as g/cc, for the retort samples and Dean Stark samples collected at comparable core depths. The black line is representative of a one-to-one relationship between Dean Stark and retort bulk densities; points plotted nearest to this line exhibit the most similar porosities.



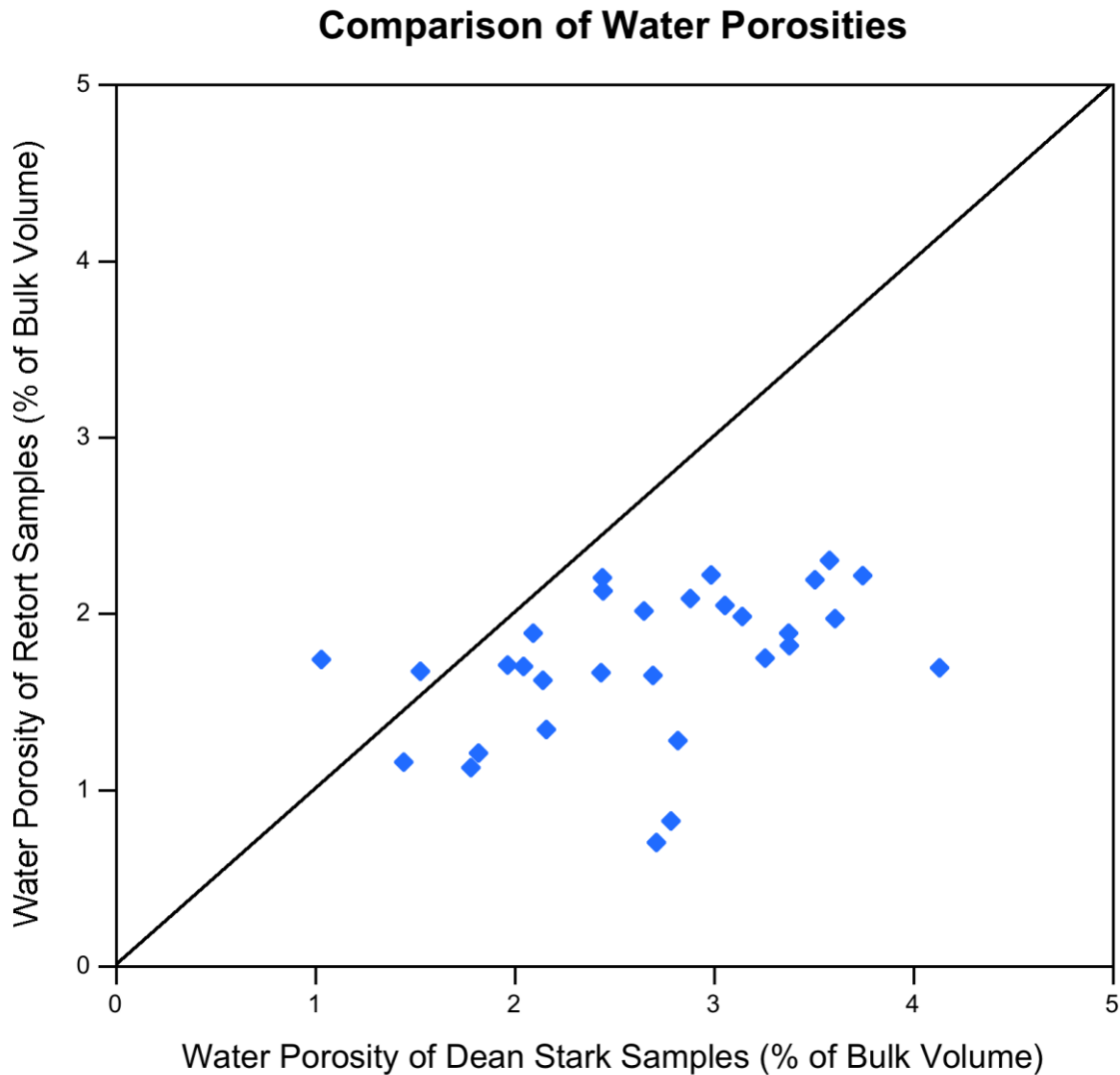


Figure 23. Comparison of water porosities. Chart comparing Dean Stark calculated water porosity, as % of bulk volume, against retort water porosity for samples collected at comparable core depths. The black line is representative of a one-to-one relationship between Dean Stark and retort porosities; points plotted nearest to this line demonstrate the most similar water porosities, based on water saturation ( $S_w$ ). Dean Stark samples exhibit overall higher water porosities than those determined by retort of samples.

The water porosities are significantly higher in the Dean Stark analyzed samples compared to the retorted samples, confirming water loss during storage. Analyses of the effects of core storage time on water saturation yielded complicated relationships possibly resulting from storage at variable humidity conditions and evaporative losses of core water. Fluid substitution based on Gassman's relationships (Equation 8) and the Dean Stark water saturations has been applied to the retort calculations in order to compensate for lost water during storage (Avseth, Mukerji, and Mavko 2005).

$$\varphi_t = \frac{\rho_{grain} - \rho_{bulk}}{\rho_{grain} - \rho_{fluid\_sub}} \quad (8)$$

Where  $\varphi_t$  is the total porosity,  $\rho_{grain}$  is the dry grain density,  $\rho_{bulk}$  is the as-received bulk density, and  $\rho_{fluid\_sub}$  is the fluid density of the retort as-received samples calculated with Dean Stark as-received water saturation ( $S_{w\_DS}$ ) and retort as-received hydrocarbon saturation ( $S_{HC}$ ) (Equation 9).

$$\rho_{fluid\_sub} = S_{w\_DS} * 1 \frac{g}{cm^3} + S_{HC} * 0.83 \frac{g}{cm^3} \quad (9)$$

Despite this attempt to reconcile porosities, total porosities, corrected for differing fluid substitutions, continue to show differences between the Dean Stark and retort results (Fig. 24). Dean Stark porosities remain greater than corrected retort porosities. Moreover, hydrocarbon porosities determined by Dean Stark methods are lower than determined from retort samples for the lower hydrocarbon porosities (< 8 % BV) while Dean Stark porosities are greater than determined from retort samples for higher hydrocarbon porosities (> 8% BV) (Fig. 25).

In order to better understand the SE measurements, I have analyzed S1 and S2 peaks following Dean Stark and retort extractions. Figures 26 and 27 show post-Dean Stark and post-retort S1 values, respectively, against as-received S1 values. As expected, S1 values are highest in the as-received samples, and significantly decrease, to almost zero after both extraction methods.

Of the measurements of S1 for as-received samples, those of sample C2 appear to be much larger than all other as-received S1 measurements. This may be due to the use of oil-based mud (OBM) used while drilling this core sample causing contamination of this core.

Even if contamination did occur, free hydrocarbons within the system, were effectively extracted using both thermal and solvent extractions. In order to evaluate which extraction technique is more efficiently extracting free hydrocarbons, post-Dean Stark S1 is plotted against post-retort S1 (Fig. 28). With the exception of core sample C6, which has the highest measured vitrinite reflectance and lowest oil saturation, results of the sample suite show that Dean Stark extraction is more effective at extracting free hydrocarbons than retort extraction. It remains unclear whether Dean Stark extraction is more effective than thermal extraction at releasing hydrocarbons by cracking kerogen and producing additional “free” hydrocarbons.

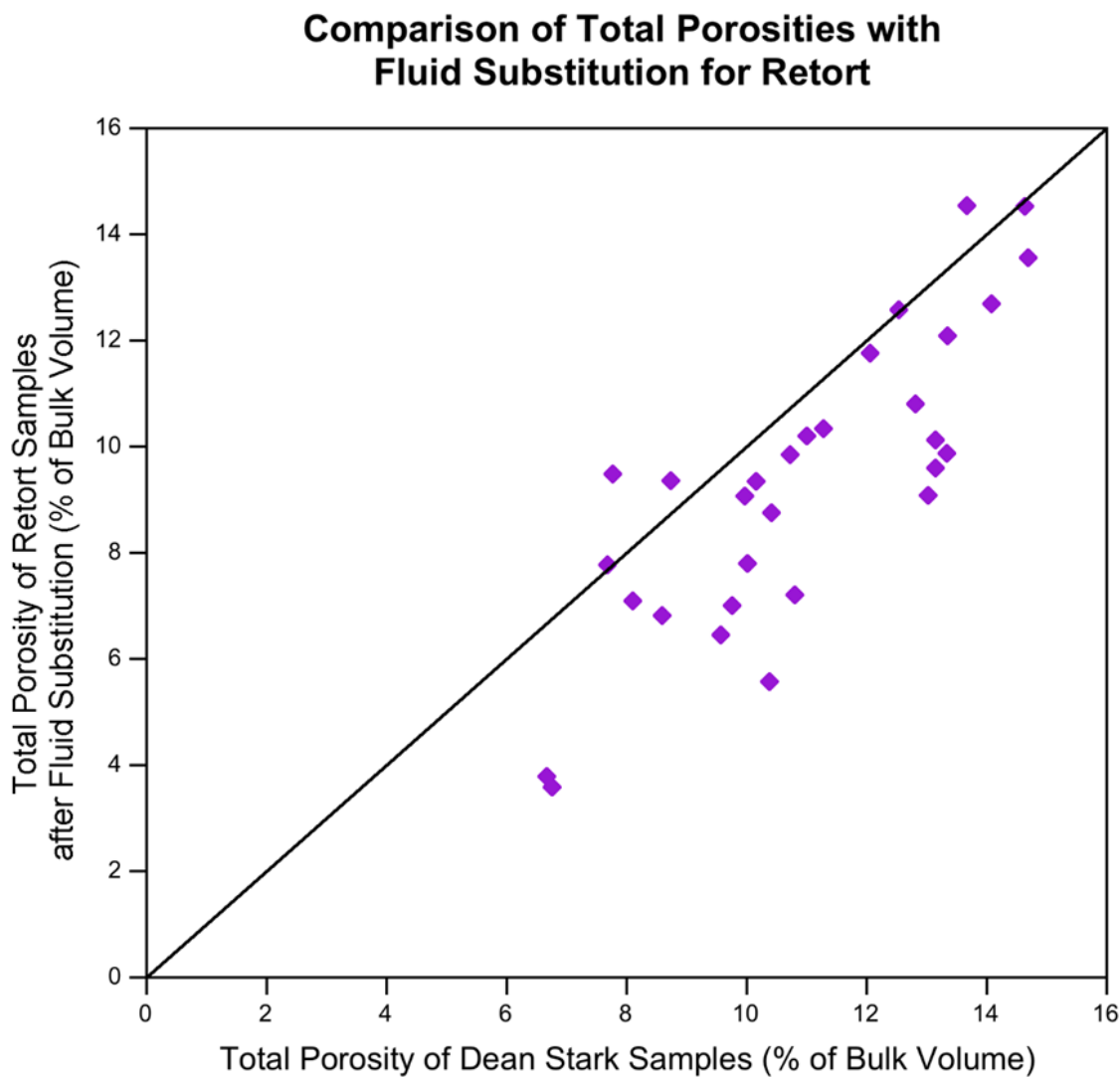


Figure 24. Comparison of total porosities with fluid substitution for retort. Chart comparing Dean Stark calculated total porosity, as % of bulk volume, against retort total porosities that have fluid substitution applied for samples collected at comparable core depths. The black line is representative of a one-to-one relationship between Dean Stark and retort porosities; points plotted nearest to this line demonstrate the most similar porosities. Dean Stark samples exhibit higher total porosities than those of fluid substituted retort samples.

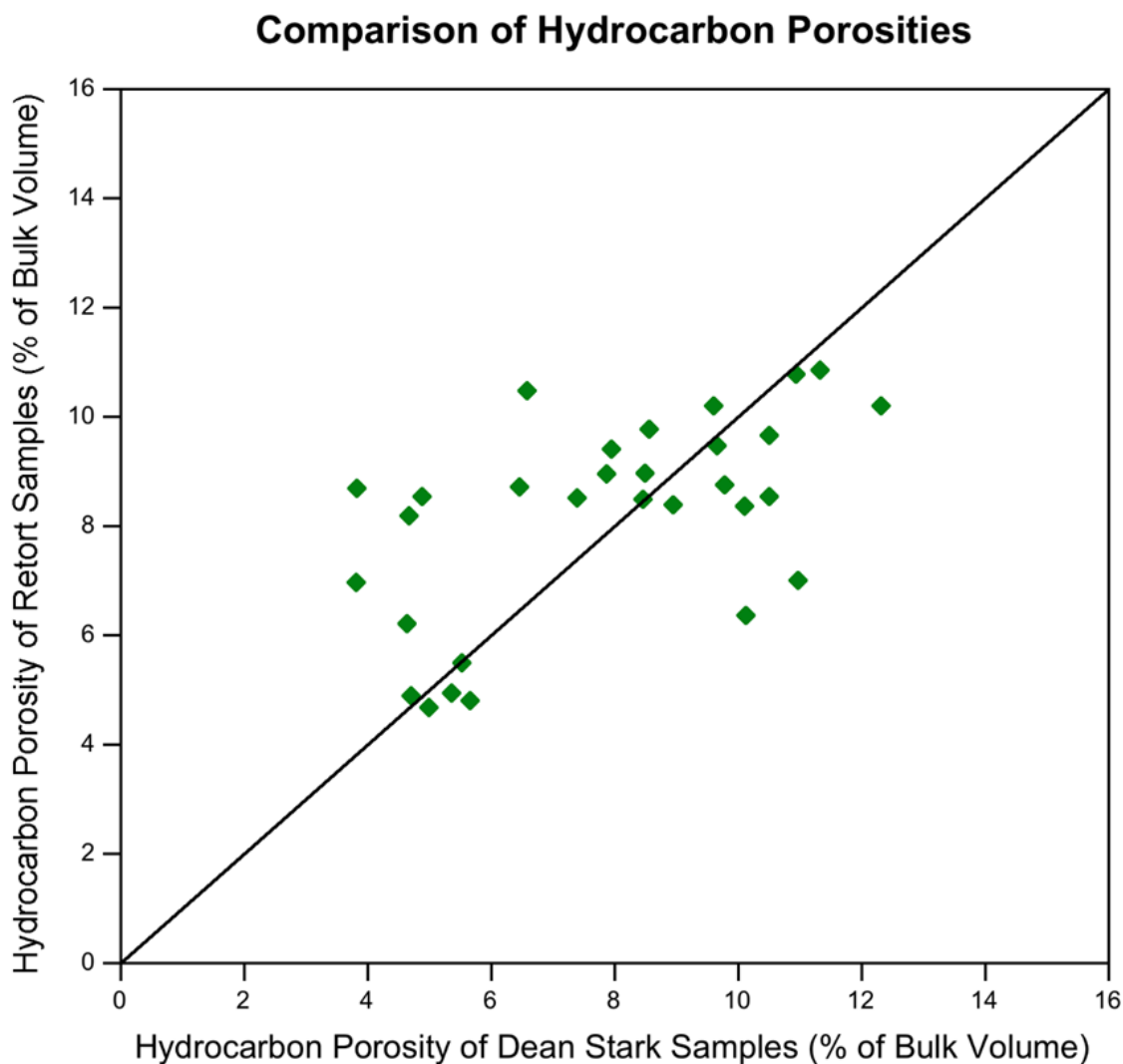


Figure 25. Comparison of hydrocarbon porosities. Chart comparing Dean Stark calculated hydrocarbon porosity, as % of bulk volume, against retort hydrocarbon porosity for samples collected at comparable core depths. The black line is representative of a one-to-one relationship between Dean Stark and retort hydrocarbon porosities; points plotted nearest to this line exhibit the most similar porosities.

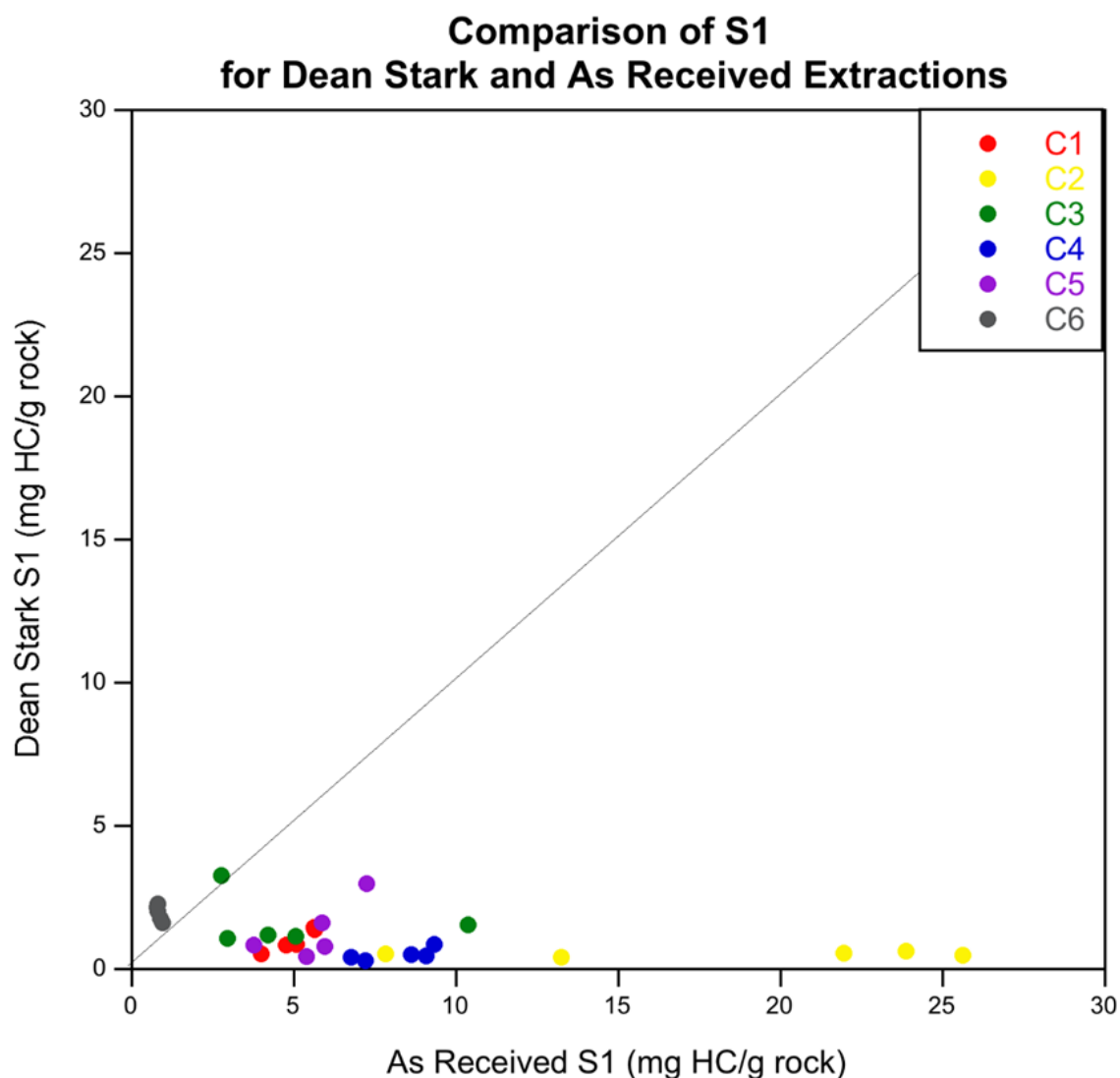


Figure 26. Comparison of S1 for Dean Stark and as-received extractions. Chart comparing post-Dean Stark S1 measurements, as mg HC/g rock, against as-received S1 measurements for samples collected at comparable core depths. The black line is representative of a one-to-one relationship between Dean Stark and as-received S1 values; points plotted nearest to this line exhibit the most similar S1 values. Overall, S1 measurements following solvent extraction as nearly zero. Note the inflated S1 values of C2 (possible oil based drilling mud contamination during drilling and core extraction).

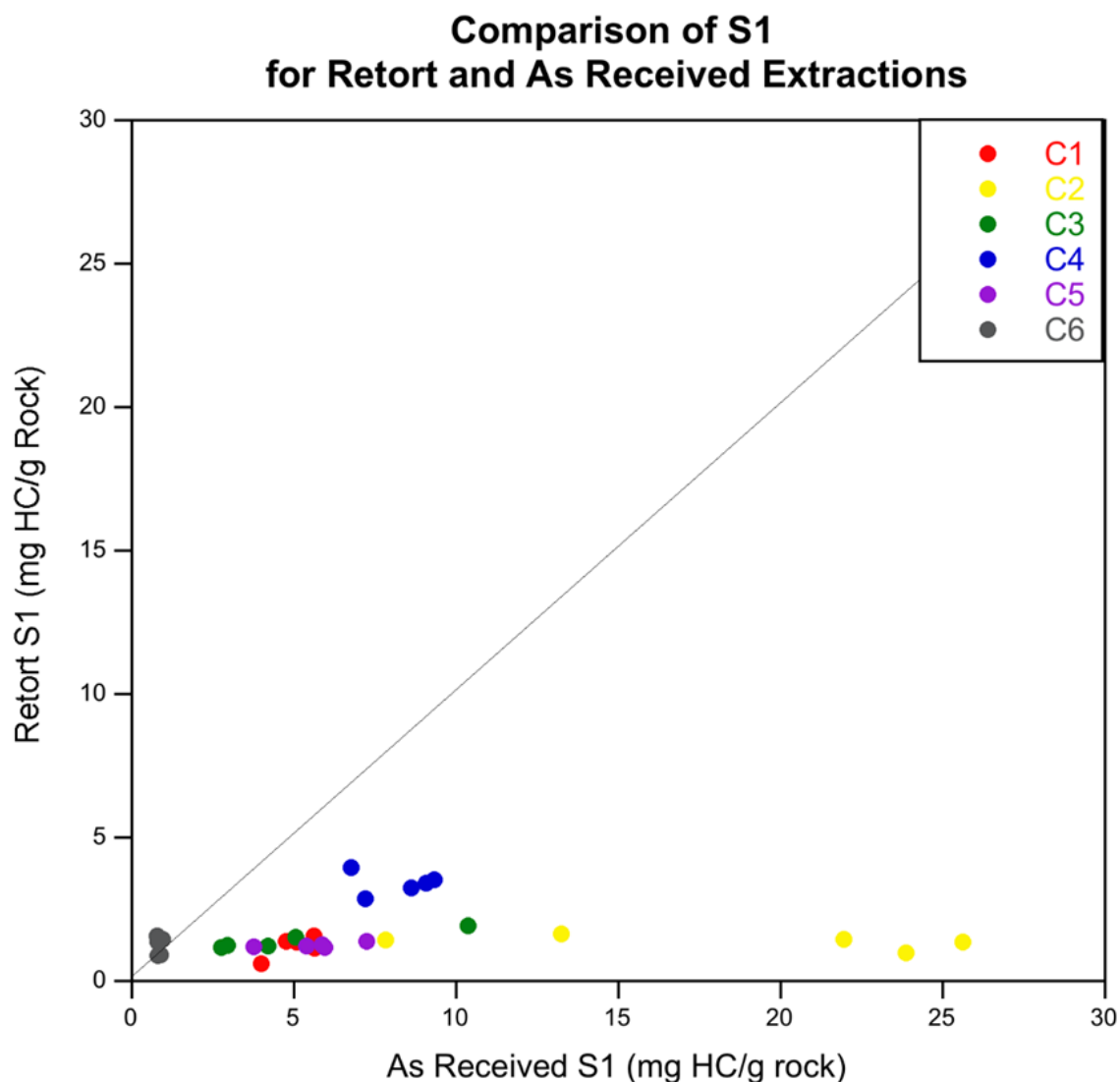


Figure 27. Comparison of S1 for retort and as-received extractions. Chart comparing post-retort S1 measurements, as mg HC/g rock, against as-received S1 measurements for samples collected at comparable core depths. The black line is representative of a one-to-one relationship between Dean Stark and as-received S1 values; points plotted nearest to this line exhibit the most similar S1 values. Overall, S1 measurements following solvent extraction are extremely reduced. Note the inflated S1 values of C2 (possible oil based drilling mud contamination during drilling and core extraction).

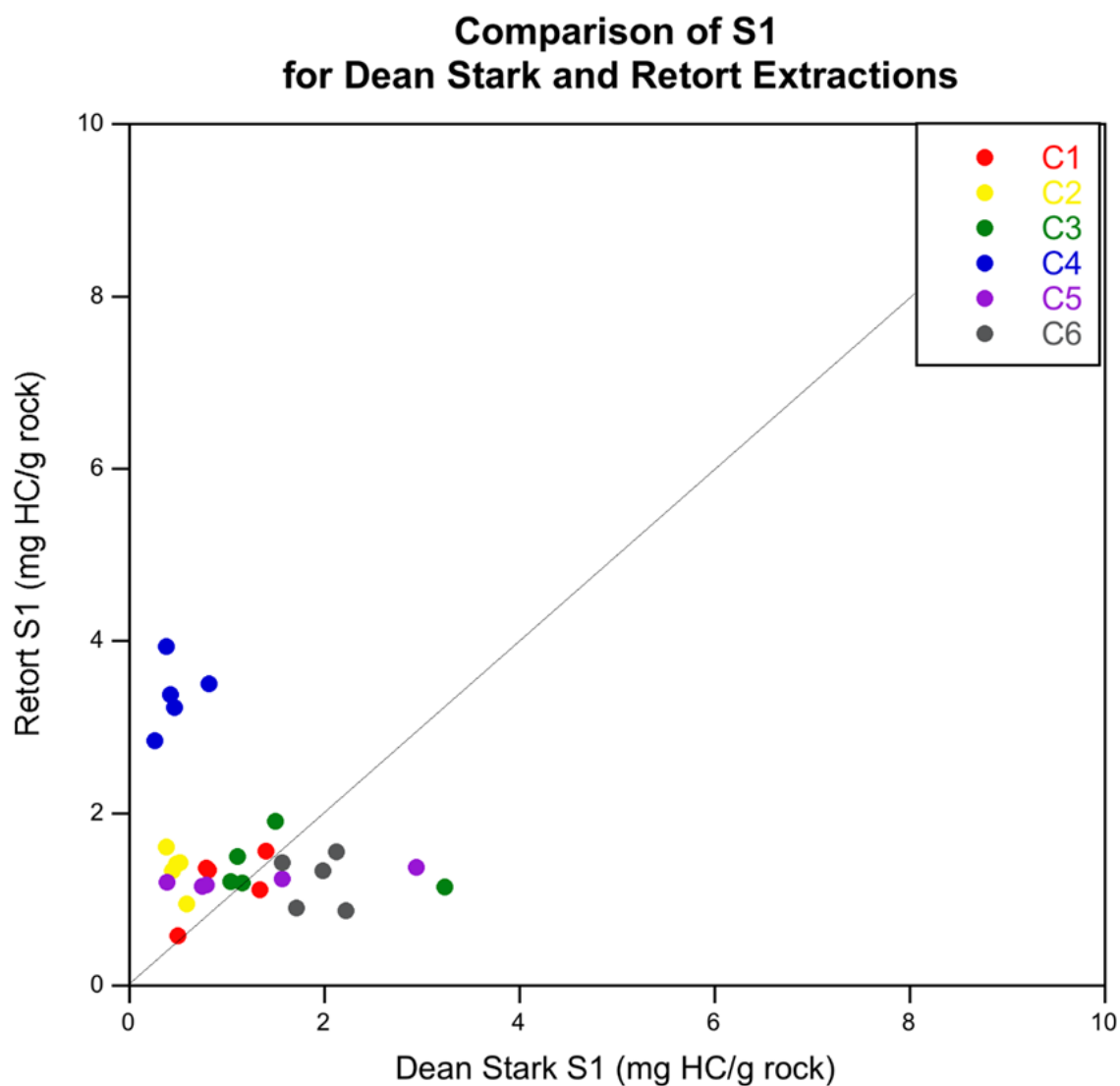


Figure 28. Comparison of S1 for Dean Stark and retort extractions. Chart comparing post-Dean Stark S1 measurements, as mg HC/g rock, with post-retort S1 measurements for samples collected at comparable core depths. The black line is representative of a one-to-one relationship between Dean Stark and retort S1 values; points plotted nearest to this line exhibit the most similar S1 values. Overall, S1 measurements following solvent extraction are higher than those measured following thermal extraction.



Measurements of S2, the hydrocarbon potential, of the post-Dean Stark samples are reduced relative to S2 values of as-received samples (Fig. 29), while S2 values of post-retort samples are similar to those of as-received samples (Fig. 30).

The drop in S2 resulting from Dean Stark solvent extraction implies that kerogen, the nonvolatile, insoluble, organic matter that may crack during thermal extraction, is not the only organic matter measured by S2. The S2 peak must also be due to a soluble, heavier organic component remains in the system during thermal extraction during which S1 is reduced. The likely organic component that accounts for this is bitumen, which is heavier than S1 organics and soluble during extraction (Collins and Lapierre, 2014), but it is not generally associated with S2 (Equations 2 and 3).

When comparing S2 values of post-Dean Stark and with post-retort samples (Fig. 31), a similar relationship is found as when comparing post-Dean Stark with as-received (Fig. 29). Since as-received S2 and post-retort S2 values appear to be approximately equivalent, it is likely that they can be used interchangeably, but the uncertainties in post-retort S1 measurements leave questions about the accuracy of the post-retort S2 measurements. Thermal extraction could lead to some cracking of new hydrocarbons, thereby increasing S1 and decreasing S2 values of post-retort pyrolysis measurements.

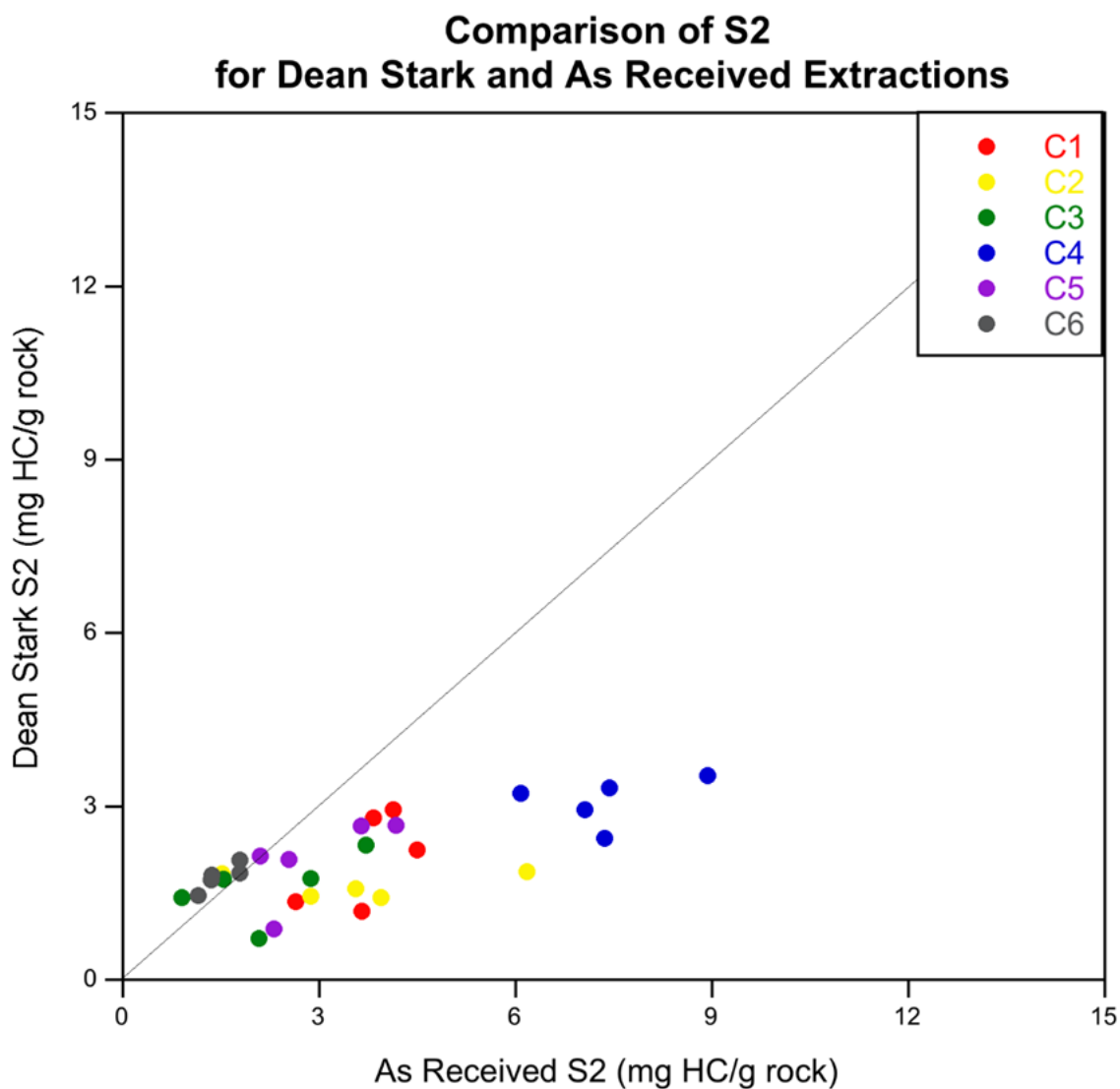


Figure 29. Comparison of S2 for Dean Stark and as-received extractions. Chart comparing post-Dean Stark S2 measurements, as mg HC/g rock, against as-received S2 measurements for samples collected at comparable core depths. The black line is representative of a one-to-one relationship between Dean Stark and as-received S2 values; points plotted nearest to this line exhibit the most similar S2 values. Overall, S2 measurements post solvent extraction are greatly reduced.

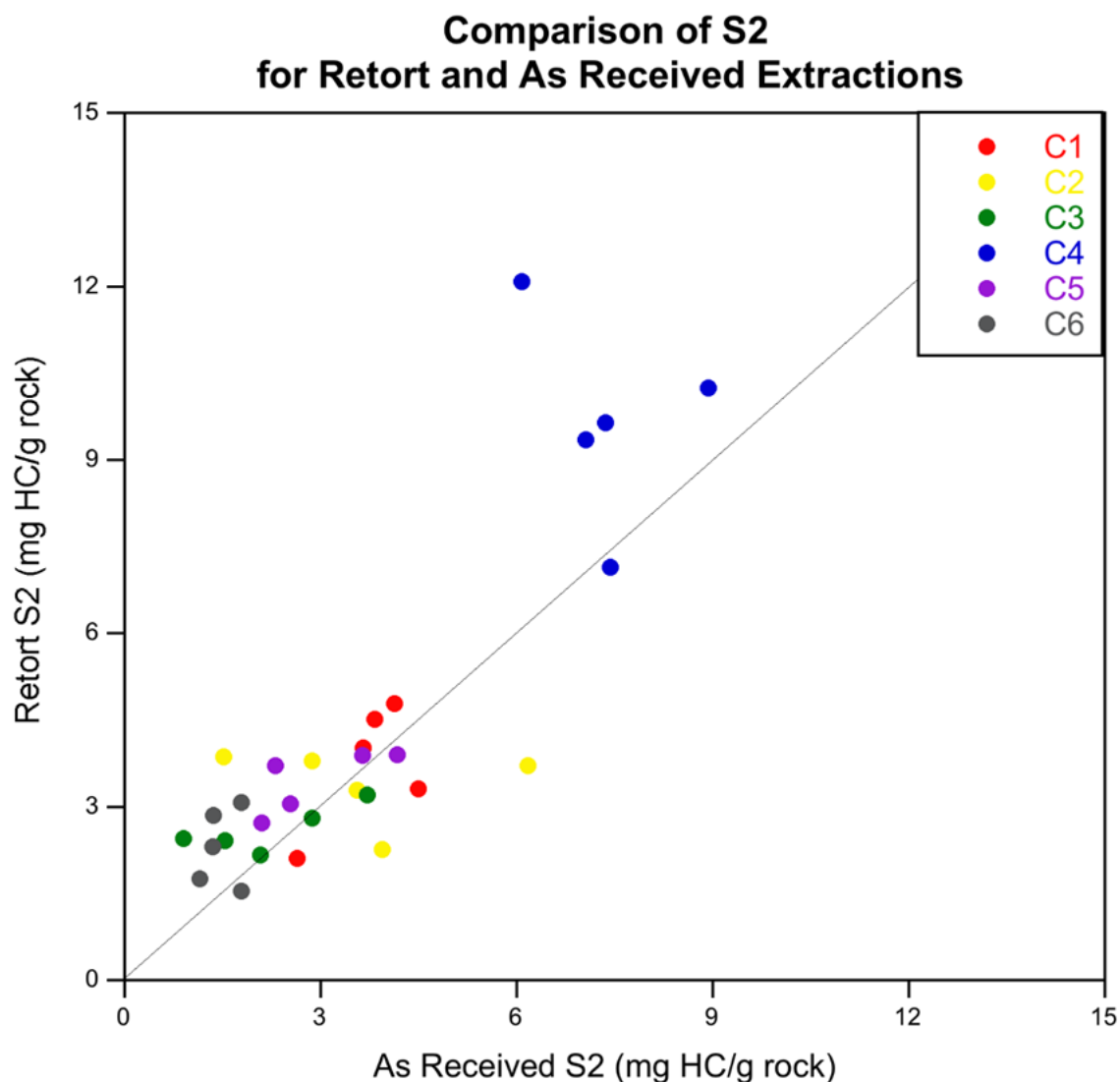


Figure 30. Comparison of S2 for retort and as-received extractions. Chart comparing post-retort S2 measurements, as mg HC/g rock, against as-received S2 measurements for samples collected at comparable core depths. The black line is representative of a one-to-one relationship between retort and as-received S2 values; points plotted nearest to this line exhibit the most similar S2 values. Overall, S2 measurements post solvent center around the one-to-one line, implying equivalent S2 reading pre- and post-thermal extraction.

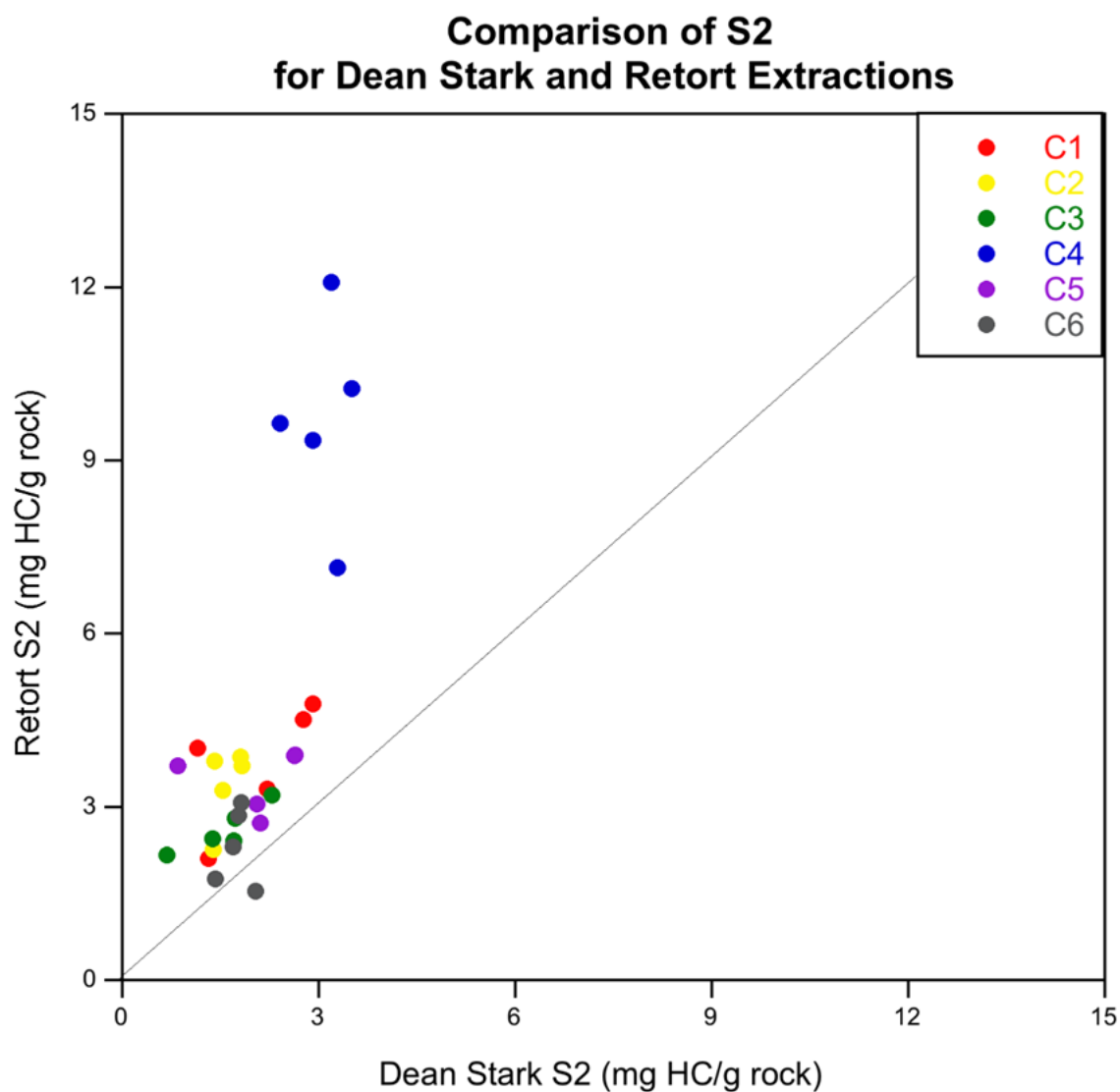


Figure 31. Comparison of S2 for Dean Stark and retort extractions. Chart comparing post-Dean Stark S2 measurements, as mg HC/g rock, with post-retort S2 measurements for samples collected at comparable core depths. The black line is representative of a one-to-one relationship between Dean Stark and retort S2 values; points plotted nearest to this line exhibit the most similar S2 values. Overall, S2 measurements following solvent extraction are lower than those following thermal extraction.

## *5.2 Organic matrix and hydrocarbon mobility*

The porosity, pyrolysis, and LECO TOC data give insights into the organic components of both the rock matrix and mobile and non-mobile components of pore space. Types of reservoir matrix, pore-filling fluids and organic matrix materials are summarized in Figure 32.

### *5.2.1 Matrix-contributing organic matter*

Measurements of S1' is key to quantifying the kerogen contributing portion of the shale matrix as well as the hydrocarbon mobility of the pore fluids. By comparing S2 values of as-received, post-retort, and post-Dean Stark data (Fig. 33), S1' can be understood as the difference between as-received and post-Dean Stark S2, or the difference between the solid black one-to-one line and the dashed blue line. For this data set, S1' represents approximately half of the total S2, but additional work will need to be done to confirm whether or not this pattern holds true for all unconventional reservoir shale samples.

In order to quantify the total matrix-contributing amount (weight %) of TOC in the shale structure, the as-received TOC ( $TOC_{AR}$ ), S1 ( $S1_{AR}$ ) and S2 ( $S2_{AR}$ ) along with the post-Dean Stark S2 measurements ( $S2_{post DS}$ ) are required. If hydrocarbon density is assumed to be  $0.83 \text{ g/cm}^3$ , “Adjusted TOC” ( $TOC_{ADJ}$ ) can be calculated by:

$$TOC_{ADJ} = TOC_{AR} - 0.83[S1_{AR} + (S2_{AR} - S2_{post DS})] \quad (10)$$

The Adjusted TOC is the matrix-contributing portion of TOC. By quantifying this  $TOC_{ADJ}$  and ignoring any the bitumen portion of the TOC, more accurate bulk densities can be applied for petrophysical evaluations (Fig. 34).

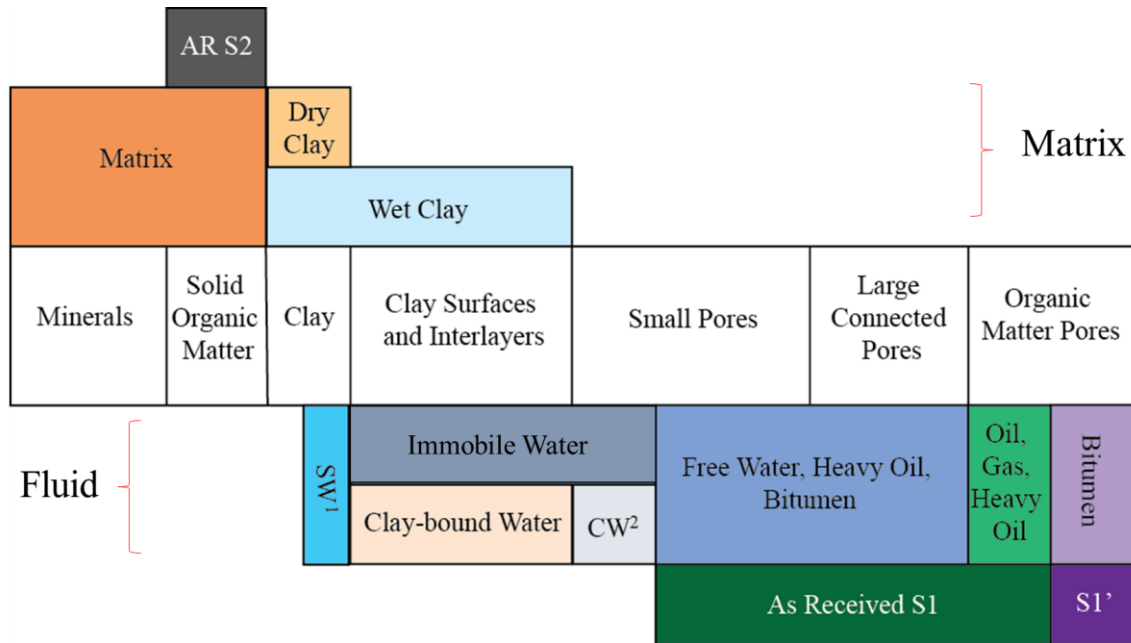


Figure 32. Shale matrix and pore components and corresponding pyrolysis measurements. Chart categorizing the matrix contributing components within unconventional reservoir shales and fluid types contributing to both the matrix structure and pore-storage components. 1. SW – structural water, 2. CW – capillary water. Components measured by S1, S2, and S1' have been indicated.

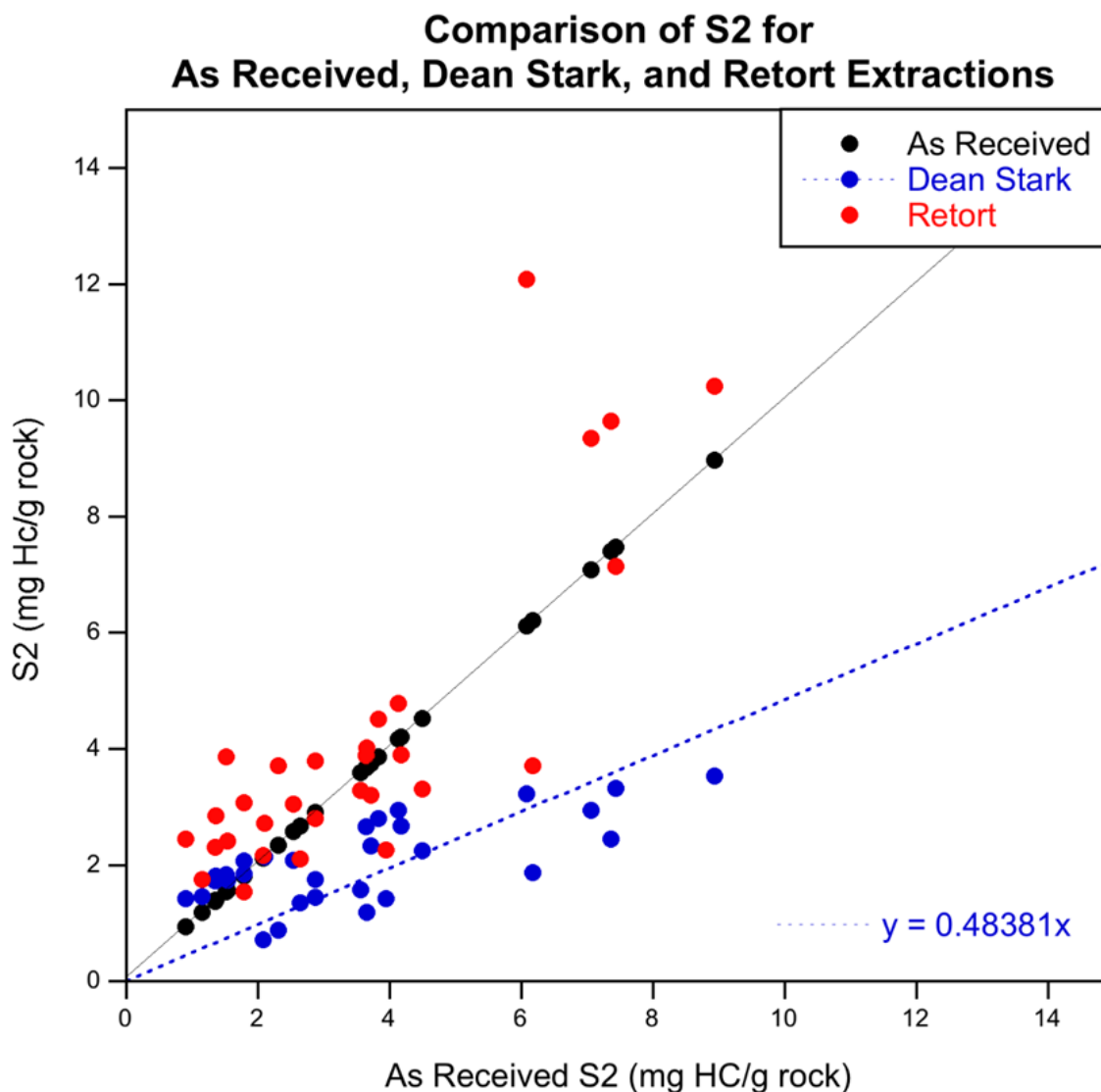


Figure 33. Comparison of S2 for as-received, Dean Stark and retort extractions. Plot comparing post-Dean Stark S2 measurements, as mg HC/g rock, as-received S2 measurements, and post-retort S2 measurements. The black line is representative of a one-to-one relationship with as-received S2 values; points plotted nearest to this line exhibit the most similar S2 values. Overall, S2 measurements of post-solvent extraction samples are greatly reduced, implying a soluble heavy organic component, which is extracted during Dean Stark. S2 measurements following thermal extraction are approximately equivalent to as-received S2 measurements; retort fails to extract the soluble heavy organic component that Dean Stark extracts.

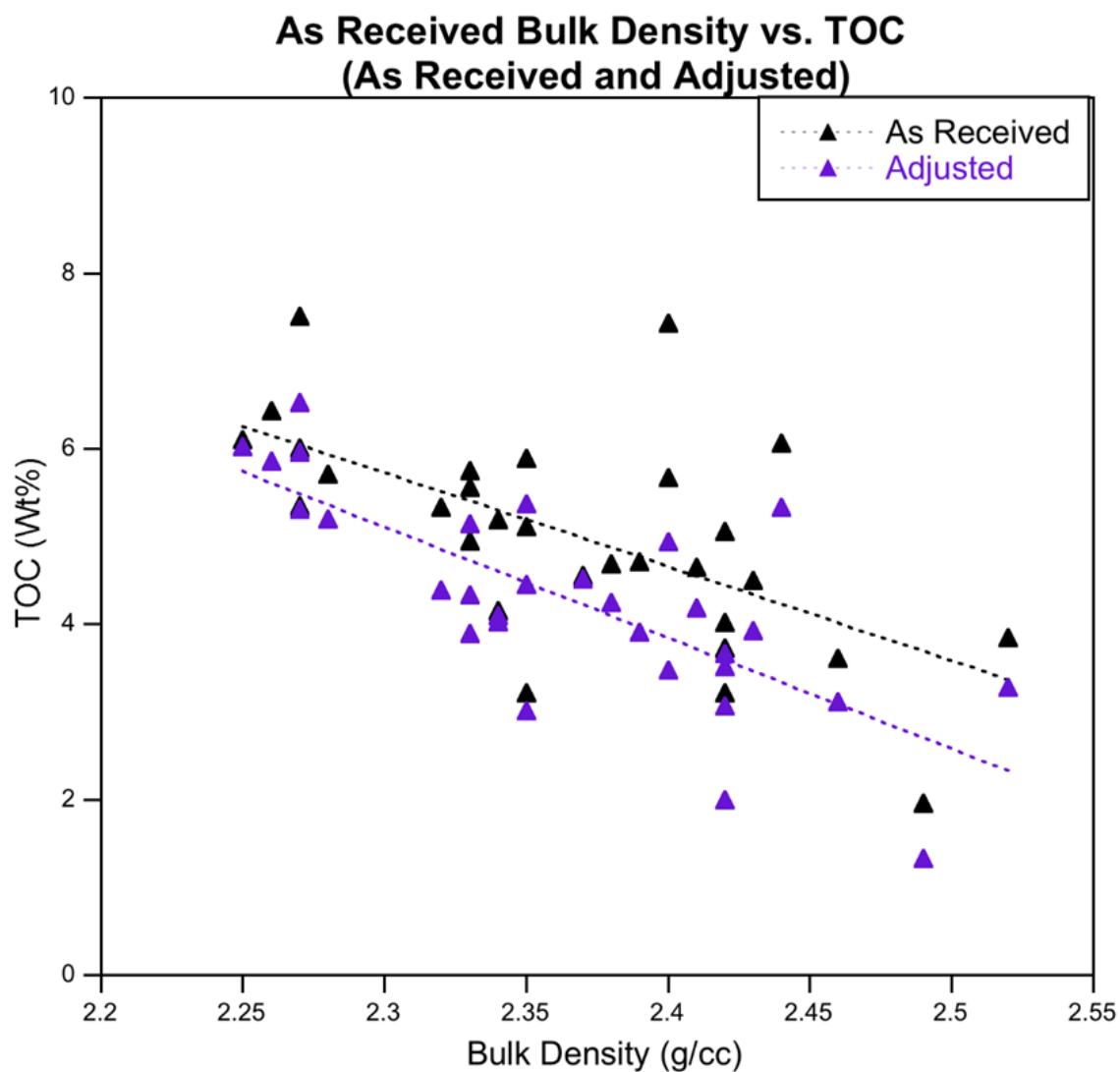


Figure 34. As-received bulk densities vs. TOC (as-received and adjusted). Chart comparing as-received TOC, as weight percent, with adjusted TOC (Equation 10). Both TOC and adjusted TOC are plotted against as-received bulk densities for comparison. Best fit lines have been applied in order to facilitate trend observations. The As-received data exhibits overall higher TOC values compared to adjusted data; by adjusting TOC values using Equation 10, an organic content which is representative of matrix contribution is expressed.



### 5.2.2 Mobility

Estimating hydrocarbon mobility, or the mobile portion of the calculated total hydrocarbon porosity, is important to the economic viability of a well. The porosity measurements combined with the pre- and post-extraction pyrolysis measurements can be used to determine the potentially flowable portion of hydrocarbons, which for the sake of this paper will be referred to as “mobility.”

Earlier observations and discussions highlight possible problems using retort measurements due to probable cracking, or creation, of new hydrocarbons during thermal extraction. Therefore, I will not discuss hydrocarbon mobility on the basis of retort measurements. Instead, the discussion will depend on as-received and post-Dean Stark measurements.

The as-received S1 measurements suggested possible OBM contamination, so these S1 measurements will also be avoided. S1', as calculated in Equation 3, quantifies the immobile (heavy) portion of the hydrocarbons and can be used to correct hydrocarbon porosities by first determining what percentage of the pore-volume is immobile:

$$\varphi_{S1'} = \frac{1}{10} S1' \rho_{bitumen} \rho_{grain} \quad (11)$$

and then determining what percentage of the hydrocarbon porosity is effectively mobile:

$$\%Mob = 100[1 - (\frac{\varphi_{S1'}}{\varphi_{hc}})] \quad (12)$$

where %Mob is the mobile percentage of hydrocarbon porosity, and  $\varphi_{hc}$  is the total hydrocarbon porosity. The %Mob is defined to quantify the percent of hydrocarbons that

are able to flow from pore spaces and be collected at a wellhead in ideal conditions (i.e. ignoring capillarity and permeability).

Understanding the relationship between %Mob and maturity may provide an efficient means of determining effective (producable) hydrocarbon porosity with only Dean Stark porosity measurements and maturity data (%Ro). By plotting %Mob, as calculated by Equation 11, against measured %Ro, a relatively strong linear trend is evident (Fig. 35). The least mature (lowest %Ro) samples have the lowest percentage of mobile hydrocarbons (lowest %Mob), and therefore the greatest amount of heavy bituminous organic matter (S1') with a slope of approximately 30 %Mob/%Ro. The most mature samples prove to have the highest percentage of mobile hydrocarbons, approaching nearly 100% mobility, implying little to no S1.'

The best fit line determined in Figure 35 was then applied to a plot of %Mob vs. calculated %Ro in order to assess whether or not calculated maturity is sufficient to predict %Mob (Fig. 36). However, a wider variance from the best-fit line is exhibited, when using calculated %Ro than observed using measured %Ro. Thus, better predictions of hydrocarbon mobility can be made using measured %Ro.

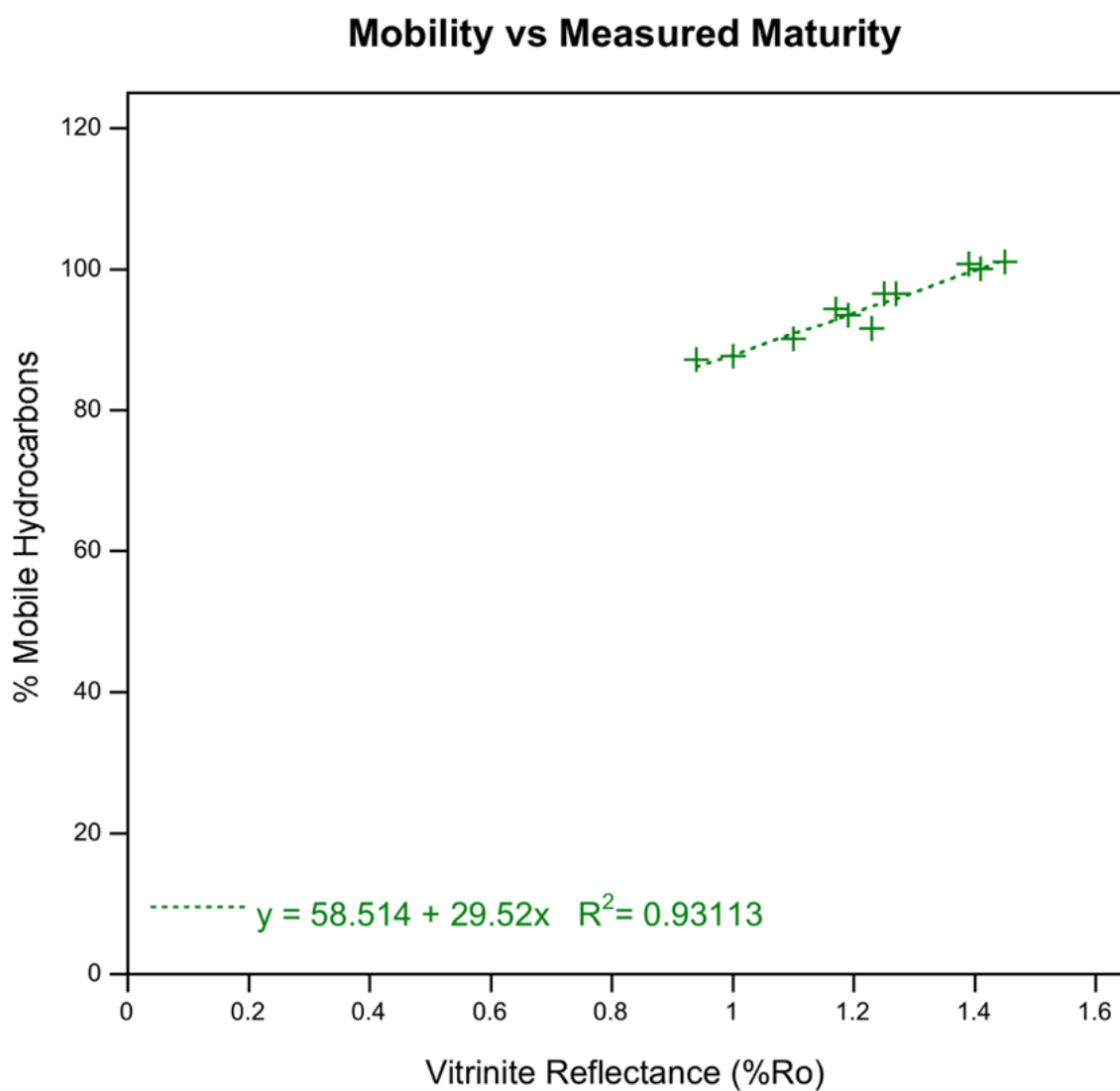


Figure 35. Mobility vs. measured maturity. Chart displaying linear relationship between measured maturity, or vitrinite reflectance (%Ro) and percent mobility of hydrocarbons (%Mob). A strong relationship is apparent with a slope of 30 %Mob/%Ro, with  $R^2 = 0.93$ .

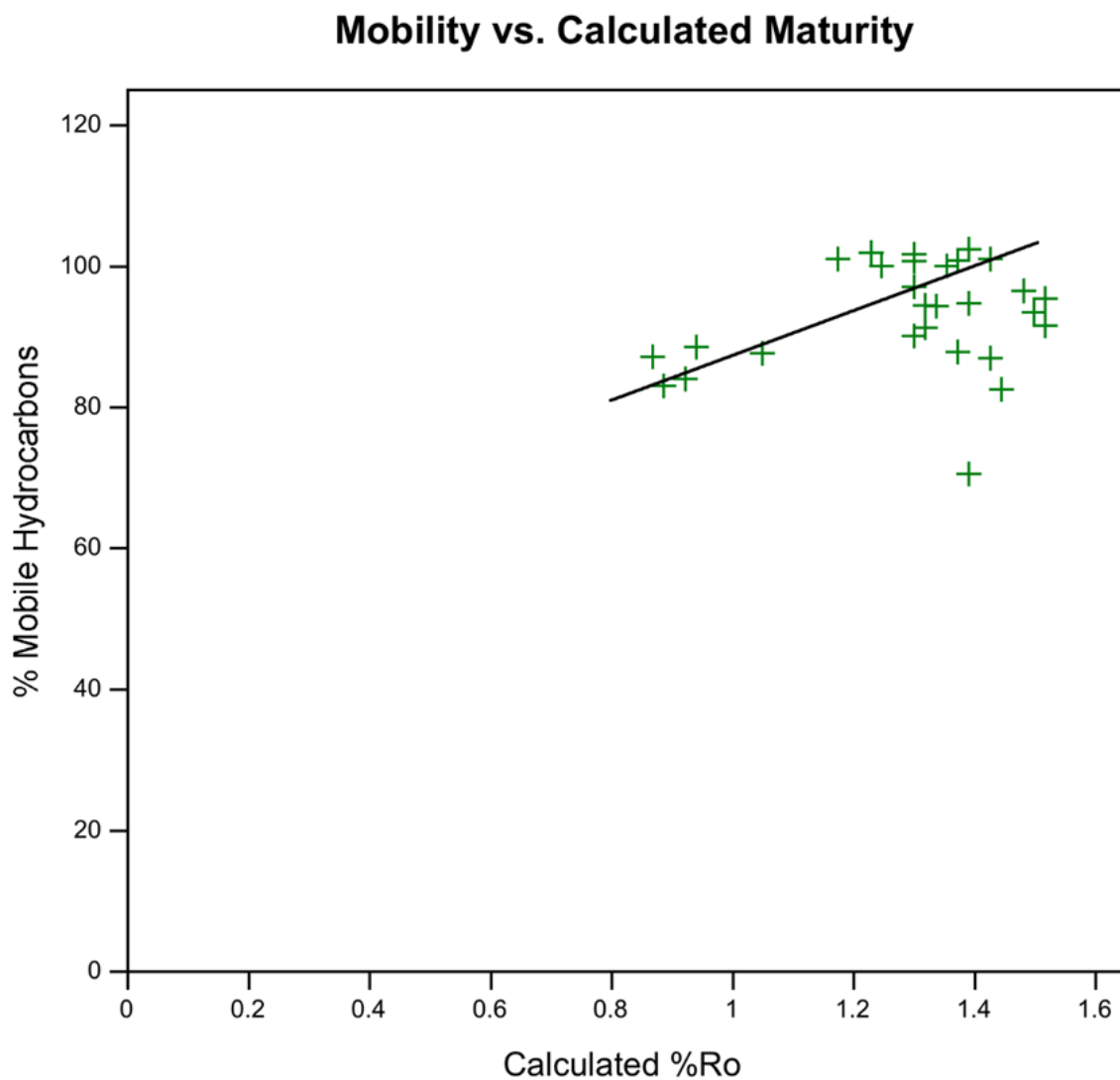


Figure 36. Mobility vs. calculated maturity. Chart displaying positive linear relationship between calculated maturity, or vitrinite reflectance (%Ro) and percent mobility of hydrocarbons. The black line represents the best-fit relationship from Figure 35. Measured maturity proves to be a better indicator of % mobility compared with calculated maturity.

### *5.3 Compositional analysis and imaging*

Compositional analysis of the shale core material was attempted at several scales. MicroXRF and XRD were completed first in order to identify areas of interest and expected percentages of mineralogical components. Using this information as a guide, reflected light microscopy gave insight into significant structures and morphology within the samples. These images became starting points for higher resolution electron microprobe and SEM observations.

#### *5.3.1 General composition*

Processed MicroXRF (Fig. 14) images reveal mixed calcite/clay/quartz layers within macroscopically homogeneous shale core. Within these mixed beds are distinguishable, thin laminations of calcite-rich layers. Pyrite can also be identified in the samples. The focus of the higher resolution imaging began by isolating areas of interest, which included samples from the mixed calcite/clay/quartz layers as well as the calcite-rich layers and areas that were relatively high in pyrite as well as some that exhibited very little pyrite within the MicroXRF images.

Once these sampling locations were identified, reflected light microscopy was used to obtain images at 20X magnification and 50X magnification (Fig. 15). Within these images, numerous and diverse foraminifera are surrounded by very fine-grained dark material. These forams range in size from tens of microns to several hundred microns in diameter. Inside of the forams are various materials; some light in color (matching the foraminifera shell material), some darker, some are completely filled,

while some are only partially filled or apparently empty. The forams more densely populate the calcite-rich layers of the MicroXRF regions but are still present in the mixed calcite/clay/quartz regions. WDS was used to confirm that the foram shells are composed of calcite (Fig. 16). The diversity in forams also suggests calcitic shells as opposed to foram shells composed of aragonite.

Relatively large (several hundred microns) areas of the shale samples consist of light-medium colored amorphous material, which were analyzed using BSE in order to estimate density. Filled fractures were also imaged using reflected light microscopy, and appear to be filled with light-colored substance suggesting organic matter.

### *5.3.2 Density-based quantification*

XRD, MicroXRF, reflected light microscopy, and WDS provide general mineralogical and microstructural information about the shale samples, but individual grain identification requires additional data and increased resolution. SEM provides high-resolution images, whose individual grains can be analyzed by BSE for density differences. Table 5 is a compilation of common minerals and solids and their corresponding densities. Together, Figures 18 and 19 illustrates the various shades of gray in BSE images, corresponding to density ranges, exhibited within the sampled regions. The brightest framboidal regions correspond to pyrite with a high density of  $5.0 \text{ g/cm}^3$ , while the darkest areas correspond to pore space with essentially zero density. Using ImageJ Software, the LUT # counts from 8-bit grayscale images can be obtained (Fig. 37)

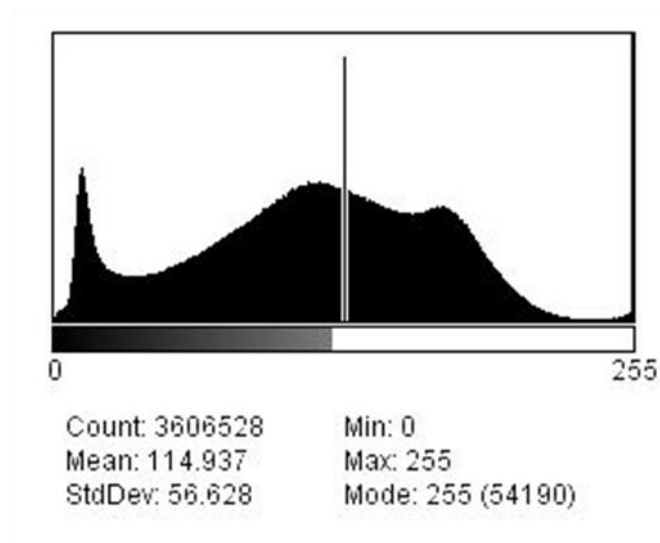
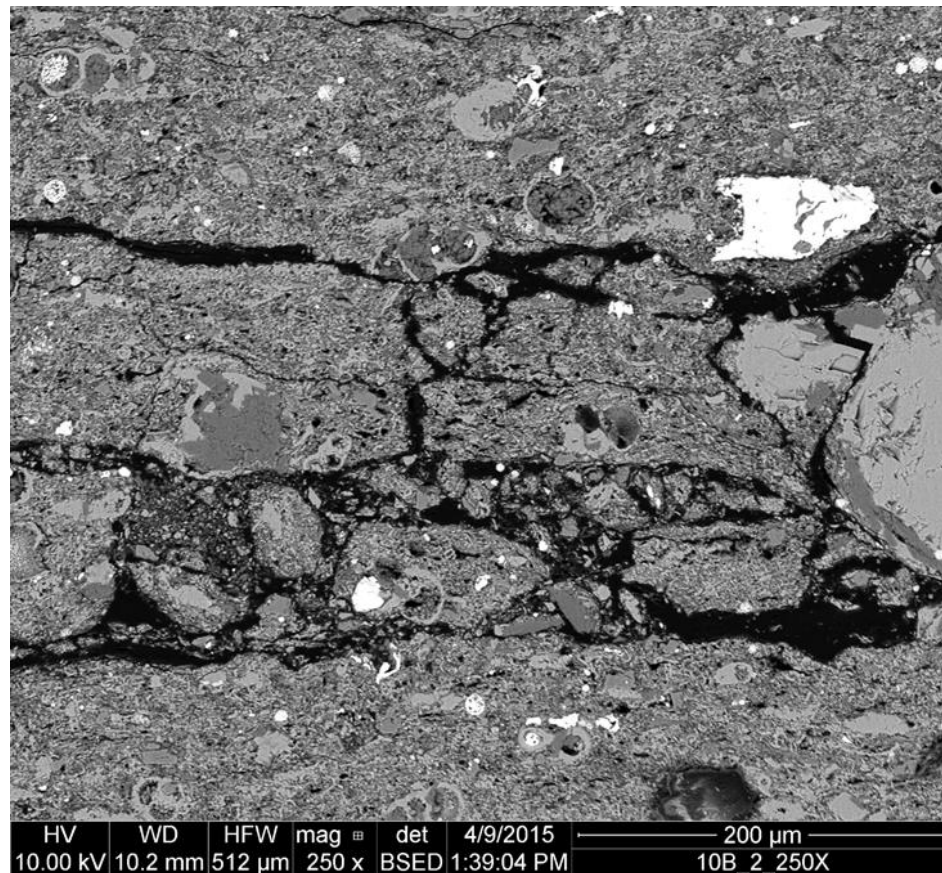


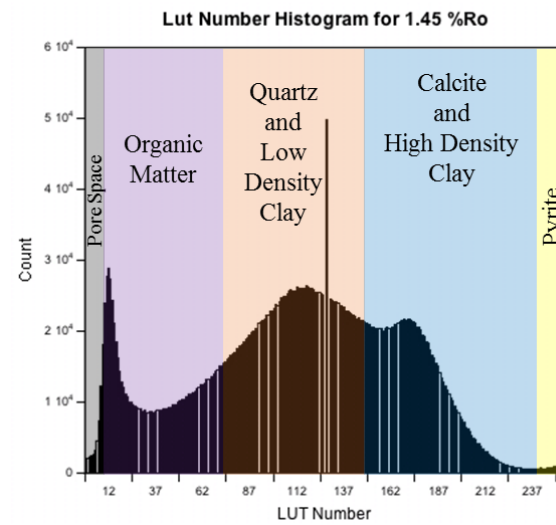
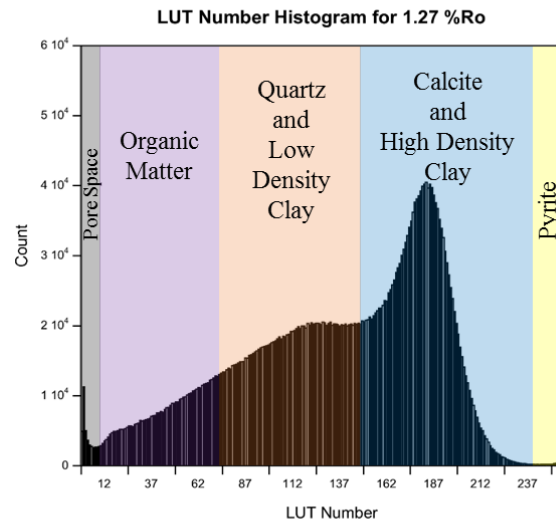
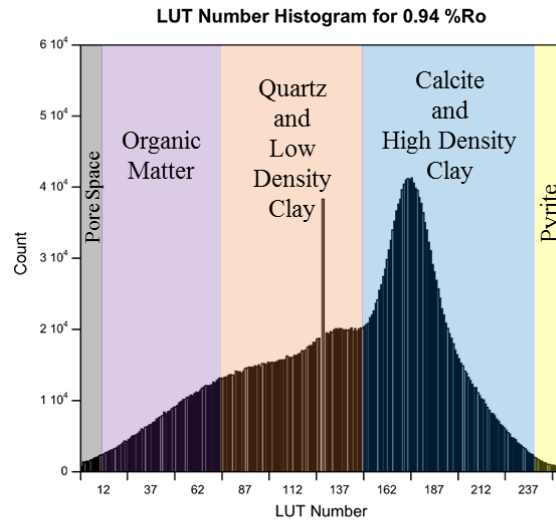
Figure 37. 8-bit grayscale backscattered electron images and corresponding histograms. BSE images collected for sample 10B using a 10 kV beam and a working distance of 10 mm, displayed at 250X with a HFW of 512  $\mu$ m and corresponding histogram of LUT # (0 – 255) distribution for 8-bit image.

The XRD data that were collected provide bulk percentages of calcite, clays, organic matter, pyrite, and quartz expected in each location. However, because the XRD data was collected from a larger sample size, the values can only be used as approximate compositions for any small area imaged. This compositional information provides a basis for determining representative LUT # ranges for corresponding density ranges of known materials.

ImageJ may be used to isolate a given range of for LUT # and produce false color images which can be utilized to determine spatial distributions of phases with given densities, with distinct cutoffs. Original BSE image cutoffs were set based on XRD values and corresponding LUT#s (see Appendix B). This was performed for all imaged areas on the lowest resolution BSE image of each (250X – 1500X) (Fig. 39). The best determination of LUT #s and corresponding densities was determined from this analysis and is displayed in Table 11. Clays exhibit a wide range of densities, and therefore have been separated into low-density clays, grouped with quartz, and high-density clays, grouped with calcite. Based on the structure of the fine-grained material imaged on the SEM, the clay is primarily illite, with an expected density of 2.6-2.9 g/cm<sup>3</sup>.



Figure 38. Lookup table histogram of 8-bit backscattered electron images with compositional ranges. Histograms of LUT # (0-255) extracted from 8-bit grayscale BSE images. Histograms for 3 different maturities are exhibited (0.94 %Ro, 1.27 %Ro, and 1.45 %Ro), and LUT # ranges corresponding to pore space, organic matter, quartz and low- density clay, calcite and high density clay, and pyrite have been identified based on their known densities.



Lookup Table Ranges and Corresponding Densities			
LUT Range	False Color	Probable Mineral	Density (g/cm <sup>3</sup> )
0-10	Lime Green	Pore Space and V.Lt. Organics (Gas, Oil)	0-0.6
11-70	Black to Purple	Organic Matter (Crude Oil, Bitumen, Kerogen)	0.8-2.2
71-150	Fuschia - Orange	Quartz and Light Clays	2.2-2.65
151-239	Lt. Orange - Yellow	Calcite and Heavy Clays	2.7-3.0
240-255	Lt. Yellow - White	Apatite, Marcasite, and Pyrite	3.15-5.0

Table 11. Lookup table ranges and corresponding densities. Table displaying lookup table ranges and corresponding assigned “false color” densities associated with minerals from lowest to highest image brightness (LUT #).

An analysis of the percentage of area imaged BSE-determined mineral and TOC was compared with phase percentages determined by bulk XRD measurements, successfully over all SEM images. All of the collected sampling location BSE percent areas for each depth were averaged in a group designated as “All.” Calcite-rich sampling locations were averaged together and designated as in “Ca-rich” layers, and mixed calcite/clay/quartz layers were averaged, designated as “Avg Ca.” Comparisons of XRD and BSE and LUT # results are illustrated in Figure 39.

In confirmation of the chosen BSE image brightness (LUT #) cutoffs chosen, the BSE-inferred percent area measurements of minerals and solids are comparable to the XRD volumes for all regions of samples as well as compositional layers rich in calcite, clay and quartz, pyrite, mixed regions, and TOC. The compared values plot around the one-to-one line, and therefore support the LUT # ranges set for analysis, although variance is exhibited that is likely due to local variations in lithology at a fine scale.

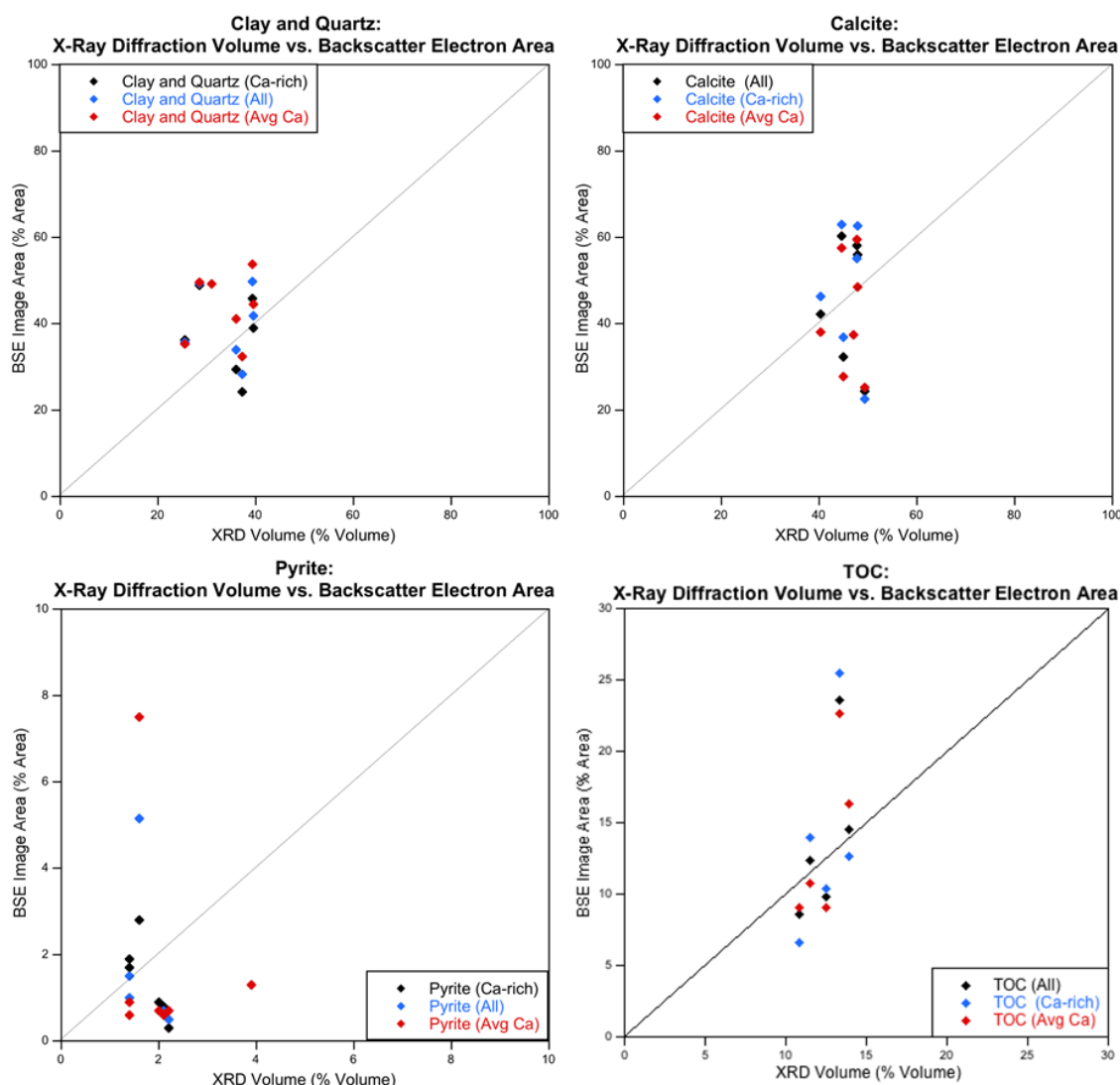


Figure 39. X-ray diffraction volume vs. backscattered electron area comparison: clay and quartz, calcite, pyrite, and TOC. Charts displaying comparisons of mineralogy percentages as determined by bulk XRD methods and BSE image analysis, as with chosen brightness (LUT #) cutoffs, summing over all images for a given sample (All), calcite-rich layers (Ca-rich), and average calcite content layers, for average values collected in calcium-rich (blue), average calcium (red), and all (black) locations on analyzed polished plates. The black lines represent a one-to-one relationship between XRD volumes and BSE image areas; points plotted nearest to this line exhibit the most similar porosities.

Lookup tables can be made in ImageJ in order to more easily visualize density differences in BSE images. Figure 40 is a modified version of the Fire lookup table in ImageJ that has been adjusted, based on the values in Table 11, to clearly indicate pore space. Applying this lookup table (Fig. 41) creates a clearer way of visualizing the pore space in the BSE image using a false color scale that facilitates visual inspection and evaluation of spatial distributions of phases at fine SEM scales.

Macroscopic techniques including XRD and MicroXRF prove to be inadequate when attempting to study microstructural characteristics of organic matter, but do provide useful diagnostic information of the character of the shale organics. Microscopic techniques consisting of reflected light microscopy, electron microprobe WDS, and BSE also fall short in terms of identification of organics. Physical and chemical confirmation of organic matter is challenging because of the limits of detection for C by WDS. Also, the amorphous character and density are the primary identifiable characteristics of organic matter by BSE. Yet sample preparation for BSE imaging can only preserve the less volatile organic material remains of samples. These less volatile organics are primarily immobile and have higher densities than mobile hydrocarbons. Thus, they are less distinguishable from light clays in BSE images than expected for the volatile organics, which were released from samples.

The pore space appears to be located primarily within the lower density organic material. The fracture-filling material has low densities ( $< 2.2 \text{ g/cm}^3$ ) and, based on morphology and density, it is assumed to consist of organic matter. The foram shells exhibit density values in line with calcite, confirming their composition. Some foram

shells are filled with calcite, some with pyrite, some with a mixture of low-density clay (kaolinite) and organic matter acting as organic pore space.

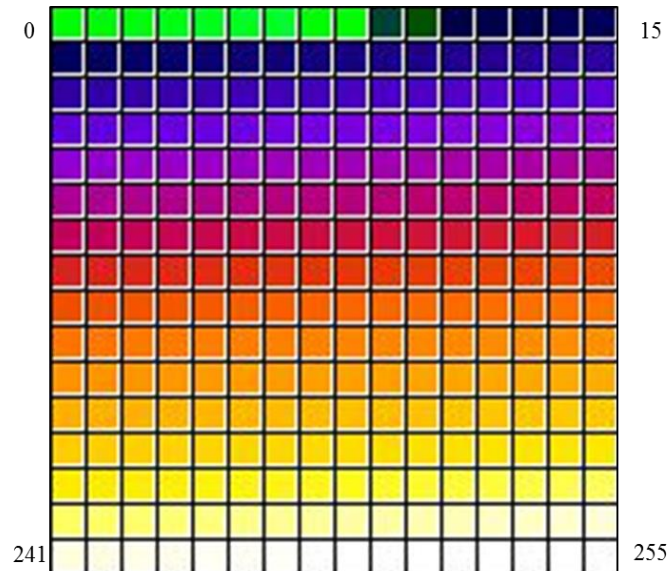
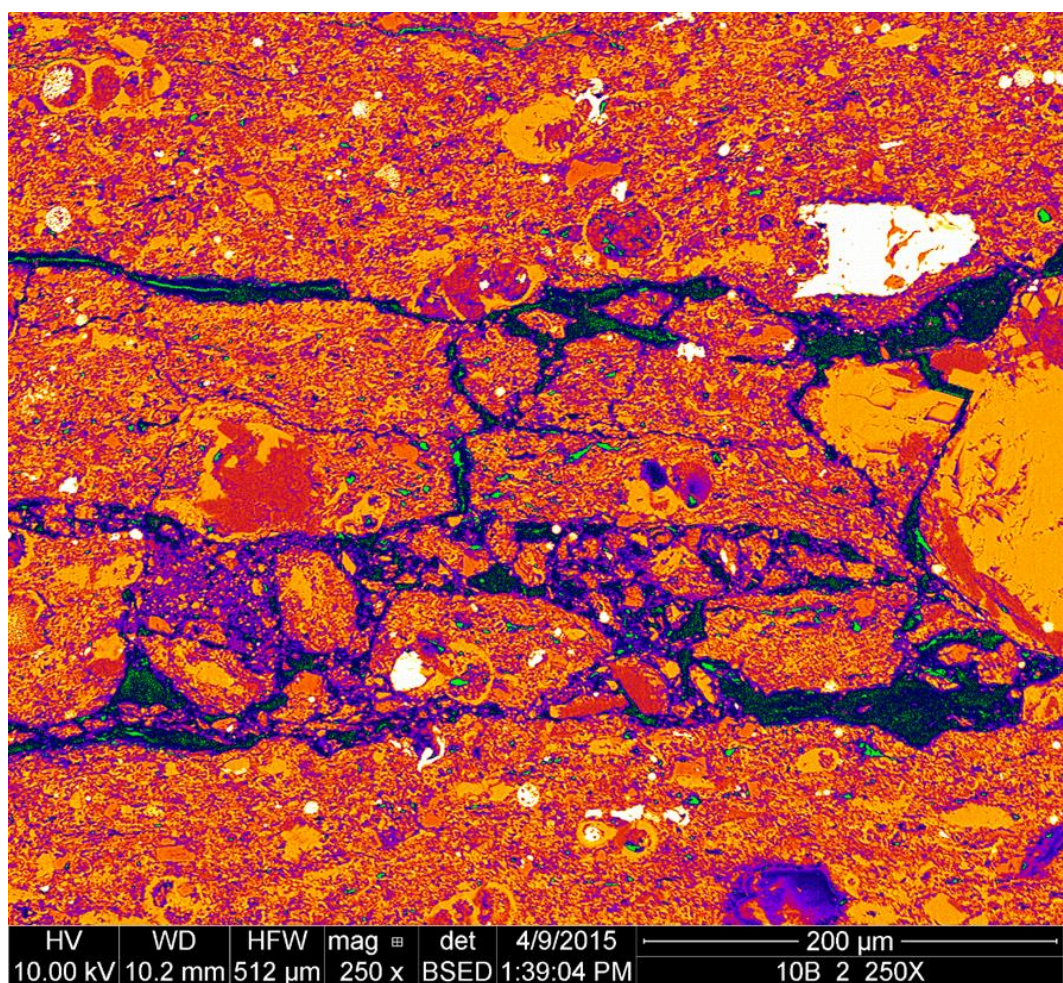


Figure 40. Modified fire lookup table. Lookup table (LUT) of modified Fire (from ImageJ Software) LUT shades applied to 8-bit images using assigned numbers 0 through 255. The bright green is associated with the lowest LUT #s, analogous to the lowest densities, and the brightest white represents 255



# INDEX






Starting LUT #	Lookup Table Colors	Ending LUT #	Phase
0		10	Pore Space and V. Lt. Organics (Oil and Gas)
11		70	Organic Matter (Crude Oil, Bitumen, and Kerogen)
71		150	Quartz and Lt. Clays
151		239	Calcite and Hvy. Clays
240		255	Apatite, Marcasite, and Pyrite

Figure 41. 8-bit backscattered electron images with modified fire lookup table. Images collected for sample 10B using a 10 kV beam and a working distance of 10 mm, displayed at 250X with a HFW of 512 μm false colored using the modified Fire LUT (Fig. 41). Representative colors from each phase range are displayed in the index.



### 5.3.3 Pore conservation: effective pressure

Observations of thin-walled foram shells that are only partially filled or entirely empty raise questions of fluids that have been lost between drilling and specimen observations, and potentially abnormal fluid pressures in shales during burial. The foraminifera shells are relatively thin (averaging 3.7  $\mu\text{m}$ ) and act as intragranular pore space (Fig. 42 and 43).

The preservation of forams is surprising, considering the depth of burial and effective pressures ( $P_e$ ) calculated from the difference between lithostatic and hydrostatic gradients. However, bottomhole fluid pressures indicate that fluids within the sampling interval were overpressured, reducing values of effective pressure (Fig. 44). Fine-grained rocks with high capillarity and low permeability can serve as seals to fluids, leading to excess pore fluid pressures. This is displayed by the  $P_{pf}$  points plotting between the lithostatic and hydrostatic pressure curves. With depth,  $P_{pf}$  approaches  $P_l$  and therefore  $P_e$  decreases, resulting in preservation of the pore structures (foram shells in this case). This can only hold true if the foraminifera experience a constant volume ( $\Delta V = 0$ ) of calcite, clay, or organic matter (bitumen, kerogen, oil, and/or gas) under pressure resulting from burial. This relationship holds true for all filled intragranular pore space.



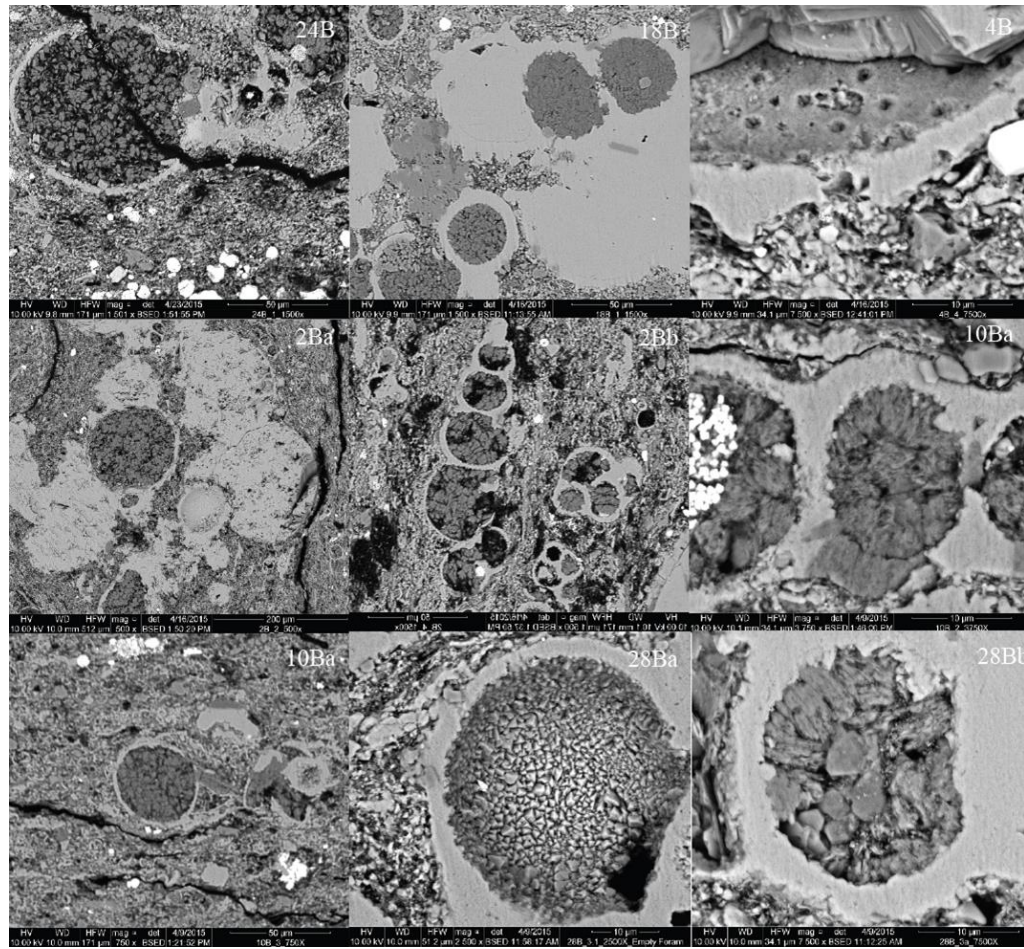
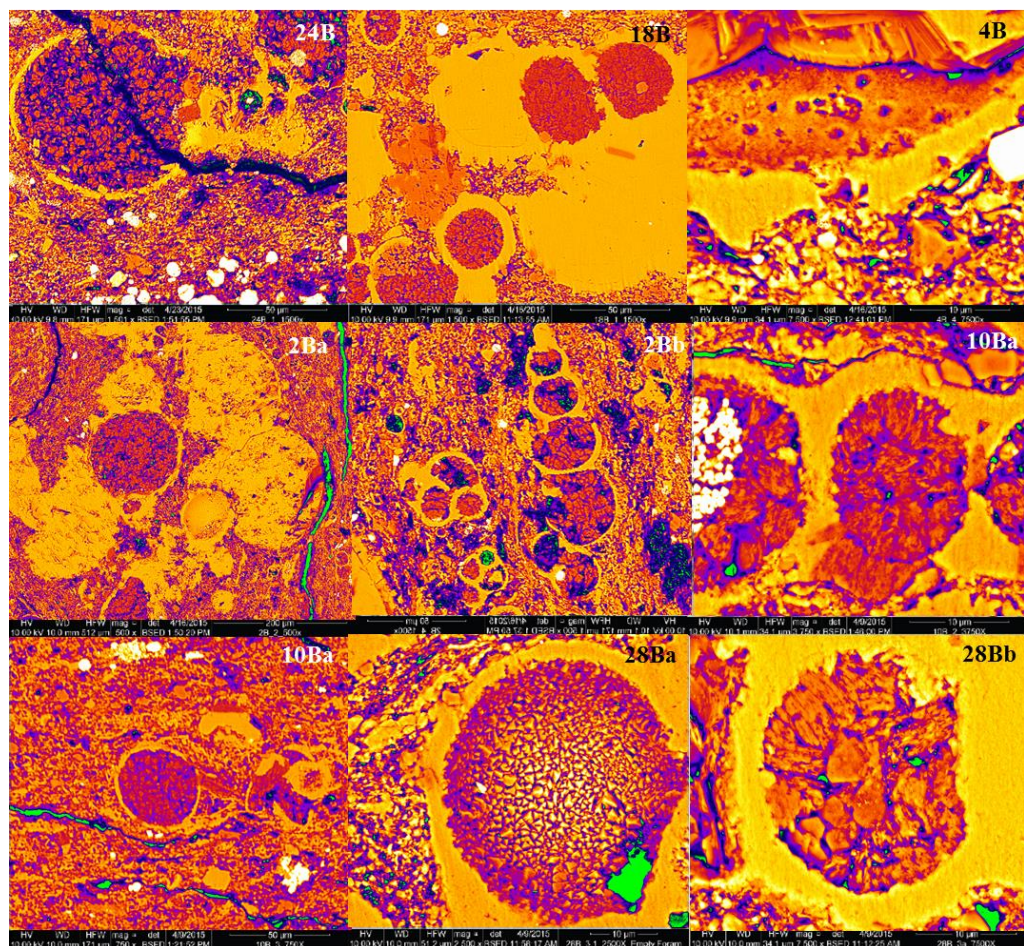


Figure 42. Backscattered electron images of foraminifera. BSE images representing the variability in foraminifera found within multiple samples. Images were analyzed for foram wall thickness (10 measurements taken for each image using ImageJ Software); resulting average foram wall thickness is  $3.689 \mu\text{m}$  with a standard deviation of  $1.813 \mu\text{m}$  and a wall-thickness range of  $1.000 - 10.227 \mu\text{m}$ .



#### INDEX






Starting LUT #	Lookup Table Colors	Ending LUT #	Phase
0		10	Pore Space and V. Lt. Organics (Oil and Gas)
11		70	Organic Matter (Crude Oil, Bitumen, and Kerogen)
71		150	Quartz and Lt. Clays
151		239	Calcite and Hvy. Clays
240		255	Apatite, Marcasite, and Pyrite

Figure 43. False-color backscattered electron images of foraminifera. These images demonstrate the variability in foraminifera found within multiple samples. Images were analyzed for foram wall thickness (10 measurements taken for each image using ImageJ Software); resulting average foram wall thickness is 3.689  $\mu\text{m}$  with a standard deviation of 1.813  $\mu\text{m}$  and a wall-thickness range of 1.000 – 10.227  $\mu\text{m}$ .



As seen in Figure 44, this relationship is complicated due to the polynomial character of  $P_{pf}$ . Zoback (2007) describes this pattern in detail, breaking down the transition zone (area between lithostatic and hydrostatic pressure) into two separate zones, with the deeper zone experiencing a much higher pressure gradient. In Zoback (2007), the higher pressure gradient begins around 3000 m. The boundary between the zones for these data is located closer to 2500 m. The presence of two distinct zones suggests that compaction is complicated by multiple factors. During early burial, compaction is dominated by effective pressure. As burial (and temperature/maturity) progresses, pore fluids in the form of hydrocarbons begin to form, which results in increased porosity and  $P_{pf}$ , and decreased effective pressures, leading to the preservation of open pores within the rocks.

Pore preservation is further complicated by the process of cementation. The timing of cementation plays a role in preservation of pore space. Figures 45(A) and 45(B) exhibit framboidal pyrites contained within preserved foram shells. This is suggestive of bacterially mediated sulfur reduction (Wacey et al., 2015) within the forams at temperatures below 60-80°C (Machel, 2001). Assuming a geothermal temperature gradient of 25°C/km during burial and surface temperature of 25°C during the Cenomanian age of the Cretaceous period (Slingerland et al., 1996), the framboidal pyrite was likely precipitated by a burial depth no greater than 1.5 km. Given the microstructural relationships observed in SEM between original foram shells, precipitated calcite, and framboidal pyrite (Fig. 45A,B), the shell wall thicknesses appear to have increased by calcite precipitation at inner shell surfaces (Fig. 45C) before the

framboidal pyrite was precipitated (before burial to 1.5 km). Thus, foram shells were strengthened early in the burial history and did not collapse, helping to preserve porosity within when effective pressures  $P_e$  of  $\sim 18$  MPa were reached at burial depths of  $\sim 2.4$  km. Other microstructural observations (Fig. 45D) indicate that effective pressures reached values close to the failure point of some foram shells, with microfractures displayed by some of the thinner shells. Maximum effective pressures experienced by shales buried to varying depths reached  $\sim 20$  MPa (Fig. 44). Little consideration is required to analyze any stress concentrations above this mean value that would have contributed to foram shell crushing and porosity reduction, owing to the fine grain size of the matrix surrounding foram shells. Analyses of stress concentrations leading to fracture indicate the importance of coordination and grain size of surrounding grains (Sammis, 1997; King and Sammis, 1992), and the coordination of shale-size matrix grains ( $\sim 2.5$   $\mu\text{m}$ ) surrounding a 50  $\mu\text{m}$ -sized foram is well over 100.

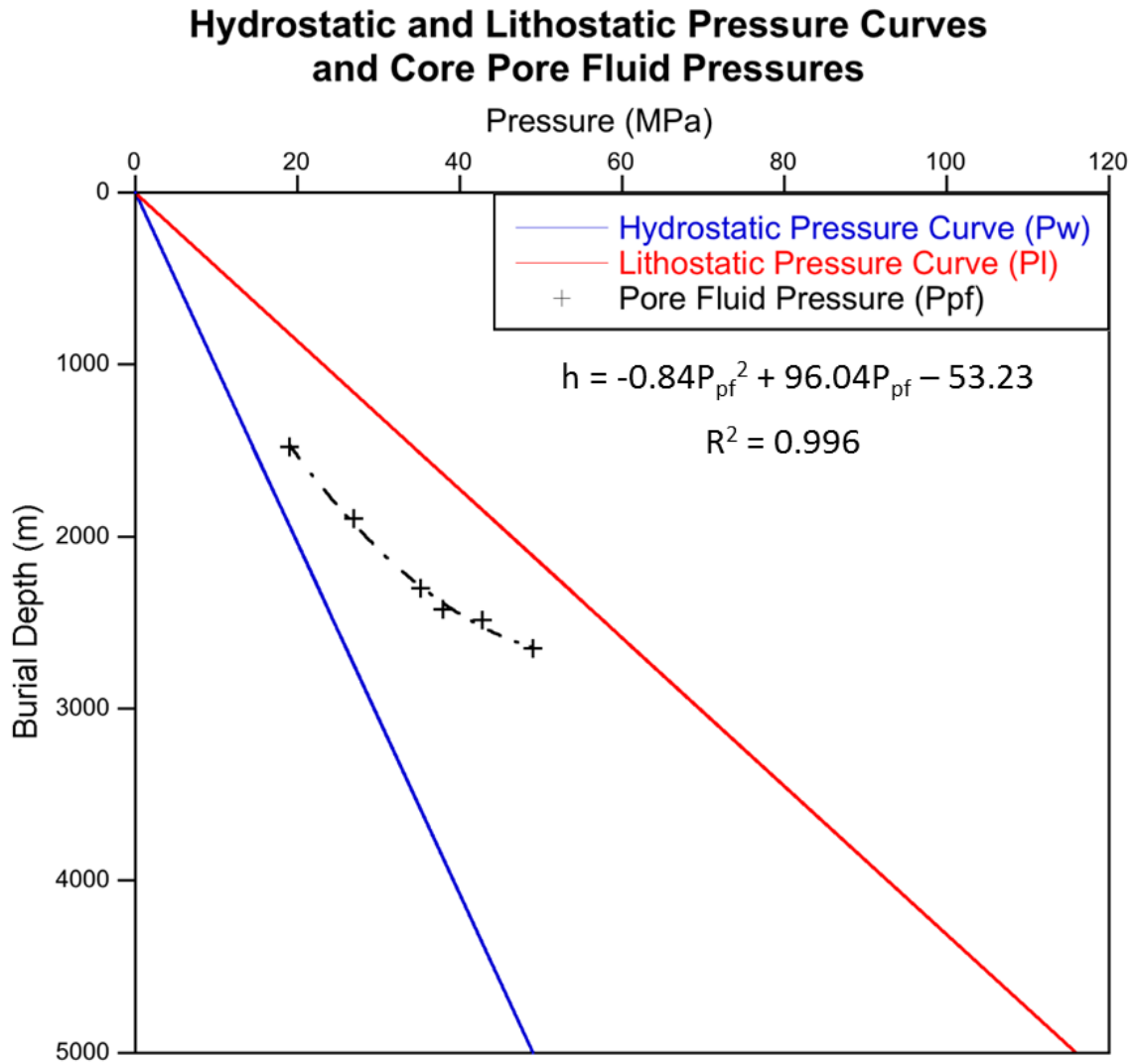


Figure 44. Hydrostatic and lithostatic pressure curves and core pore fluid pressures. Plot of pressure versus depth. The blue line represent the hydrostatic pressure with depth ( $P_w = \rho_w g h$ , where  $\rho_w = 1000 \text{ kg/m}^3$ ,  $g = 9.8 \text{ m/s}^2$ , and  $h$  is the depth of burial). The red line represents the lithostatic pressure with depth ( $P_l = \rho_l g h$ , where  $\rho_l = 2367 \text{ kg/m}^3$ ,  $g = 9.8 \text{ m/s}^2$ , and  $h$  is the depth of burial). Plotted points represent measured pore fluid pressure ( $P_{pf}$ ) and display a strong ( $R^2 = 0.996$ ) polynomial relationship ( $h = -0.84P_{pf}^2 + 96.04 P_{pf} - 53.23$ ). Effective pressure ( $P_e$ ) is calculated by Equation (1).

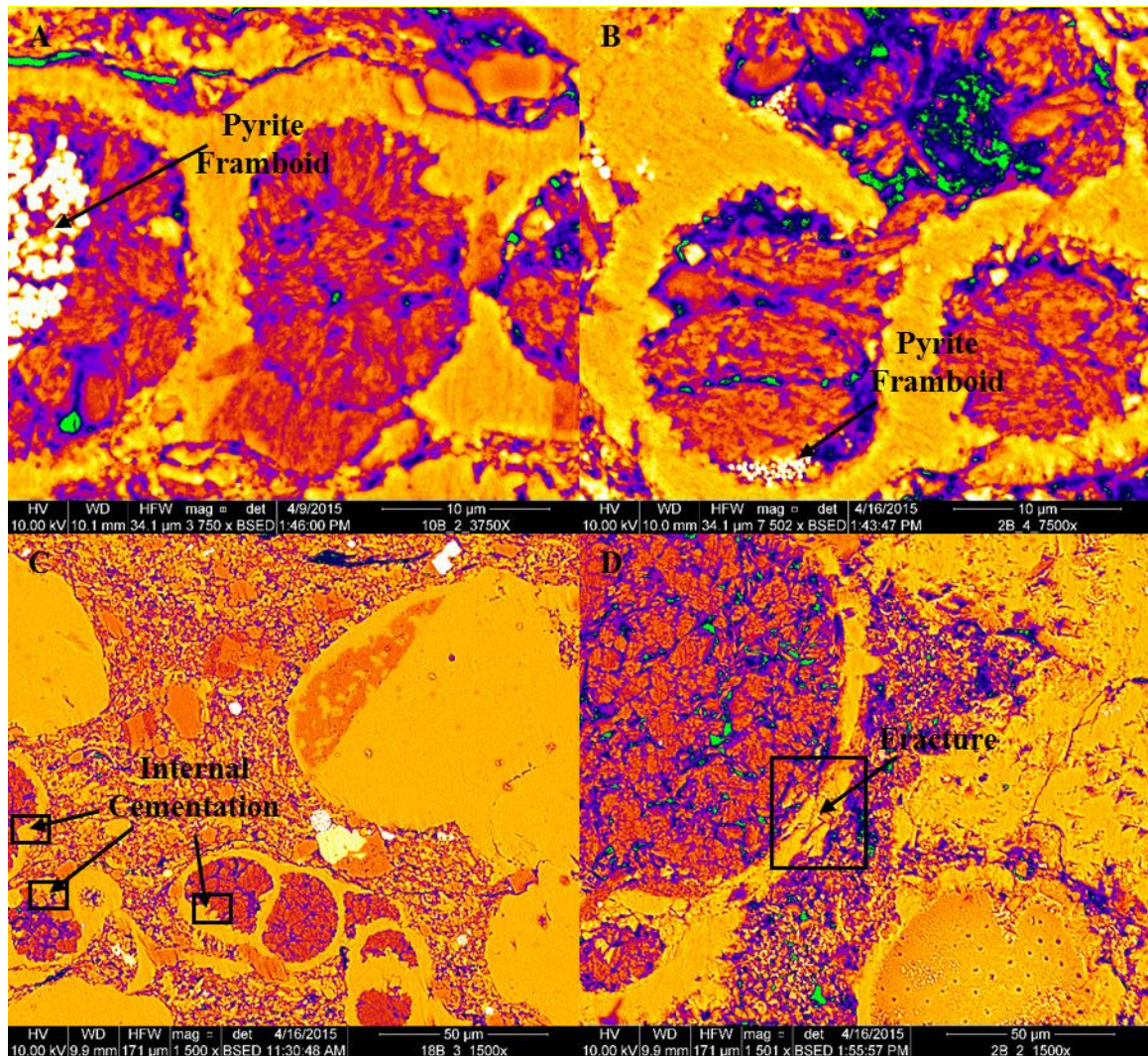


Figure 45. False-colored backscattered electron images of foraminifera. Displayed images represent diversity of foraminifera found within multiple samples. Images A and B contain pyrite framboids, suggestive of low-temperature emplacement of sulfur-rich compounds. Image C displays internal cementation of foram shells. Image D displays thin-walled foram fractures suggestive of pre-failure zone of effective pressure.

Organic pores are typically small, with the vast majority of pores having diameters  $< 5 \mu\text{m}$ . The largest pores ( $10 - 100 \mu\text{m}$ ) found in the BSE images reside within fractures and forams. During compaction of shales, the largest pore spaces are lost first, preserving the micropores (Delage and Lefebvre, 1983; Dewhurst and Aplin, 1998). Small pores require larger effective pressure to collapse because more lithostatic load is supported by surrounding solids (Dewhurst and Aplin, 1998). Small pores behave “stronger” since solids surrounding pore need to be deformed for pores to collapse with increasing areas of contact between neighboring solids as pores are reduced in size (Fig. 46). Based on BSE results, porosity within these unconventional reservoir shales appears to be primarily intragranular and organic.

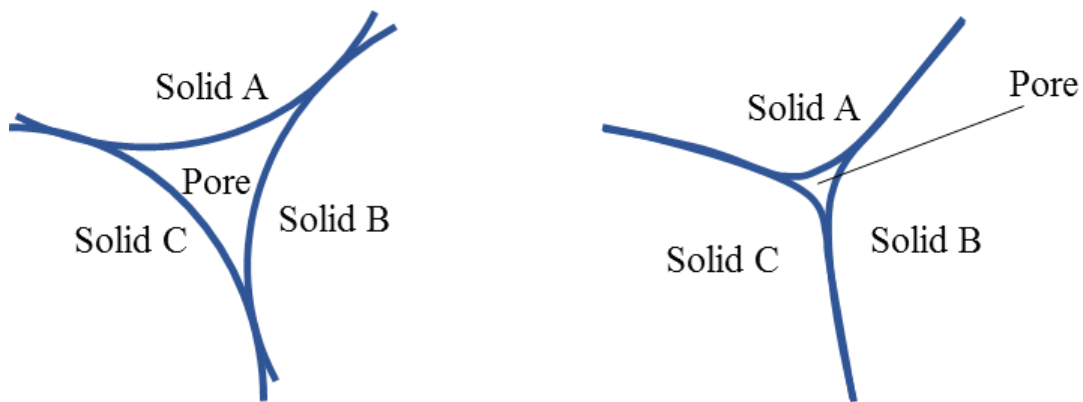


Figure 46. Pore diagrams. Large pore and small pore diagrams illustrating differences in the amount of solid-solid contact surrounding pore spaces.

#### *5.3.4 Backscattered electron porosity relationships*

Wopenka and Pasteris (1993) suggest that carbonates may catalyze organic maturity, and therefore porosity, for a given burial pressure and temperature. To test this, the BSE sampling locations were analyzed for percent area of calcite, as determined by BSE LUT # analyses, and grouped into 2 categories: average calcium (Avg Ca) and calcium-rich (Ca-Rich). These values were plotted against BSE porosity (% area), as calculated using LUT # ranges (Fig. 47); each plotted point represents the average calcite content (% area) for a thin section. A third category which averaged the combined calcite content of Avg Ca and Ca-Rich, called “All” was also created.

The samples selected from regions with average Ca, or the mixed calcite/clay/quartz layers, exhibit an overall lower porosity. As discussed earlier, these locations have lower densities of foraminifera, suggesting that significant pore space is created related to the forams, or specifically contained within the forams. The two calcite/clay/quartz BSE images exhibiting higher than expected porosity ( $> 1$  % area) contain organically filled fractures which demonstrate pore densities that are greater than the surrounding matrix material (Fig. 48). Whether the carbonates chemically catalyze porosity or simply provide a compaction-protected reservoir for organic matter is unclear.



### Backscatter Electron Porosity vs. Backscatter Electron Calcium Content

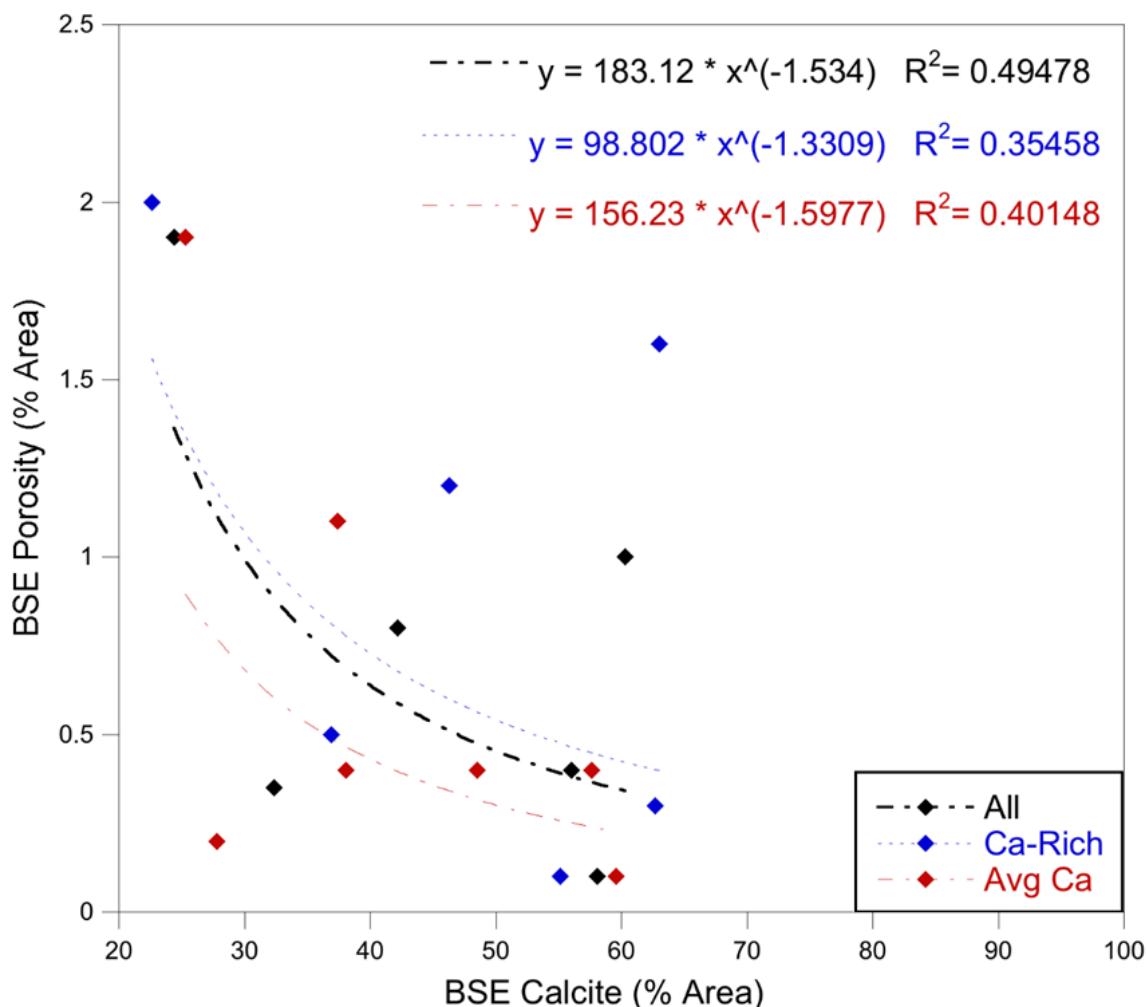


Figure 47. Backscattered electron porosity vs. backscattered electron calcite content. Chart displaying relationship between BSE porosity, as % area, against BSE calcite content, as % area, for average values collected in calcium-rich (blue), average calcium (red), and all (black) locations on analyzed polished plates. The Avg Ca samples displayed an overall lower BSE porosity compared with the Ca-Rich and combined (All) sampling locations. Curve fits for each (All, Ca-Rich, and Avg Ca) are displayed, with  $0.354 < R^2 < 0.495$ .

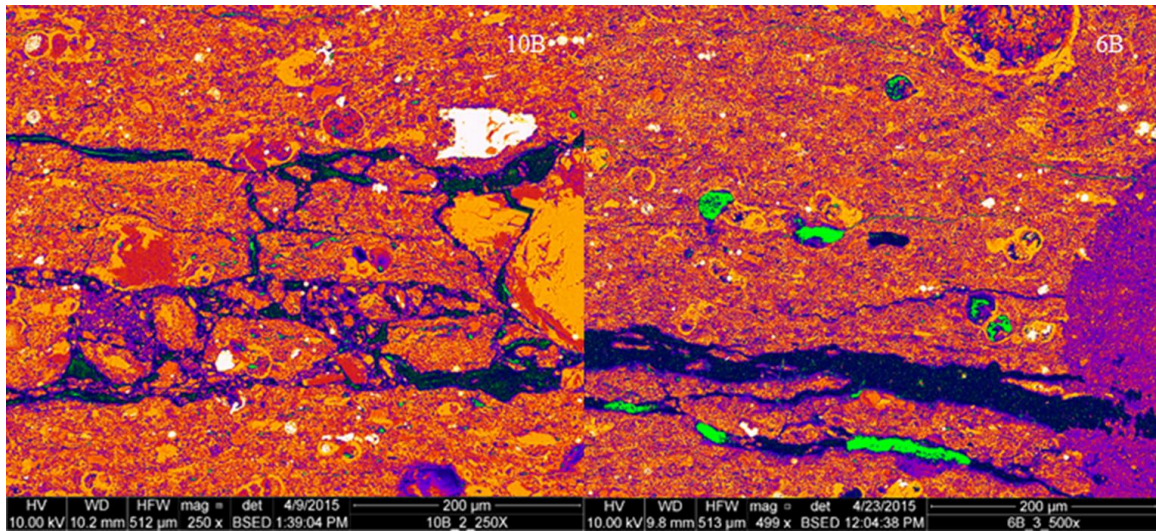


Figure 48. Backscattered electron images of average calcium: fractured regions. 8-bit BSE images collected for sample 10B and 6B using a 10 kV beam and a working distance of 10 mm with a HFW of 512-513  $\mu\text{m}$ , false colors assigned by the modified Fire LUT (Fig. 40). These images correspond to the two highest porosity BSE images for Avg Ca and with significant evidence of fracturing, filled afterwards by low-density organic matter and pores, suggesting increased organic porosity in the presence of filled-fractures.

The quantified BSE porosity is expected to increase with maturity, resulting from medium-density convertible carbon forms transforming to lower-medium density retained (adsorbed, absorbed, and stored) organic solids and expelled hydrocarbons. The expelled hydrocarbons may act as pore-filling fluids (oil and gas), while higher-density residual carbon phases consist of inert kerogen and pyrobitumen matrix material. This relationship is analyzed using measured maturity (%Ro) (Fig. 49).

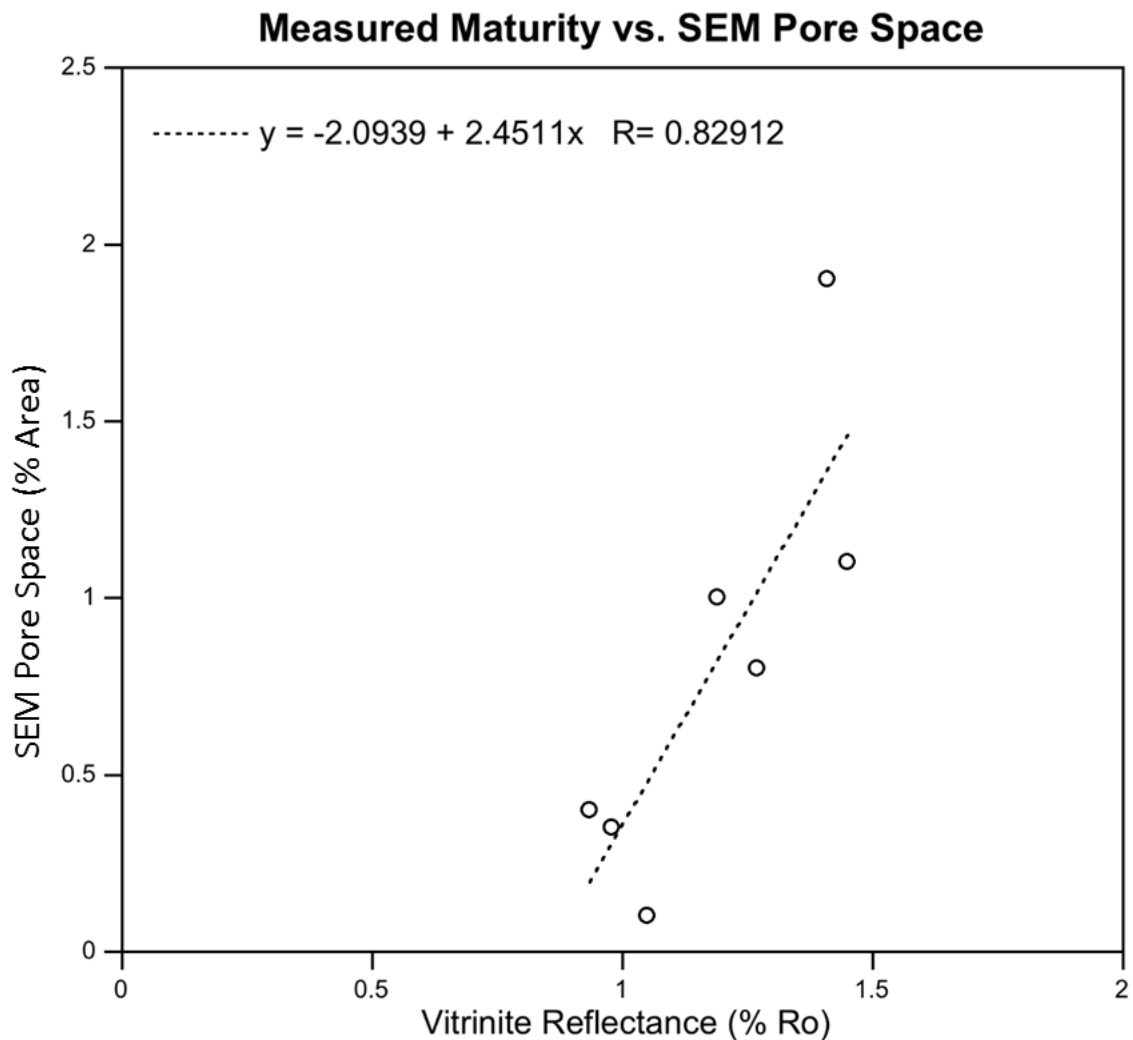


Figure 49. Measured maturity vs. SEM pore space. Chart exhibiting a positive linear relationship between measured maturity, as vitrinite reflectance (%Ro), against BSE porosity (% area) for samples collected at comparable core depths. The black dashed line represents the best fit relationship, which exhibits a relatively good ( $R^2 = 0.68745$ ) relationship between measured maturity and BSE image porosity that could be refined with additional sampling.

BSE porosity and measured maturity show a positive linear relationship with  $R^2 = 0.69$ , suggesting a correlation between increased pore space and increased maturity. This relationship suggests a process whereby organic pore space is created as the shale matures, though the apparent pore space (~ 0–2% area) is not equal to the Dean Stark estimated porosity (~ 6–15% volume). Thus, adsorption and absorption of lighter hydrocarbons within denser hydrocarbons may play a significant role in the storage of mobile hydrocarbons within unconventional reservoir shales. The effective storage area, and the quantity of immobile components that reside in bitumen porosity, remain difficult to quantify using BSE as a result of the inability to separate kerogen and bitumen by density (Table 5).

The positive linear relationship between BSE porosity and measured maturity, which correlates to depth (Fig. 50), differs markedly from established compaction curves associated with the response of porous rocks to increasing effective pressure (Kominz and Pekar, 2001; Rhodehamel, 1977; Smith et al., 1976). Plotting total porosity versus burial depth and comparing these data with a modified shale compaction curve, accounting for effects of cementation, based on the work of Kominz and Pekar (2001):

$$\varphi = 0.30e^{-\frac{h}{1593}} \quad (13)$$

where  $\varphi$  is porosity and  $h$  is burial depth, yields results suggesting a more complicated relationship between porosity and depth (Fig. 51). The results of this study suggest that porosity does not decrease strictly with depth in organically-rich shales. Instead, porosities may reduce due to compaction at shallow intervals and then begins to increase with thermal maturity of hydrocarbons at greater depths (Fig. 52). The degree

to which thermal maturation increases porosity relative to losses of porosity depend on the total organic carbon content of the rock as well as the temperature gradient with depth relative to the pressure gradient. More work must be done to establish the true nature of the organically-rich shale compaction curve to understand the character of compaction once over-maturity is reached and to understand the interplay between compaction and maturation.

#### *5.4 Upscaling*

Predictions based on interpretations and relationships demonstrated in this study can be applied to measurements from core samples and to larger scale log results for effective porosity. Improved estimates of economic viability and sweet spot mapping are two possible byproducts of porosity and mobility determinations. However, in order to properly upscale these results sufficient reservoir material must be sampled in order to take into account fracturing and calcite density at larger scales. Moreover, reliable measured maturity analysis will be necessary. True mobility is not only dependent on the pore fluid components, but also the permeability of the reservoir lithology. Without a sufficiently connected network of pore space for the fluids to flow through and adequate capillarity, the mobile pore fluids will be unable to migrate and become truly mobile.

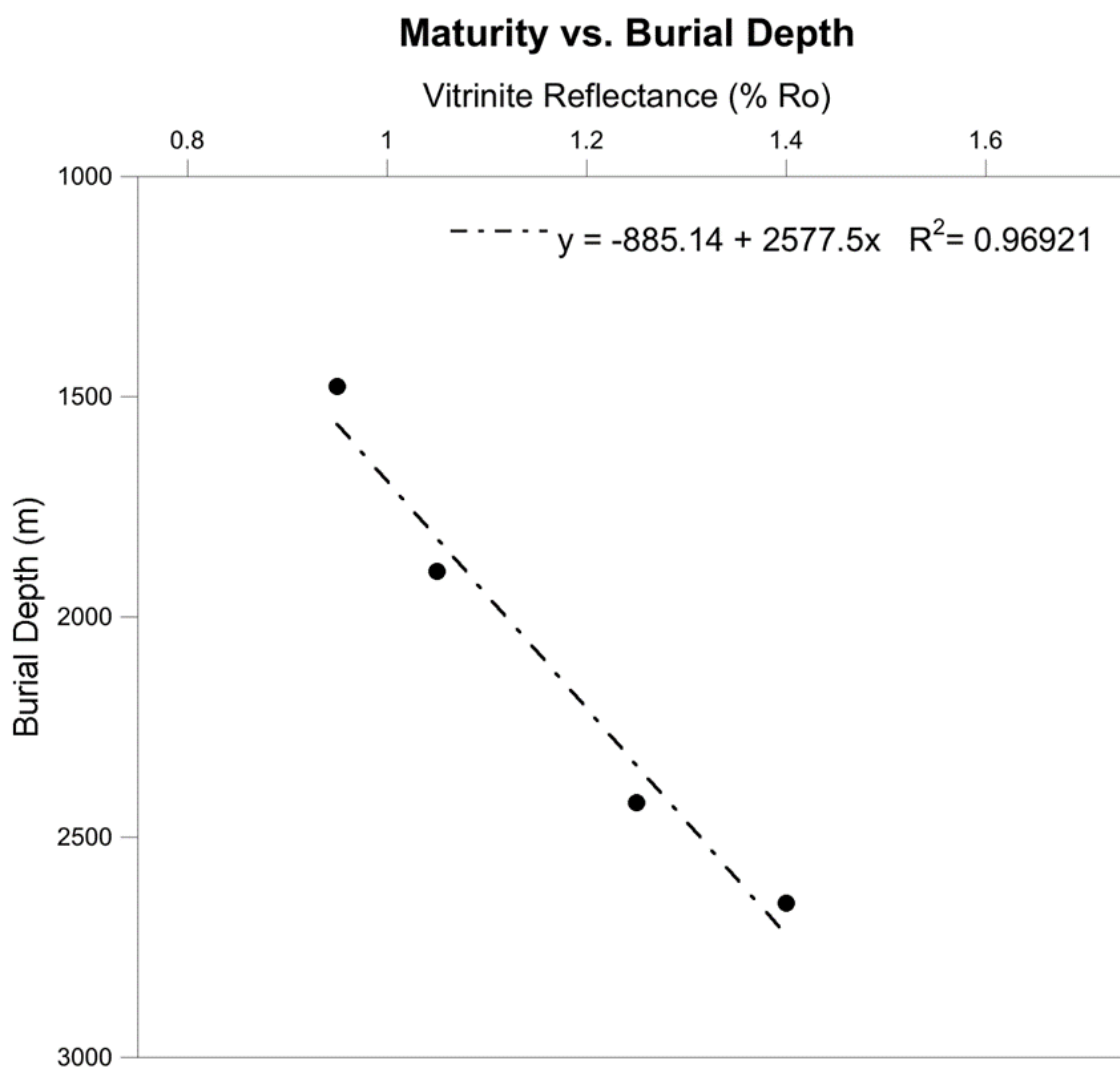


Figure 50. Measured maturity vs. burial depth. Chart exhibiting a linear relationship between average measured maturity for each core, as vitrinite reflectance (%Ro), against burial depth (m). The black dashed line represents the best fit relationship, which exhibits a strong ( $R^2 = 0.97$ ) relationship between measured maturity and burial depth.

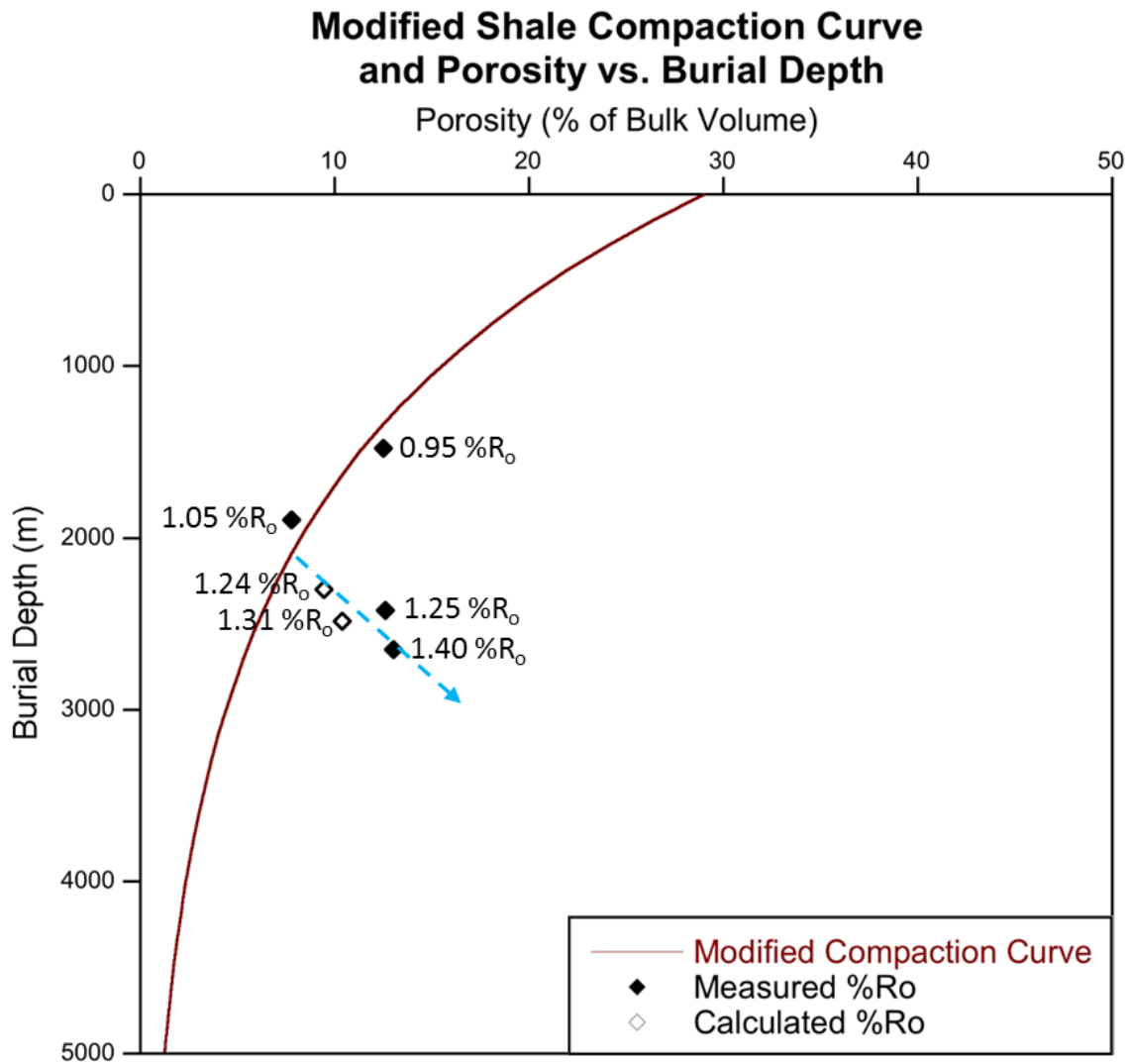


Figure 51. Modified shale compaction curve and porosity vs. burial depth. Modified shale compaction curve based on the deepest portion of low-porosity shale compaction curve from Kominz and Pekar (2001) and modified to include the effects of cementation (Equation 13) plotted as porosity (% of bulk volume) versus burial depth (m) represented as a maroon curve. Plotted points represent average total porosity for each of the 6 cores (C1 through C6) plotted at the average sample depth. The dashed blue arrow represent the suggested trend of increased porosity with depth resulting from maturation of hydrocarbons. Each plotted point has been labelled with its corresponding maturity (%Ro). Points plotted as solid black diamond are labelled with measured maturities, and points plotted as outlined diamonds are labelled with estimated maturities based on the relationship between maturity and burial depth determined in Figure 49.

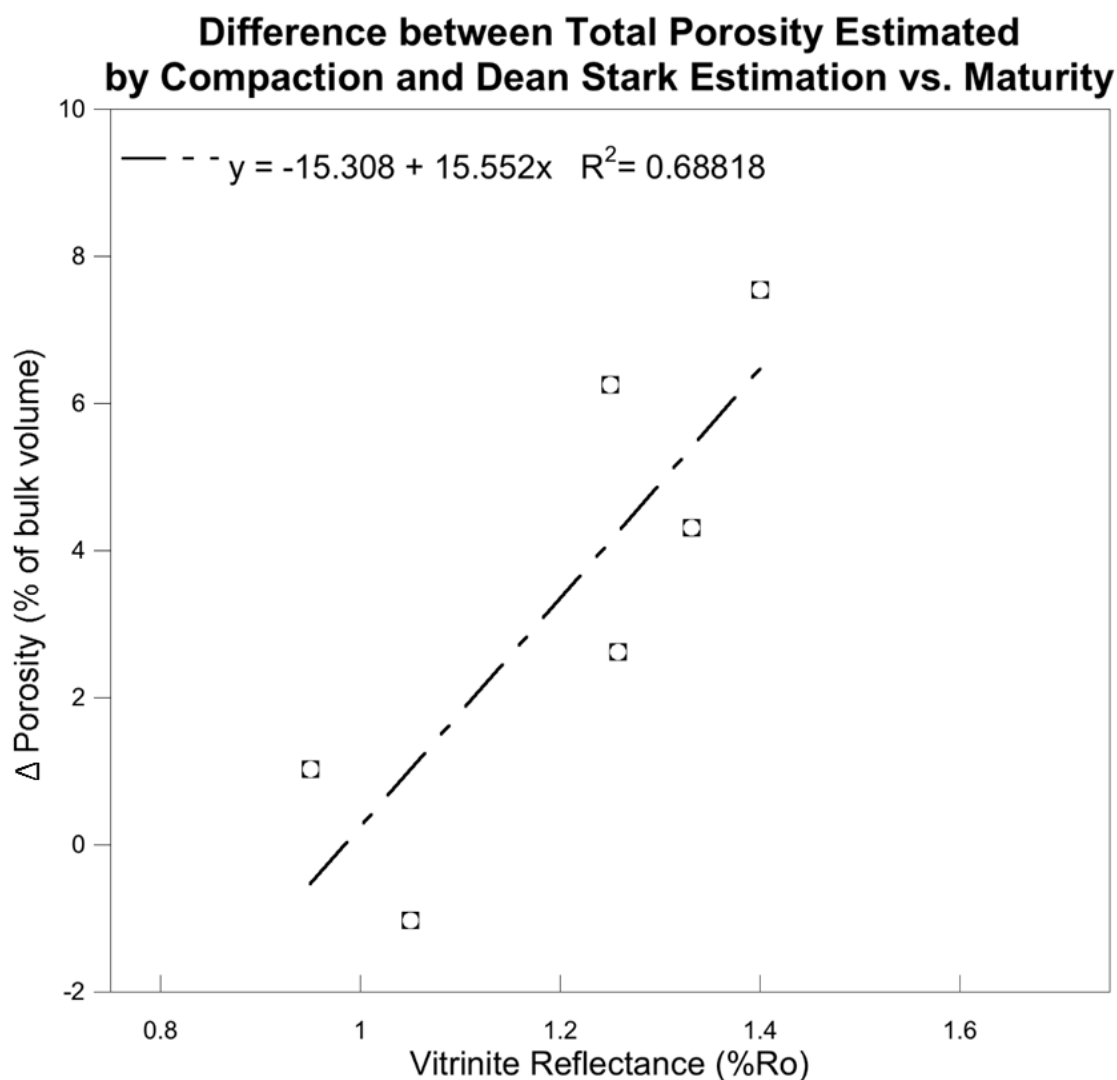


Figure 52. Difference between total porosity estimated by compaction and Dean Stark estimation vs. maturity. Chart exhibiting a linear relationship between average differences in total porosity estimated by modified compaction curve (Equation 13) and total porosity estimated by Dean Stark and average measured maturity for each core, as  $\Delta$ Porosity (% bulk volume) against vitrinite reflectance (%Ro). The black dashed line represents the best fit relationship, which exhibits a linear relationship between measured porosity difference and maturity ( $R^2 = 0.69$ ).



## 6. CONCLUSIONS

Combining results of extraction, pyrolysis, LECO TOC, XRD, MicroXRF, reflected light microscopy, WDS, and BSE, pore space and pore-filling fluids lead to the following conclusions about the nature of organic shale porosity and its relationship with maturity:

- GRI/Dean Stark solvent extraction measurements combined with Pyrolysis measurements provide sufficient data to effectively quantify matrix-contributing kerogen, immobile bitumen, and mobile pore-filling fluids.
- Mobility of pore-filling hydrocarbons has a relatively strong ( $R^2 = 0.93$ ) positive linear relationship with measured vitrinite reflectance, implying that measured maturity (%Ro) can be used as a predictor of hydrocarbon mobility, and therefore, effective porosity.
- Porosity is highest in calcite-rich layers with forams. Forams serve as intragranular pores, and are not broken during compaction to depths of 2650 m. Organically rich foram-filling material appears to be isolated and uncommunicative with surrounding pores or shale matrix. Porosity also appears to increase in the presence of organically filled fractures.
- Primary porosity of organically rich matrix material is significant but permeability is relatively low.
- LUT # analyses of BSE images provides a means of quantifying shale composition and porosity at fine scales of observation (microns).

- BSE imaged pore space exhibits a positive linear relationship ( $R^2 = 0.69$ ) with measured vitrinite reflectance, but BSE imaged pore space is not equal to solvent extraction measurements of porosity. Adsorption and Absorption, therefore, play a large role in pore-fluid storage within unconventional shales. Moreover, the increase in porosity with maturation overwhelms the reduction in porosity anticipated during compaction due to lithostatic loads.
- In contrast to the geochemical techniques of identifying organic matter in shales, microscopic techniques of geochemical identification remain deficient. Instead, identification and study of organic phases at the microscope rely on morphology and density of organics.
- Upscaling of microscopic results for porosity and composition is difficult due to variations in fracture densities and foram densities.

## REFERENCES

- Al-mashramah, Yaser Abdullah Abdullah, “Maturity of Kerogen, Petroleum Generation and the Application of Fossils and Organic Matter for Paleotemperature Measurements.” Masters diss., Lund University, 2011.
- Avseth, Per, Tapan, Mukerji, and Gary Mavko. 2005. “Introduction to Rock Physics.” In *Quantitative Seismic Interpretation: Applying Rock Physics Tools to Reduce Interpretation Risk*, 1-47. New York: Cambridge University Press.
- Baskin, David K. 1997. “Atomic H/C Ratio of Kerogen as an Estimate of Thermal Maturity and Organic Matter Conversion.” *AAPG Bulletin* 81: 1437–1450.
- Bernard, Sylvain, Richard Wirth, Anja Schreiber, Hans-Martin Schulz, and Brian Horsfield. 2012. “Formation of Nanoporous Pyrobitumen Residues during Maturation of the Barnett Shale (Fort Worth Basin).” *International Journal of Coal Geology* 103: 3-11.
- Brace, William F. 1980. “Permeability of Crystalline and Argillaceous Rocks.” *International Journal of Rock Mechanics and Mining Sciences & Geomechanics Abstracts* 17: 241-251.
- Burger, Jon, Doug McCarty, Russ Peacher, and Timothy Fischer, “Sample Preparation for Unconventional Analysis: a Case against Solvent Extraction.” Paper presented at the *International Symposium of the Society of Core Analysts*, Avignon, France, 8-11 September 2014.
- Camp, Wayne K. and Barry E. Wawak. 2013. “Enhancing SEM Grayscale Images through Pseudocolor Conversion: Examples from Eagle Ford, Haynesville, and Marcellus Shales.” In *Electron Microscopy of Shale Hydrocarbon Reservoirs: Memoir 102*, edited by Wayne K. Camp, Elizabeth Diaz, and Barry Wawak, 15-26. Tulsa: The American Association of Petroleum Geologists.
- Charest, Marc. 2013. “Petroleum Geochemistry: the Source is the Reservoir.” *Canadian Discovery Digest* 5: 17–48.
- Clementz, David M. 1979. “Effect of Oil and Bitumen Saturation on Source-Rock Pyrolysis: Geologic Notes.” *AAPG Bulletin* 63(12): 2227-2232.

- Collins, Dylan and Scott Lapierre, “Integrating Solvent Extraction with Standard Pyrolysis to Better Quantify Thermal Maturity and Hydrocarbon Content in the Oil Window.” *Unconventional Resources Technology Conference*, Denver, Colorado, 25 – 27 August, 2014. Convention Presentation.
- Crain, E. Ross. 2014. “Petrophysical Handbook – Total Organic Carbon (TOC).” Crain’s Petrophysical Handbook. Accessed July 2014. <https://www.spec2000.net/11-vshtoc.htm>.
- Curtis, Mark E., Brian J. Cardott, Carl H. Sondergeld, and Chandra S. Rai. 2012. “Development of Organic Porosity in the Woodford Shale with Increasing Thermal Maturity.” *International Journal of Coal Geology* 103: 26-31.
- Dean, E. W. and D. D. Stark. 1920. “A Conventional Method for the Determination of Water in Petroleum and Other Organic Emulsions.” *The Journal of Industrial and Engineering Chemistry* 12(5): 486-490.
- Delage, Pierre and Guy Lefebvre. 1984. “Study of the Structure of a Sensitive Champlain Clay and of its Evolution during Consolidation.” *Canadian Geotechnical Journal* 21: 21-35.
- Dembicki, Harry, Jr. “Shale Gas Geochemistry Mythbusting.” Paper presented at the *AAPG Annual Convention and Exhibition*, Pittsburgh, Pennsylvania, 19-22 May 2013.
- Dembicki, Harry, Jr. 2009. “Three Common Source Rock Evaluation Errors Made by Geologists during Prospect or Play Appraisals.” *American Association of Petroleum Geologists Bulletin* 93(3): 341-356.
- Dewhurst, David N. and Andrew C. Aplin. 1998. “Compaction-Driven Evolution of Porosity and Permeability in Natural Mudstones: an Experimental Study.” *Journal of Geophysical Research* 103(B1): 651-661.
- Dow, Wallace G. 1977. “Kerogen Studies and Geological Interpretations.” *Journal of Geochemical Exploration* 7: 79-99.
- Espitalie, J., J. L. Laporte, M. Madec, F. Marquis, P. LePlat, J. Paulet, and A. Boutefeu. 1977. “Methode Rapide de Caracterisation des Roches Meres de Leur Potentiel Petrolier et de Leur Degre d’Evolution.” *Revue l’Institute Franc,ais du Pe’trole*, 32: 23–42.
- Espitalie, J., F. Marquis, and I. Barsony. 1984. “Geochemical Logging.” *Analytical Pyrolysis – Techniques and Applications*: 276-304.

- Espitalie, J., G. Deroo, and F. Marquis. 1985. "La Pyrolyse Rock-Eval et ses Applications." *Revue de l'Institut Français du Pétrole* 40: 563-579 and 755-784.
- Fjaer, Erling, Rune M. Holt, Per Horsrud, Arne M. Raaen, and Rasmus Risnes. 2008. "Failure Mechanics." In *Petroleum Related Rock Mechanics*, 55-102. New York: Elsevier.
- Handwerger, D. A., D. Willberg, M. Pagels, B. Rowland, and J. F. Kerrer, "Reconciling Retort versus Dean Stark Measurements on Tight Shales." Paper presented at the *Society of Petroleum Engineers Annual Technical Conference and Exhibition*, San Antonio, Texas, 8-10 October 2012.
- Janssens, Koen H. A., Freddy C. V. Adams, and Anders Rindby. 2000. "Overview." In *Microscopic X-ray Fluorescence Analysis*, 1-16, New York: John Wiley & Sons, Inc.
- Jarvie, Daniel M., Ronald J. Hill, Tim E. Ruble, and Richard M. Pollastro. 2007. "Unconventional Shale-Gas Systems: the Mississippian Barnett Shale of North-Central Texas as One Model for Thermogenic Shale-Gas Assessment." *AAPG Bulletin* 91(4): 475-499.
- Jarvie, Daniel M.. 2012. "Components and Processes Affecting Producibility and Commerciality of Shale Oil Resource Systems." Paper presented at *Houston Geological Society Applied Geoscience Conference*, Houston, Texas, 20-21 February 2012.
- Jennings, Debra S. and Jonathan Antia. 2013. "Petrographic Characterization of the Eagle Ford Shale, South Texas: Mineralogy, Common Constituents, and Distribution of Nanometer-Scale Pore Types." In *Electron Microscopy of Shale Hydrocarbon Reservoirs: Memoir 102*, edited by Wayne K. Camp, Elizabeth Diaz, and Barry Wawak, 101-114. Tulsa: The American Association of Petroleum Geologists.
- Kane, Jeff. 2007. "A Petrophysical Comparison of the Barnett and Woodford Shales." Paper presented at *Permian Basin Geological Synthesis Project Annual Meeting*, Austin, Texas, 26-27 February 2007.
- King, Geoffrey C. P. and Charles G. Sammis. 1993. "The Mechanisms of Finite Brittle Strain." In *Fractals and Chaos in the Earth Sciences*, edited by Charles G. Sammis, M. Saito, and Geoffrey C. P. King, 611-640. Boston: Birkhäuser Verlag Basel.

- Klug, Harold P. and Leroy E. Alexander. 1954. "Fundamental Principles of X-ray Diffraction." In *X-ray Diffraction Procedures for Polycrystalline and Amorphous Materials*, 111-161, New York: John Wiley & Sons, Inc.
- Kominz, Michelle A. and Stephen F. Pekar. 2001. "Oligocene Eustasy from Two-Dimensional Sequence Stratigraphic Backstripping." *Geological Society of America Bulletin* 113(3): 291-304.
- Kwon, Ohmyoung, Andreas K. Kronenberg, Anthony F. Gangi, and Brann Johnson. 2001. "Permeability of Wilcox Shale and its Effective Pressure." *Journal of Geophysical Research* 106(B9): 19339-19353.
- Lemmens, Herman, and Dennis Richards. 2013. "Multiscale Imaging of Shale Samples in the Scanning Electron Microscope." In *Electron Microscopy of Shale Hydrocarbon Reservoirs: Memoir 102*, edited by Wayne K. Camp, Elizabeth Diaz, and Barry Wawak, 27-36. Tulsa: The American Association of Petroleum Geologists.
- Loucks, Robert G., Robert M. Reed, Stephen C. Ruppel, and Ursula Hammes. 2012. "Spectrum of Pore Types and Networks in Mudrocks and a Descriptive Classification for Matrix-Related Mudrock Pores." *AAPG Bulletin* 96(6): 1071-1098.
- Luffel, D. L., F. K. Guidry, and J. B. Curtis. 1992. "Evaluation of Devonian Shale with New Core and Log Analysis Methods." *Journal of Petroleum Technology* 44(11): 1192-1197.
- Machel, Hans G. 2001. "Bacterial and Thermochemical Sulfate Reduction in Diagenetic Settings – Old and New Insights." *Sedimentary Geology* 140(1):143-175.
- Modica, Christopher J. and Scott G. Lapierre. 2012. "Estimation of Kerogen Porosity in Source Rocks as a Function of Thermal Transformation: Example from the Mowry Shale in the Powder River Basin of Wyoming." *AAPG Bulletin* 96(1): 87-108.
- Morrow, C. A., L. Q. Shi, and J. D. Byerlee. 1984. "Permeability of Fault Gouge under Confining Pressure and Shear Stress." *Journal of Geophysical Research* 89(B5): 3193-3200.
- Neglia, S. 1979. "Migration of Fluids in Sedimentary Basins." *AAPG Bulletin* 63:573-597.

- Ocean Drilling Program. 2014. "Rock Eval Pyrolysis." Texas A&M University. Accessed July 2014. [http://www.odp.tamu.edu/publications/tnotes/tn30/tn30\\_11.htm](http://www.odp.tamu.edu/publications/tnotes/tn30/tn30_11.htm).
- Passey, Q. R., K. M. Bohacs, W. L. Esch, R. Klimentidis, and S. Sinha. 2010. "From Oil-Prone Source Rock to Gas-Producing Shale Reservoir – Geologic and Petrophysical Characterization of Unconventional Shale-Gas Reservoirs." Presented at *CPS/SPE International Oil & Gas Conference and Exhibition in China*, Beijing, China, 8-10 June, 2010.
- Pepper, Andrew S. 1991. "Estimating the Petroleum Expulsion Behavior of Source Rocks: A Novel Quantitative Approach." Geological Society, London, Special Publications 59(1): 9-31.
- Peters, Kenneth E. 1986. "Guidelines for Evaluating Petroleum Source Rock Using Programmed Pyrolysis." *AAPG Bulletin*, 70: 318–329.
- Rasband, W.S. 1997-2014. ImageJ, U. S. National Institute of Health, Bethesda, Maryland, USA, <http://imagej.nih.gov/ij>.
- Reed, Stephen Jarvis Brent. 2005. "Scanning Electron Microprobe Analysis and Scanning Electron Microscopy in Geology." New York: Cambridge University Press.
- ResTech. 1996. "Development of Laboratory and Petrophysical Techniques for Evaluating Shale Reservoirs." Chicago: Gas Research Institute Report GRI-95/0496.
- Rhodehamel, E. C. 1977. "Sandstone Porosities." In *Geological Studies on the COST No. B-2 Well, U.S. Mid-Atlantic Outer Continental Shelf Area: Geological Survey Circular 750*, edited by P.A. Scholle, 23-31.
- Rice, Dudley D. 1993. "Composition and Origins of Coalbed Gas: Chapter 7." In *Hydrocarbons from Coal: AAPG Special Volumes 38(1993)*: 159 – 184.
- Roberts, Willard L., Thomas. J. Campbell, and George R. Rapp, Jr. 1990. *Encyclopedia of Minerals*. New York: Van Nostrand Reinhold.
- Sammis, Charles G. 1997. "Fractal Fragmentation and Frictional Stability in Granular Materials." In *IUTAM Symposium on Mechanics of Granular and Porous Materials*, edited by N. A. Fleck and A. C. F. Cocks, 23 - 34. Cambridge: Springer-Science+Business Media, B.V.

- Scholle, Peter A. and Dana S. Ulmer-Scholle. 2003. "A Color Guide to the Petrography of Carbonate Rocks: Grains, Textures, Porosity, Diagenesis" *AAPG Memoir* 77.
- Senftle, J. T., and Charles R. Landis. 1991. "Vitrinite Reflectance as a Tool to Assess Thermal Maturity: Chapter 12: Geochemical Methods and Exploration." In *Source and Migration Processes and Evaluation Techniques: AAPG Treatise of Petroleum Geology, Handbook of Petroleum Geology*. edited by R. K. Merrill, 119–125.
- Slatt, Roger M. and Neal R. O'Brien. "Pore Types in the Barnett and Woodford Gas Shales: Contribution to Understanding Gas Storage and Migration Pathways in Fine-Grained Rocks." *AAPG Bulletin* 96(12): 2017–2030.
- Slingerland, Rudy, Lee R. Kump, Michael A. Arthur, Peter J. Fawcett, Bradley B. Sageman, and Eric J. Barron. 1996. "Estuarine Circulation in the Turonian Western Interior Seaway of North America." *Geological Society of America Bulletin* 108(8): 941-952.
- Smith, John W. "Theoretical Relationship between Density and Oil Yield for Oil Shales." United States Department of the Interior, Bureau of Mines Report of Investigation, No. 7248, 17 April 1969.
- Smith, K. Lee, L. Douglas Smoot, Thomas H. Fletcher, and Ronald J. Pugmire. 1994. "Coal Structural Characterization by Advanced Techniques." In *The Structure and Reaction Processes of Coal*, edited by Dan Luss, The Plenum Chemical Engineering Series, 77-196. New York: Plenum Press.
- Smith, M. A., R. V. Amato, M. A. Furbush, D. M. Pert, M. E. Nelson, J. S. Hendrix, L. C. Tamm, G. Wood, Jr., D. R. and Shaw. 1976. "Core Analysis, Shale Analysis, and Wireline Data." In *Geological and Operational Summary, COST no. B-2 Well, Baltimore Canyon Trough Area, Mid-Atlantic OCS: U.S. Geological Survey Open-File Report* 76–774, 13-26.
- Spain, David R. and Ryan McLin. 2013. "SEM Charecterization of Shale Gas Reservoirs Using Combined Secondary and Backscattered Electron Methods: an Example from the Haynesville Shale, Texas and Louisiana." In *Electron Microscopy of Shale Hydrocarbon Reservoirs: Memoir 102*, edited by Wayne K. Camp, Elizabeth Diaz, and Barry Wawak, 45-52. Tulsa: The American Association of Petroleum Geologists.
- Terzaghi, K., 1923, Die berechnung der durchlassigkeitsziffer des tones aus dem verlauf der hydrodynamithen spannungserscheinungen, Sitzungsber. Akad. Wiss. Wien Math Naturwiss. Kl. Abt. IIa, 132: 105–124.



- Tissot, B., B. Durand, J. Espitalie, and A. Combaz. 1974. "Influence of the Nature of Diagenesis or Organic Matter in the Formation of Petroleum." *AAPG Bulletin* 58(3): 499 – 506. Total Organic Carbon Analysis. 2012. Stratochem Services. Accessed 04 May 2015. [http://stratochem.com/?page\\_id=34](http://stratochem.com/?page_id=34).
- Total Organic Carbon (TOC-LECO) Analysis. 2015. Ellington and Associates, Inc. Accessed 04 May 2015. <http://www.ellingtongeologic.com/total-organic-carbon-TOC-LECO.html>.
- U. S. Geological Survey. 2011. "Photomicrograph Atlas." U. S. Geological Survey Energy Resources Program. Accessed 12 March 2015. <http://energy.usgs.gov/Coal/OrganicPetrology/PhotomicrographAtlas.aspx>.
- Wacey, David, Matt R. Kilburn, Martin Saunders, John B. Cliff, Charlie Kong, Alexander G. Liu, Jack J. Matthews, and Martin D. Brasier. 2015. "Uncovering Framboidal Pyrite Biogenicity using Nano-Scale CNorg Mapping." *Geology* 43(1): 27-30.
- Wang, Fred P., and Rob M. Reed, and A. John. 2009. "Pore Networks and Fluid Flow in Gas Shales." Presented at *SPE Annual Technical Conference*, New Orleans, Louisiana, 4-7 October 2009.
- Wentworth, Chester K. 1922. "A Scale of Grade and Class Terms for Clastic Sediments." *The Journal of Geology* 30(5): 377–392.
- Will, Georg. 2006. "The Reitveld Method." In *Powder Diffraction: the Reitveld Method and the Two-Stage Method*, 41-72. Germany: Springer.
- Wopenka, Brigitte and Jill Dill Pasteris. 1993. "Structural Characterization of Kerogens to Granulite-Facies Graphite: Applicability of Raman Microprobe Spectroscopy." *American Mineralogist* 78: 533–557.
- Young, Allen, Philip F. Low, and A. S. McLatchie. 1964. "Permeability Studies of Argillaceous Rocks." *Journal of Geophysical Research* 69(20): 4237-4245.
- Zdanavičiūtė, Onytė and Jurga Lazauskienė. 2009. "Organic Matter of Early Silurian Succession – the Potential Source of Unconventional Gas in the Baltic Basin (Lithuania)." *Baltica* 22(2): 89–98.
- Zoback, Mark D. 2007. "Pore Pressure at Depth in Sedimentary Basins." In *Reservoir Geomechanics*, 27-55. New York: Cambridge University Press.

## APPENDIX A

Total Porosity:

$$\varphi_t = 100 \times \frac{\rho_{grain} - \rho_{bulk}}{\rho_{grain} - \rho_{fluid}}$$

Water Porosity:

$$\varphi_w = 100 \times S_w \frac{\rho_{grain} - \rho_{bulk}}{\rho_{grain} - \rho_{fluid}}$$

Hydrocarbon Porosity:

$$\varphi_{hc} = 100 \times (S_{oil} + S_{gas}) \frac{\rho_{grain} - \rho_{bulk}}{\rho_{grain} - \rho_{fluid}}$$

Where:

$\varphi_t$  is total porosity (% of bulk volume)

$\varphi_w$  is water porosity (% of bulk volume)

$\varphi_{hc}$  is hydrocarbon porosity (% of bulk volume)

$\rho_{grain}$  is dry grain, or matrix, density (g/cm<sup>3</sup>)

$\rho_{bulk}$  is bulk density (g/cm<sup>3</sup>)

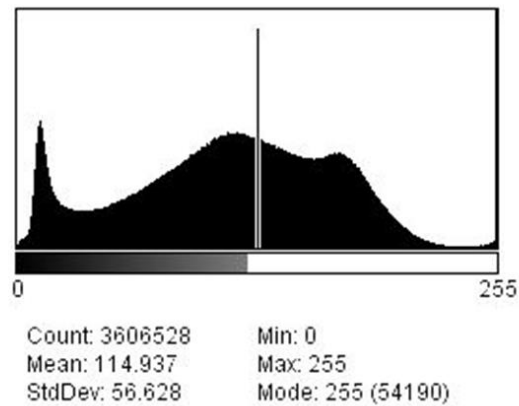
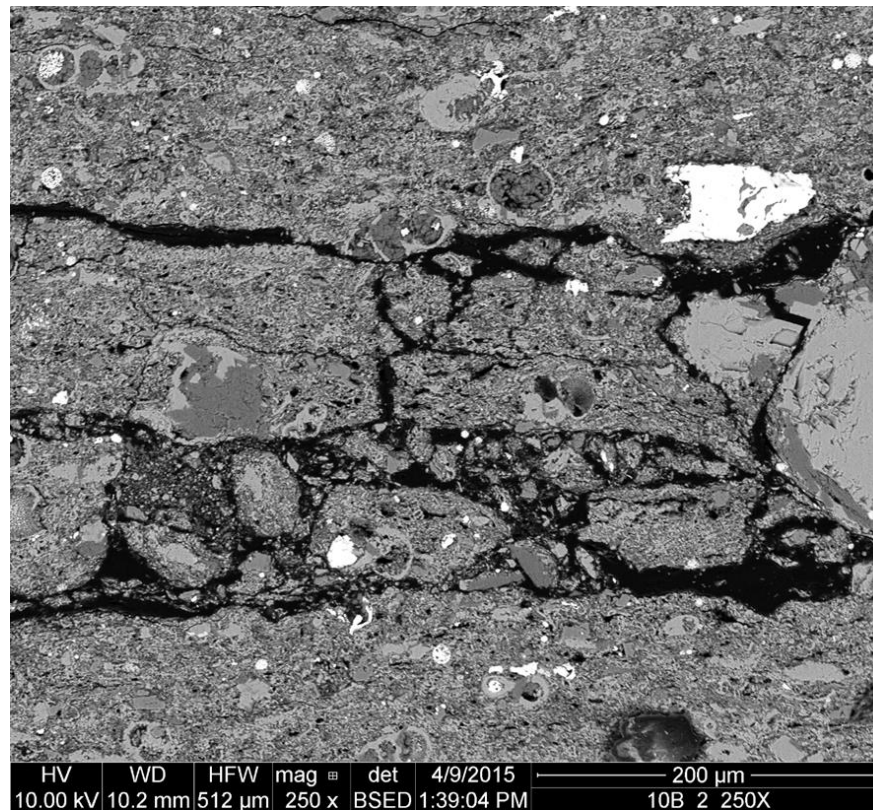
$\rho_{fluid}$  is fluid density (g/cm<sup>3</sup>)

$S_w$  is the water saturation (% of pore volume)

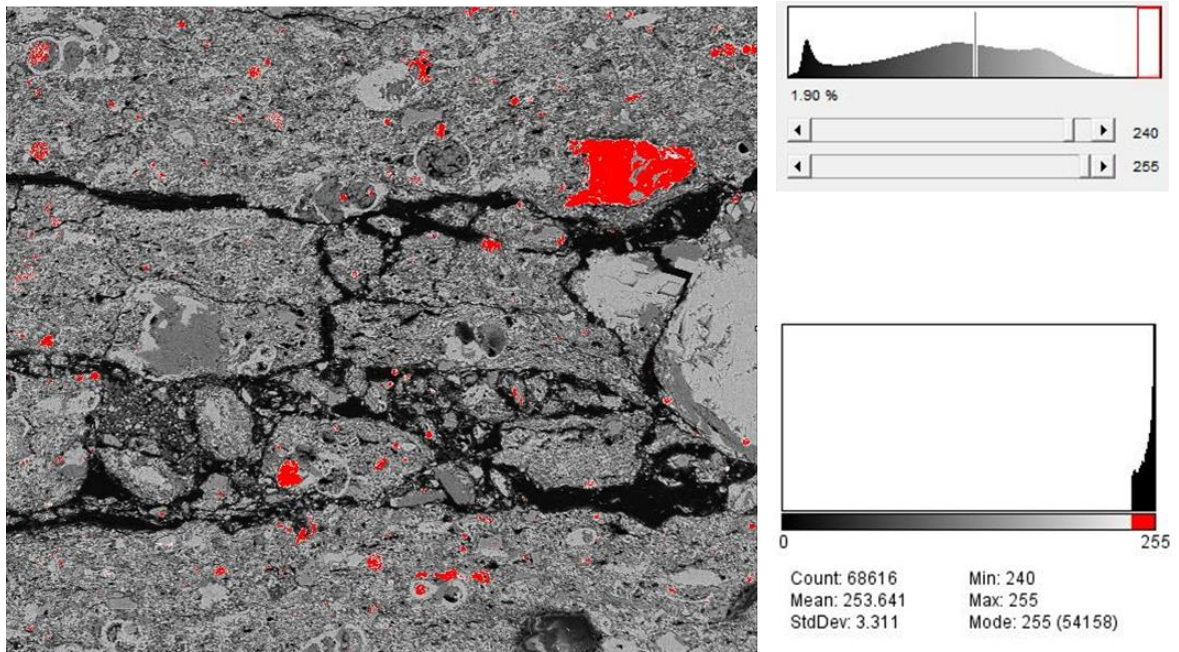
$S_{oil}$  is the oil saturation (% of pore volume)

$S_{gas}$  is the gas saturation (% of pore volume)

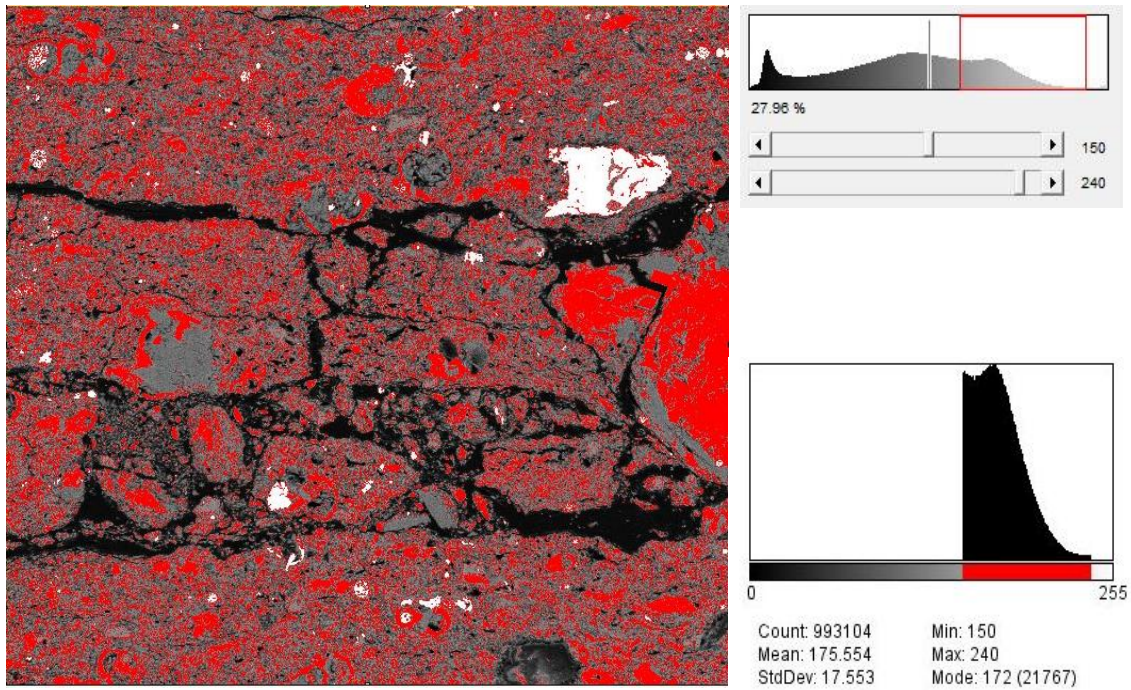
## APPENDIX B



Appendix B serves to illustrate the process for testing and confirming LUT # cutoffs for each phase of shale composition. This original 250X BSE image of sample 10B with a beam strength 10.00 kV and a working distance of 10.2 mm has been selected because of its representation of both fracturing and foraminifera content. Under the BSE image is a histogram displaying the pixel counts for LUT # 0 to 255. 0 represents black and 255 represents white.

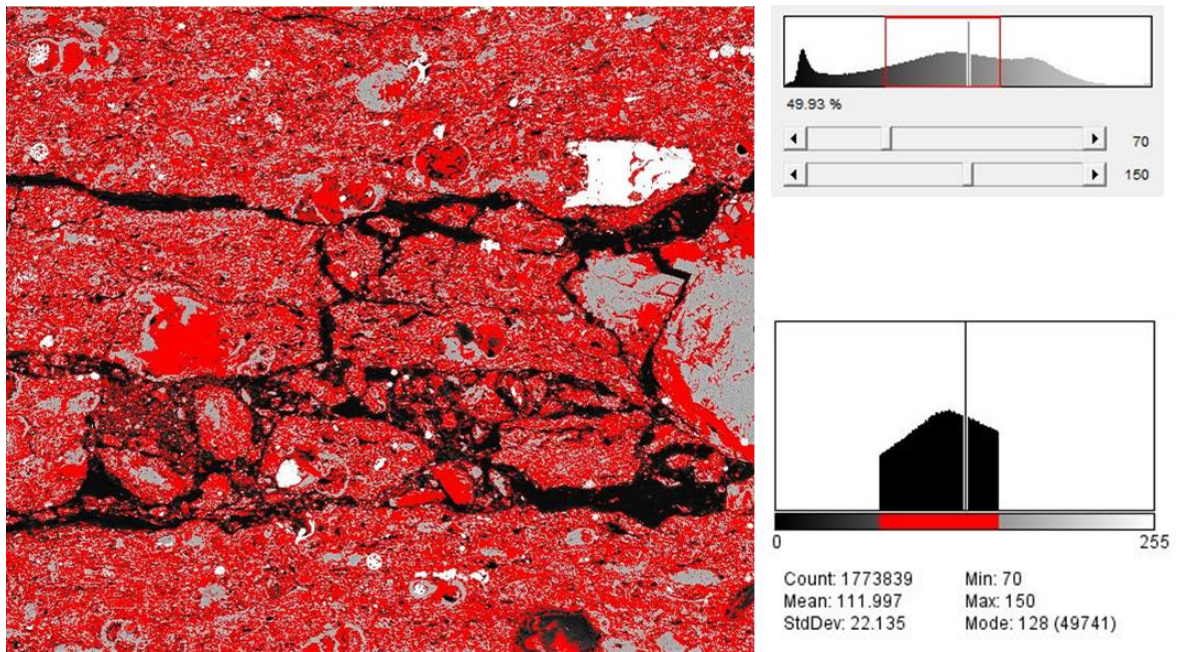


The red regions represent LUT # 240-255, corresponding to the highest-density ( $3.15 - 5.0 \text{ g/cm}^3$ ) materials contained within this shale sample: apatite, marcasite, and/or pyrite.

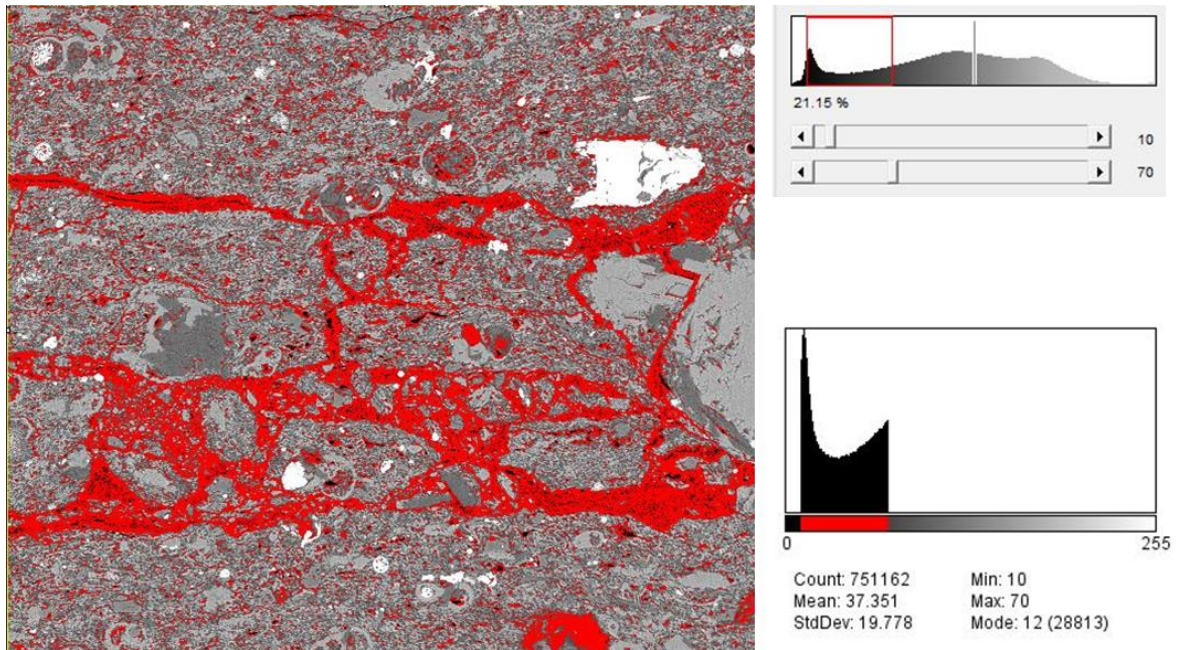


The red regions represent LUT # 150-240 corresponding to the second highest range of material densities ( $2.7 - 3.0 \text{ g/cm}^3$ ) contained within this shale sample: calcite and heavy clays.

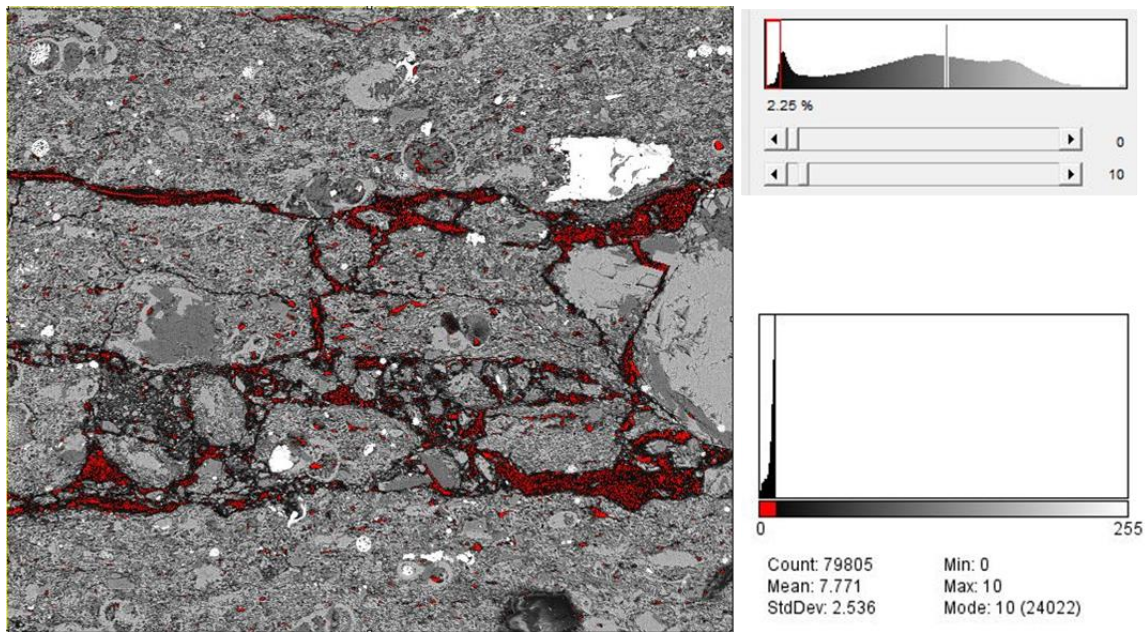




The red regions represent LUT # 70 – 150 corresponding to the middle range of material densities ( $2.2 - 2.65 \text{ g/cm}^3$ ) contained within this shale sample: quartz and light clays.



The red regions represent LUT # 10-70 corresponding to the second lowest range of material densities ( $0.8 - 2.2 \text{ g/cm}^3$ ) contained within this shale sample: organic matter (crude oil, bitumen, and kerogen).



The red regions represent LUT # 0-10 corresponding to the lowest range of material densities ( $0.0 - 0.6 \text{ g/cm}^3$ ) contained within this shale sample: pore space and very light organics (gas and oil).